UNIVERSITA' DEGLI STUDI DI PARMA

Dottorato di Ricerca in Scienza e Tecnologia dei Materiali Innovativi
XXIII Ciclo

Muons and Hydrogen in Graphene

Marcello Mazzani

Thesis submitted for the award of the degree of Ph.D. in Science and Technology of Innovative Materials

Tutor:
Chiar.mo Prof. Mauro Riccò

Coordinatore:
Chiar.ma Prof. Anna Painelli

CARBON

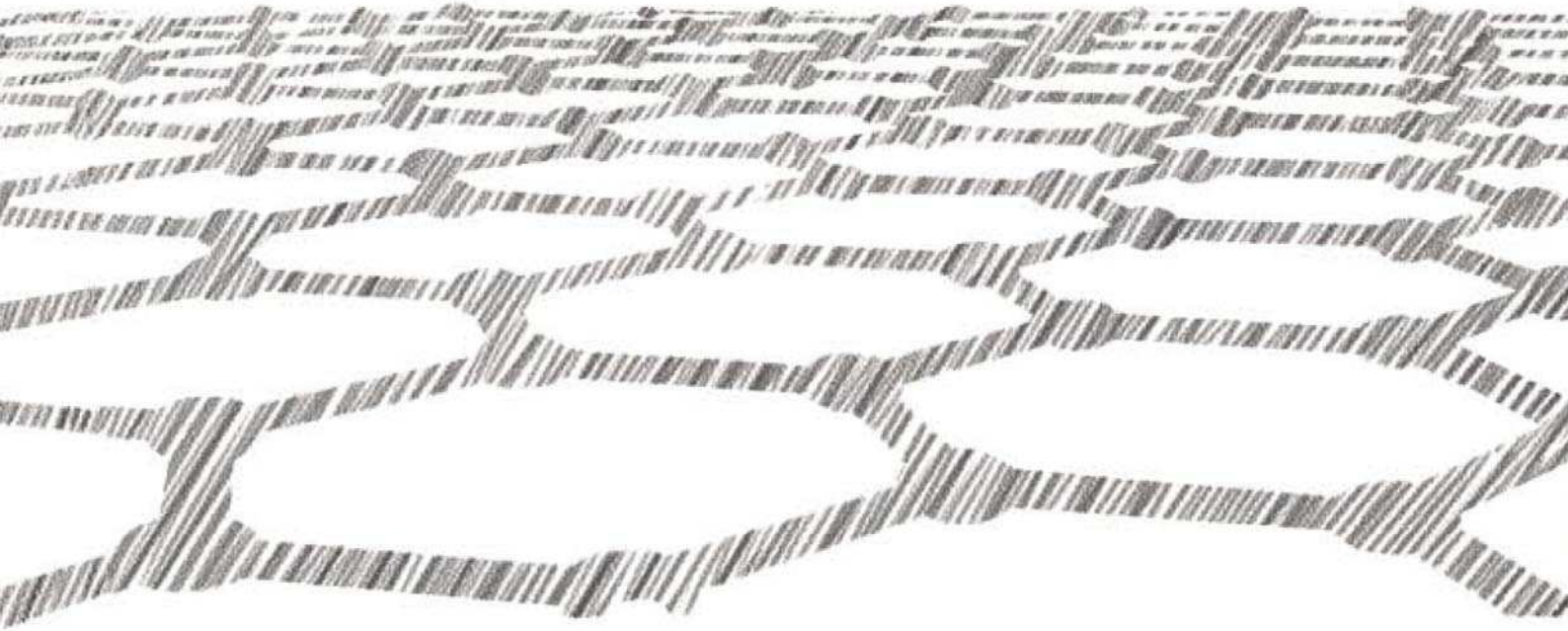

WONDERLAND

Abstract

Macroscopic quantities of graphenes have been prepared by different chemical methods and characterized by μSR spectroscopy, which proved a useful tool to study the interactions of the hydrogen atom with the defective graphene plane. A clear muon spin precession is observed in all the samples, contrary to the standard behaviour of graphite. Its origin lies in the magnetic dipolar interactions of hydrogen nuclei present at defects and reveal the formation of an extremely stable $CHMu$ (CH_2) state. The signal amplitude suggests that vacancies saturated by hydrogen have an extraordinary hydrogen capture cross-section.

In addition the μSR results, together with our SQUID investigations, pose important limits on the debated possibility of magnetism in graphene: μSR, indeed, is very sensitive to the local internal field and does not show the presence of any magnetization.

Contents

List of Tables

Introduction

The 2010 Nobel Prize award to the first successful research activities on graphene has shown the importance of this material even to the general public. Its amazing physical properties promise future technological applications in various fields. From electronics [1] to lightweight material engineering [2], from sensors [3, 4, 5] to energy storage [6, 7], graphene will probably be one of the leading materials in the technologies of the 21^{st} century.
Even if these applications are still far to come, these first years of research on graphene have been really fascinating: this system has shown a wealth of interesting phenomena related to fundamental physics. As it will be detailed in chapter 1, most of them arise from the low dimensionality of this material, which is properly bidimensional, and from its electronic energy spectrum, characterized by linear dispersion relations. Charge carriers in graphene behave as massless Dirac fermions and thus provide a valuable benchmark for relativistic quantum physics. They display extremely high mobility, even above 200000 $cm^2 \,/\, V\, s$, ballistic conduction and interesting magneto-transport properties, including the anomalous quantum Hall effect, observed already at room temperature.

Despite the great enthusiasm of the scientific community about the physics of graphene, documented by the over 7500 papers appeared in five years [8], this research field is very young and many topics are still unexplored. This is the case of graphene magnetic properties: many theoretical investigations suggest the onset of magnetic order in the bidimensional carbon lattice, triggered by defects [9, 10], but a full characterization of the material is not yet available. Similarly, the experimental studies of graphene interactions with other chemical species, important for future applications, are just at the beginning: for the case of hydrogen, for example, recent theoretical [6] and experimental [11] works have suggested that bulk graphene could represent a promising material for reversible hydrogen absorption, thanks to its huge specific surface area.
Recently, however, the development of chemical methods for the production of bulk quantities of graphene, achieved only at the end of 2008, has opened new possibil-

ities: the availability of gram-scale samples, indeed, allows to investigate the low-dimensional, nanoscopic graphene with spectroscopic techniques usually reserved to bulk solid state materials (the techniques used are shortly reviewed in chapter 2, while chapter 3 discuss the optimization of samples synthesis and their characterization).
Stimulated by these new opportunities, **the present thesis work is focused on the μSR characterization of chemically synthesized graphene**. The capabilities of this experimental technique are particularly suitable to explore different topics of interest: on the one hand μSR is extremely sensitive to magnetic interactions and, complemented by magnetometry investigations, can offer relevant insights into graphene magnetic properties and their connections with defects (chapter 4). On the other hand, muons in matter can act as light hydrogen isotopes and help to study the interactions of hydrogen atoms with graphene (chapter 5).

Chapter 1

Graphene

Graphene is a wonder material with many superlatives to its name. It is the thinnest known material in the universe and the strongest ever measured. Its charge carriers exhibit giant intrinsic mobility, have zero effective mass, and can travel for micrometers without scattering at room temperature. Graphene can sustain current densities six orders of magnitude higher than that of copper, shows record thermal conductivity and stiffness, is impermeable to gases, and reconciles such conflicting qualities as brittleness and ductility. Electron transport in graphene is described by a Dirac-like equation, which allows the investigation of relativistic quantum phenomena in a benchtop experiment.
(A.K.Geim, Graphene: Status and Prospects, Science 2009 [12])

Graphene is a single layer of carbon atoms, arranged in an planar honeycomb lattice (fig.1). It's the simplest carbon allotrope and may be regarded as the "mother" of others carbon structures: this two-dimensional system, in fact, can be stacked to form 3DIM graphite, rolled into 1DIM nanotubes and even wrapped into 0DIM fullerenes, as displayed in fig.2.
As a building block for all these systems, graphene has been the most theoretically studied, since 1947, when Wallace [13] calculated its band structure in the tight-binding approximation (see section 1.3). Nevertheless, it has been the latest carbon form to be experimen-

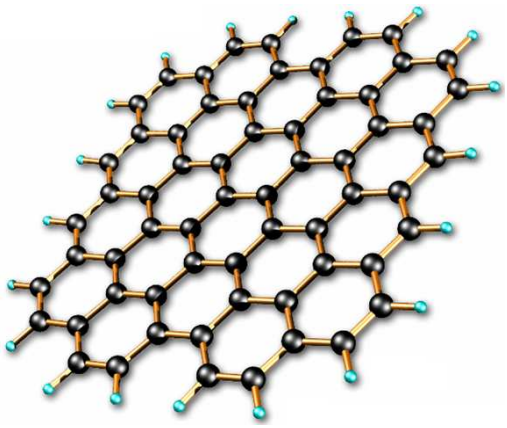

Figure 1. Graphene structure as an ideal 2DIM hexagonal lattice.

tally discovered: graphene sheets could not be isolated and recognized until 2004 [14]. The remarkable discovery and first characterization of monolayer graphene was accomplished at the University of Manchester by the Russian researchers Andre K. Geim and Kostantin Novoselov, who were awarded the Nobel Prize for physics in 2010.
From its two-dimensional nature and its electronic energy spectrum graphene derives many outstanding properties. They are highlighted by prof.Geim nice picture of graphene, quoted above, and are discussed through this chapter. First the structural and mechanical characteristics of the system are revised. Then the electrons behaviour and their similarity to Dirac fermions are examined, together with the subsequent electric and transport properties. An overview of the main applications in the field of electronics is also given. A final discussions about the presence of defects on the graphene plane and the rise of possible magnetic interactions will help to introduce the main topics of the present study.

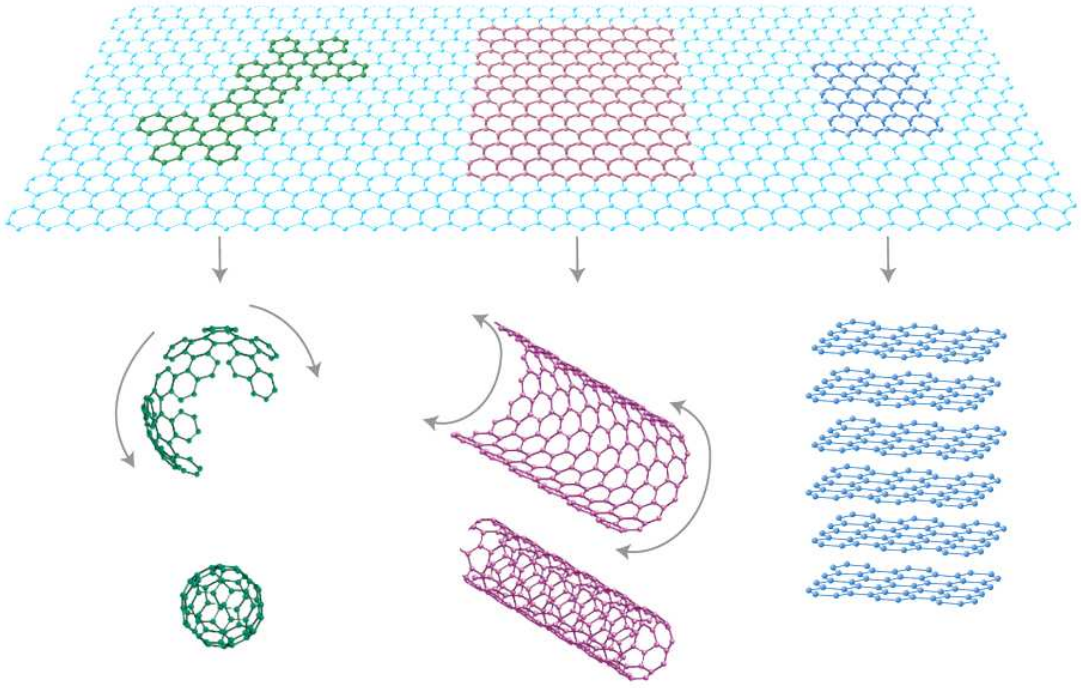

Figure 2. The graphene plane seen as the building block for all other carbon allotropes: from left to right wrapped into 0DIM fullerenes, rolled up in 1DIM nanotubes and stacked to form 3DIM graphite. Adapted from [15].

1.1 Graphene structure

In a first ideal approximation, graphene can be described as a planar carbon sheet, only one atom thick. The atoms display sp^2 hybridization and are arranged in an honeycomb lattice, with a carbon-carbon bond distance of 1.42Å. Thus graphene unit cell is hexagonal and contains two carbon atoms. Its crystal structure shall be seen as two identical, interpenetrating triangular sublattices, evidenced in fig. 3: this distinction not only helps to define the stacking order in multilayer graphene and graphite[1], but it's also intimately connected to the electronic properties of the system, as will be explained later. The graphene plane may be terminated either by *armchair or zig-zag edges*, topologically speaking the two possible ways to cut an hexagonal lattice. As an example fig.4b shows the alternation of armchair and zig-zag edges in a real graphene sample, observed with Scanning Tunneling Microscopy[2].

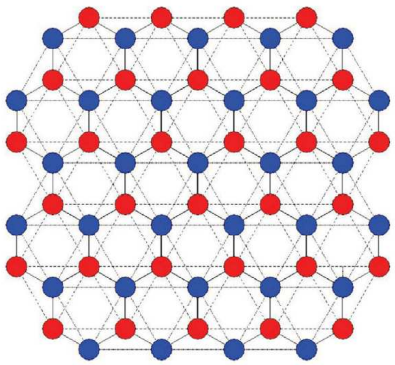

Figure 3. Graphene structure. Blue and Red carbon atoms marks the two different triangular sublattices.

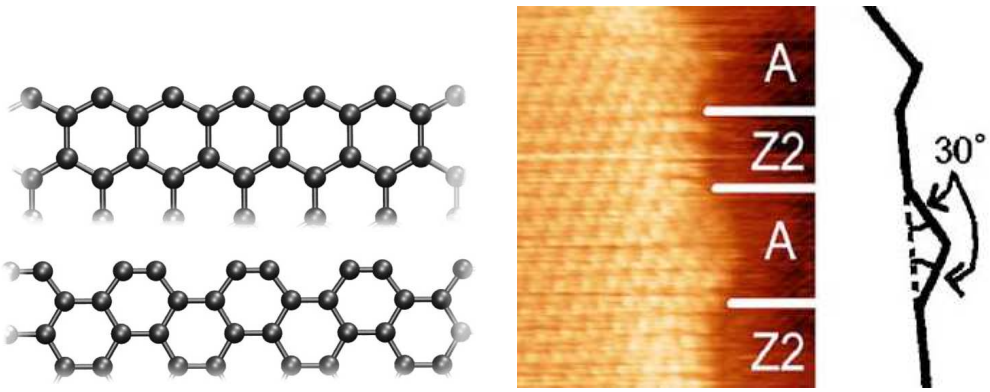

Figure 4. **(a)**Schematic representation and **(b)**STM image of the Zig-Zag and Armchair conformations at graphene edges. Adapted from [16].

Graphene was first obtained in 2004 from highly oriented pyrolytic graphite by the micromechanical cleavage technique [14], i.e. scotch-tape peeling of graphite surface.

[1]In graphitic materials the stacking order indicates the mutual position of subsequent layers. Graphite usually display the Bernal stacking ABAB, where one sublattice in layer B results aligned with the centers of the hexagons of layer A.

[2]Further detail on graphene edges will emerge while discussing their peculiar electronic states.

The novel idea which made possible the discovery of graphene and then valued the Nobel prize for physics to Novoselov and Geim, was the development of a method to probe the existence of single layer samples, based on the combination of optical interferometry and atomic force microscopy[3]. From the time of these first experiments, different more effective techniques have been developed to monitor the existence of single layer graphene, featuring Raman [18], Angle-Resolved PhotoEmission Spectroscopy [19], electron microscopies [20] and nanobeam electron diffraction [21]. The latter method was the first one to allow important insights in graphene structure and it is worth discussing it here, while for the other techniques the reader may refer to section 3.2 and to several recent reviews [20, 22]. Figure 5 displays the ED pattern of graphene at several incidence angles. No sudden intensity variation are observed in any of the diffraction peaks, as expected for monolayer graphene, whose reciprocal space is a set of equal rods (fig.7a). For the case of multilayer graphene, instead, simulations yield a non-monotonic behaviour, due to the more complex geometry in the Fourier space. The experimental and simulated intensity profiles are shown in the lower panels.

The observation of monolayer graphene seems to prove the existence of strictly 2DIM crystals and is therefore a great surprise. As first discussed by Landau [23] and Peierls[24] in the 30s and then formalized in the Mermin and Wagner theorem [25], long-range crystalline order should not exist in less than three dimensions. Indeed they proved that in one or two dimensions, within the harmonic approximation, the number of long wavelength phonons diverges at the thermodynamic limit: the induced dynamical fluctuations would exceed the limit of 1/10 of the lattice constant and, according to the Lindemann criterion, the material would melt.
Low-dimensional crystals are therefore not thermodinamically stable, as observed during the first CVD growth of graphene, which tended to collapse towards 3DIM nanostructures. In the graphene crystal these destructive fluctuations are suppressed by anharmonic coupling of the C-C bending and stretching phonon modes, which give rise to nanoscaled corrugations, called *ripples* (see fig.6).

[3]This method will not be used through this work and hence there is no need to explain it in detail here. Nevertheless it may deserve a short description: Geim's group observed (supp.inf. from [14] that graphenes prepared on a SiO_2 wafer (with a proper thickness, they used 300 nm), through transparent to visible light, can be detected in interferometry experiments, as the added optical path shifts the interference colors. In particular for graphenes with less than 3 layers this effect proved too small to be appreciated (see the supporting information from [14],fig.S2 therein. Thanks to recent improvements, this method now allow the observation of monolayers [17].). These optical measurements allowed to select few-layers graphenes among multilayers one, while SEM and AFM were used to determine the exact number of layers. AFM shows a thickness of approximately 1 nm for the first layer (these number will become clear later in the text) and additional 0.334 nm for each further sheet.

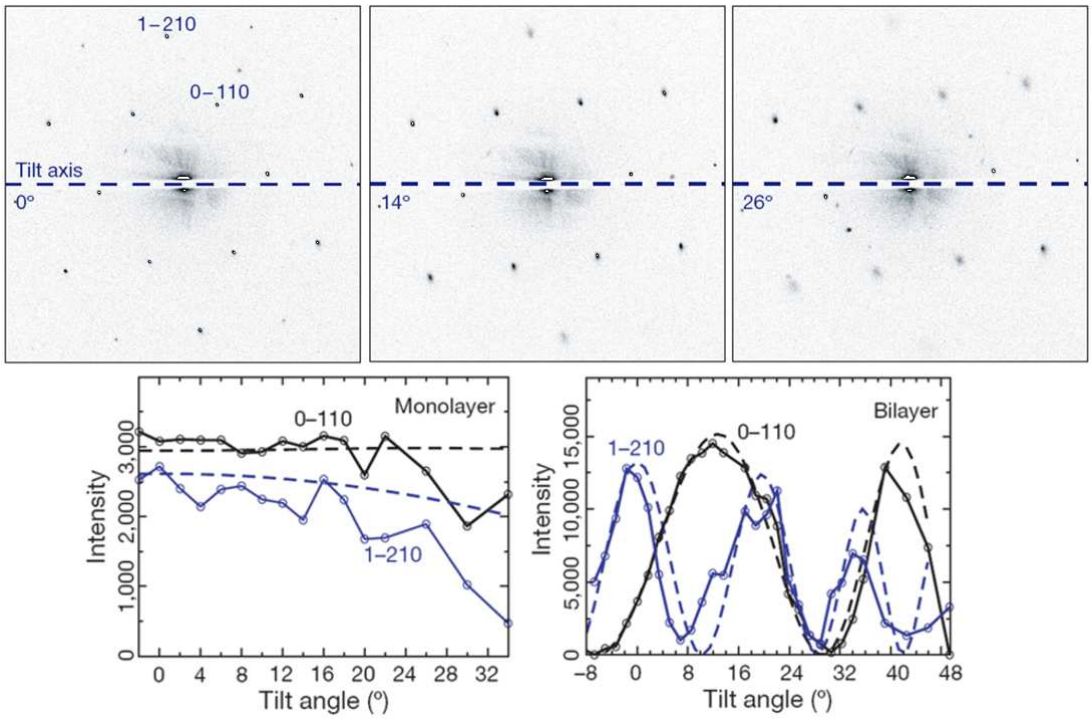

Figure 5. Electron diffraction from monolayer graphene. Above: diffraction patterns at different incidence angles. Below: intensity of Bragg reflections measured (point and solid lines) and expected (dashed lines) for single and bilayer graphene. Adapted from [21].

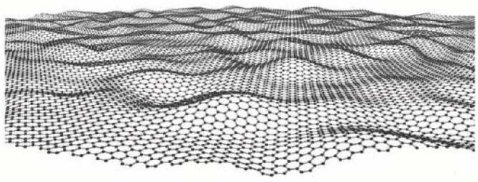

Figure 6. Schematic representation of ripples, the nanoscopic corrugations present on the graphene plane. On average their size ranges between 5 and 25 nm and they are $\sim 1\,nm$ high.

To this extent, graphene structure is not strictly 2DIM and then reconciles to the Mermin and Wagner theorem. Actually ripples are observable also in the electron diffraction patterns discussed above (fig.5): one can easily see a broadening and blurring of the diffraction peaks with increasing tilt angle, effect even larger for points farther away from the tilt axis. This broadening, also considering that the total intensity of the peaks does not vary, implies that the reciprocal space of graphene is better represented by fig.7b, where rods wander about their average directions. Correspondingly, in the real space, the graphene plane assume many different orientations. In particular, since the broadening is isotropic, the observed "waviness" is randomly oriented. Further analysis of the electron diffraction patterns of different samples [21], reveals that graphene surface deviates from its average plane by $\pm 5°$. The ripples are found to be on average $1\,nm$ high and from several to $25\,nm$ large. These nanoscopic corrugations are typical of monolayer graphene and rapidly disappear in multilayer samples (fig.7c).

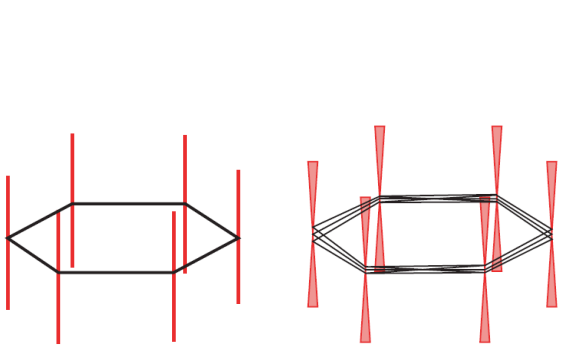

(a). Reciprocal Space of an ideal 2DIM hexagonal lattice.

(b). Reciprocal space of corrugated graphene.

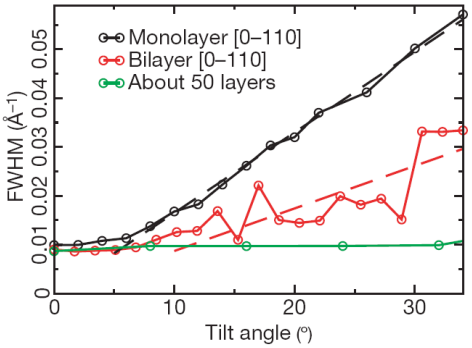

(c). Gaussian FWHM of the (0-110) diffraction peaks, as a function of tilt angle, for mono- and multilayer graphene.The apparently flat region between 0 and 5° is due to sensitivity issues.

Figure 7. Analysis of the electron diffraction patterns. The broadening of the diffraction peaks - black data in panel (c) - indicates the reciprocal space of graphene is not the set of rods expected for an ideal hexagonal plane (a), but is rather represented by cones around the average directions (b). From [21].

1.2 Mechanical properties and Applications

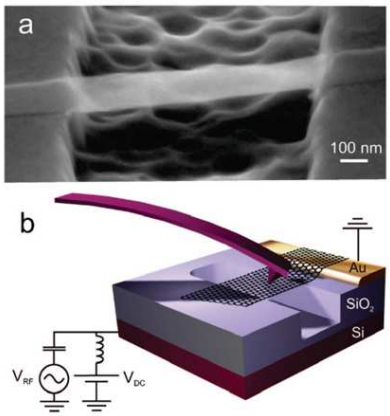

Figure 8. **(a)** SEM image and **(b)** schematic representation of a suspended graphene resonator, used for the measurements of graphene mechanical properties. From [26].

Graphene is an extremely light-weight material, a hundred times stronger than the strongest steel and it's then exceptionally promising for mechanical applications in the nextcoming future. It is the thinnest material ever observed, with a density that can be estimated from the lattice parameters to be 0.77 mg/m^2 [27] and nevertheless graphene exhibit record mechanical properties: measurements performed on suspended sheets with an AFM tip [26, 28] allowed to estimate its spring constant to be of the order of several N/m and the Young modulus to be approximately 1 TPa. Finally its breaking strength is evaluated in 42 N/m: this means that, as described by the Royal Swedish Academy of Science in the documentation for the Nobel prize [27], a fictional hammock of 1 m^2 made out of graphene[4] would hold a cat while weighting less than 1 mg. Com-

[4]Actually graphene sheets 1 m^2 large are no more science fiction. Researchers at Sung Kyun Kwan University, Korea, in cooperation with Samsung, have presented such large graphene sheets in summer 2010. Further information about their published results will be discussed later in the section about electronics application.

pared to a steel film as thick as the interlayer separation in graphite, 3.34 Å, graphene results more than 100 times stronger than the strongest steel, which exhibit a 2DIM breaking strength of 0.4 N/m. Graphene is thus "the strongest material ever measured" [28] and it's also ductile and flexible, in spite of its brittleness.
In front of these outstanding mechanical properties of suspended graphene layers, some questions arise : can these properties be transferred to macroscopic materials? Could one produce graphene-based fibers or paper for large-scale structural applications? Recently different examples of carbon-based materials have been developed (see fig.9): graphene and graphene oxide paper [29, 30], graphene films [31, 32, 33], and carbon nanotubes sheets [34], films [35] and fibers [36]. Unfortunately none of these materials keep the original strength of graphene or CNT: buckypaper is comparable to ordinary paper, while graphene oxide sheets are the best performing and shows about one tenth of the original tensile strength and Young modulus. As discussed by prof.Pugno in a recent work [37], could one reduce this frustration of the scaling-up processes? How? Several strategies have been suggested to increase the mechanical properties of

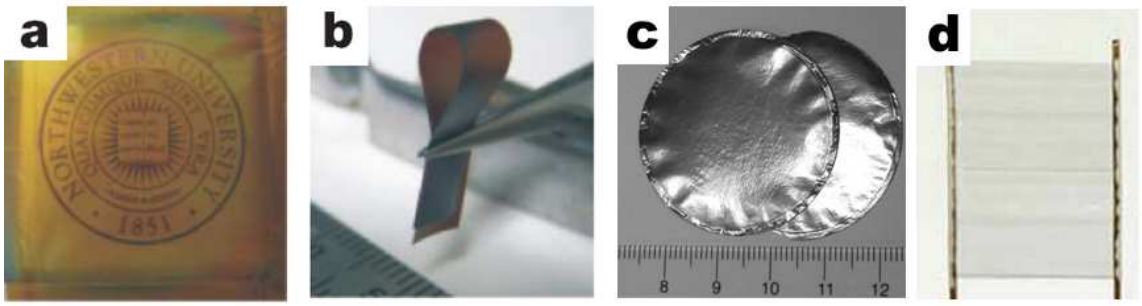

Figure 9. Examples of macroscopic graphene-based materials: **(a-b)** Graphene oxide paper, **(c)** Graphene paper, **(d)** carbon nanotubes sheets (adapted from [30, 29, 38]).

macroscopic graphene-based systems, like the engineering of extra cross-links among graphene layers [37, 30], but up to now the most successful approach has been to use graphene as an ingredient for composite materials [39]. Studies from the research group of prof. Nikhil Koratkar at Rensselaer Polytechnic Institute [2, 40] have shown that «graphene is far superior to carbon nanotubes or any other known nanofiller in transferring its exceptional strength and mechanical properties to a host material. For example epoxy composites, which are usually brittle and prone to fracture, greatly enhance their mechanical performances when mixed to graphene»[5]. Even a concentration of 0.1% in weight is enough improve the stiffness and strength of the material up to the performances obtained when adding carbon nanotubes at much higher (1%) concentration.

[5]From an interview to prof.Koratkar appeared on *Inside Rensselaer* [40].

Indeed graphene has 3 major advantages over CNT in these applications [40]:

The large surface area. As a planer sheet, graphene benefits from considerably more contact with the polymer matrix than CNT.

The surface roughness which also helps to interlock graphene in the host material and derives from the high density of surface defects, resulting from the thermal exfoliation processes used to manufacture bulk quantities of graphene[6].

The 2 dim geometry which is effective in reducing cracks propagation inside the composite. When a crack encounter a graphene sheet it's forced to deflect or to twist around the sheet, so that a large part of its propagation energy is adsorbed. Graphene has been shown to improve the composite's resistance to fatigue crack propagation by almost two orders of magnitude [2].

Advanced composites are increasingly important in new windmill blades, aircraft components and other applications requiring ultralight, high strength materials; and graphene demonstrates to be the best candidate to enhance the performances of these materials.

Mechanical applications of graphene, however, are not limited to the macroscopic scale. In particular two interesting ideas have been developed to exploit the record mechanical properties of graphene at the nanoscopic scale and deserve to be mentioned: electromechanical resonators [41, 42] and pressure and strain sensors [43].

1.3 Inside Graphene: Electronic Properties of a bidimensional material

Most of the scientific excitement about graphene has been focused on its electrons: their linear dispersion relations and the similarity to relativistic Dirac Fermions, explored in this section, are the basis for fascinating transport properties, including ballistic conduction and the quantum hall effect, which will be discussed afterwards.
As already mentioned, the electronic energy spectrum of graphene was first derived by Wallace [13] in 1947, in the standard tight-binding approximation. The details of these calculations can be found in the original paper and are thoroughly discussed in a recent review [44] by Castro Neto and coworkers[7].

[6] Chemical methods for the production of gram-scale quantities of graphene and the corresponding defects' concentration are discussed through chapter 3.

[7] The reader can found in this paper, published on Reviews of Modern Physics, a complete discus-

Qualitatively each carbon atom is in the sp^2 hybridized state and uses these three hybrid electrons to form the C-C bonds of the hexagonal lattice (the corresponding molecular orbitals, sketched in fig.10 are labelled σ). The exceptional strength of these bonds is the basis of many of the outstanding properties of graphene and carbon nanotubes. The linear combination of the remaining atomic orbitals (LCAO), one per carbon atom, may be used to compute the resulting energy bands. **In correspondence to the two sublattices of graphene the π electrons give rise to two bands** whose functional form is expressed as

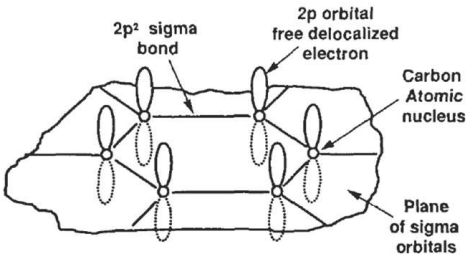

Figure 10. σ and π molecular orbital on the graphene plane.

$$E_{\pm}(\vec{k}) = \pm t_1 \hbar \sqrt{3 + \mathcal{F}(\vec{k})} - t_2 \hbar \mathcal{F}(\vec{k}) \tag{1.1}$$

$$\mathcal{F}(\vec{k}) = 2\cos(\sqrt{3}k_y a) + 4\cos\left(\frac{\sqrt{3}}{2}k_y a\right)\cos\left(\frac{3}{2}k_x a\right)$$

where $a = 1.42$Å is the C-C distance, $\vec{k}$ is the electronic wavevector, t_1 and t_2 are respectively the nearest and next-nearest neighbours hopping energies and the plus and minus signs apply to the upper (conduction) band π^* and to the lower (valence) band π.

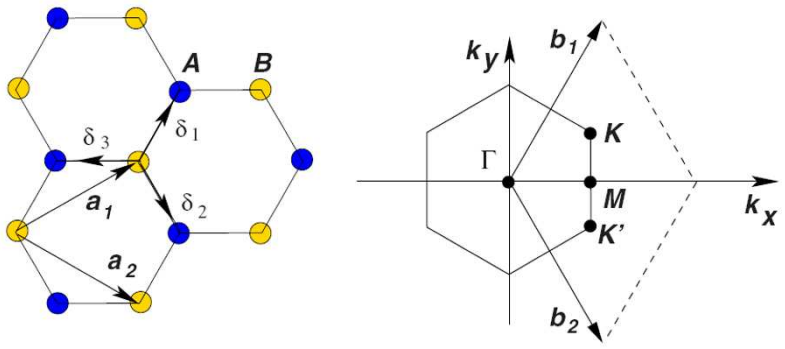

Figure 11. The graphene lattice and its Brillouin zone. $\vec{a_1}$ and $\vec{a_2}$ are the lattice unit vectors, $\vec{b_1}$ and $\vec{b_2}$ the unit vectors in the reciprocal space.

These two bands touch each other at the corners of the Brillouin zone, in the points K and K'. Near these points expanding the wavevector as $\vec{k} = \vec{K} + \vec{q}$, $|q| \ll |K|$

sion of the electronic properties of graphene, as well as many mathematical details. In the present study only an overview of the main results is given.

equation 1.1 reduces to

$$E_{\pm}(\vec{q}) = \pm\frac{3}{2}at\hbar|q| + \mathcal{O}\left[q^2/K^2\right] = \pm\hbar\, v_F\,|q| \tag{1.2}$$

Opposite to the usual case where $E(\vec{k}) = \frac{\hbar^2 k^2}{2m}$, **the dispersion relations in this region result linear** and the speed of the charge carriers does not depend any more on their momentum, but it assumes the constant value $v_F = 3at/2 \simeq 1 \cdot 10^6\, m/s$, called the Fermi velocity.

This peculiar dispersion law also reflects on the charge carrier interactions. In a normal metal, with parabolic dispersion, the electronic kinetic energy is proportional to the charge surface density $K \propto \sigma$ while Coulomb repulsion depends on its square root $U \propto \sigma^{1/2}$. Then below a certain threshold σ_0 electron correlations prevail, while at higher charge concentration the system behaves as a weakly interacting electrons gas, known as the Fermi liquid. In graphene, on the contrary, also the kinetic energy depends on the square root of the charge density, so that the ratio $\frac{U}{K}$ assume the constant value $\alpha = \frac{e^2}{\epsilon\hbar v_F}$ known as graphene's *fine structure constant*.

Graphene is then a zero-gap semiconductor (or semimetal), with symmetric valence and conduction bands and linear dispersion relations near the Fermi energy (see fig.12).

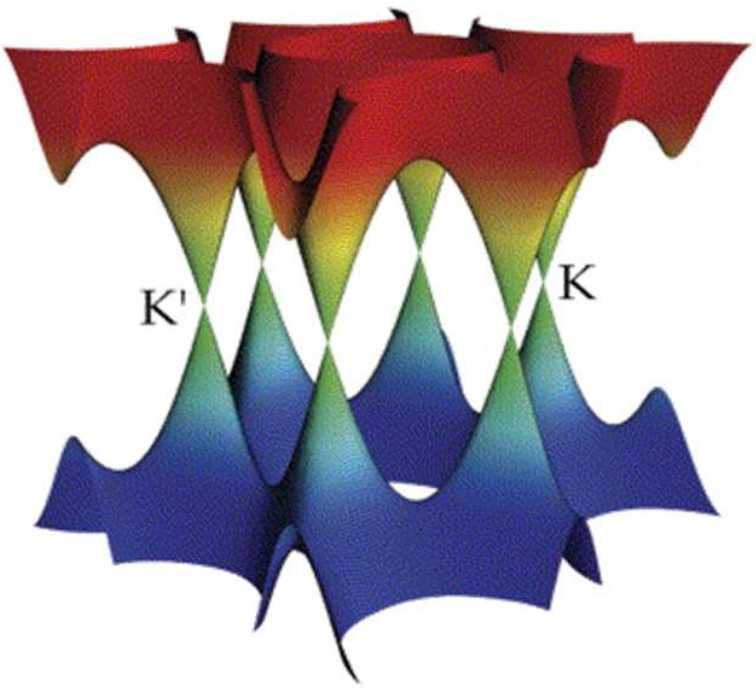

Figure 12. Electronic energy bands in graphene. The valence and conduction band assume conical shapes near the Fermi energy, in correspondence to linear dispersion relations. The material is a zero-gap semiconductor.

This peculiar energy spectrum is strictly analogue to that of fermions satisfying the relativistic Dirac equation, bringing to the conclusion that **charge carriers in graphene behaves as massless Dirac particles**. It's then convenient to review in detail how and to which extent the properties of Dirac fermions trace back to the electrons in graphene.

1.3.1 Chiral Dirac fermions in graphene

Linear dispersion relations and Energy Gap

First it's useful to illustrate the similarities in the energy spectra of graphene electrons and Dirac fermions. The latter display an energy gap proportional to the rest mass of the particles $E_{GAP} = 2\,E_0 = 2\,mc^2$ and above E_0 the energy follow the linear dispersion relation $E(\vec{q}) = \hbar c|q|$.

In graphene there's no energy gap and correspondingly the charge carrier must be considered to have *zero effective mass*. Linear dispersion relations are then valid for any energy near the Dirac points and, as seen in eq. 1.2, the Fermi velocity $v_F = c/300$ takes the place of the speed of light.

Existence of antiparticles

One of the major results of Dirac theory is the existence of antiparticles. In graphene the role of particles and antiparticles are played by electrons and holes, which display exactly symmetrical behaviours, as is evident from the electric measurements displayed in figure 15 below.

Charge conjugation symmetry

Particles and antiparticles are expected to be represented by identical wavefunctions (spinors), distinguished only by their spin component[8]. The role of the (pseudo)spin in graphene is played by the different sublattices A and B. In particular, in the basis set of momenta, the eigenstates of the bidimensional Dirac equation

$$-i\,v_F\,\vec{\sigma}\cdot\vec{\nabla}\psi(\vec{r}) = E\,\psi(\vec{r}) \tag{1.3}$$

are symmetrical for the two sublattices, i.e. near K and K', and can be written as [44]

$$\psi_{\pm,K}(\vec{k}) = \frac{1}{\sqrt{2}}\begin{pmatrix} e^{-i\theta_k/2} \\ \pm e^{i\theta_k/2} \end{pmatrix} \qquad \psi_{\pm,K'}(\vec{k}) = \frac{1}{\sqrt{2}}\begin{pmatrix} e^{i\theta_k/2} \\ \pm e^{-i\theta_k/2} \end{pmatrix}. \tag{1.4}$$

[8]This symmetry property is called the charge conjugation symmetry.

Here the plus and minus signs correspond to the two possible energy eigenvalues $\pm\hbar v_F k$, that is to the π^* (electrons) and π (holes) bands [9]. Actually the useful quantity to distinguish the electrons-holes symmetry is the *chirality* or *helicity*, defined as the projection of the pseudospin along the direction of motion:

$$\mathbf{h} = \frac{1}{2}\hbar\vec{\sigma}\cdot\hat{k} \qquad . \tag{1.5}$$

One can notice that the energy eigenstates are also eigenstates of $\mathbf{h}$ and can then write [44]

$$\mathbf{h}\,\psi_{\pm,K}(\vec{r}) = \pm\frac{1}{2}\psi_{\pm,K}(\vec{r}) \qquad \mathbf{h}\,\psi_{\pm,K'}(\vec{r}) = \pm\frac{1}{2}\psi_{\pm,K'}(\vec{r}) \qquad .$$

According to these last equations, electrons and holes respectively have a well-defined positive and negative helicity, indipendently if they are located in the K or K' valley. This is how charge conjugation symmetry is reflected in graphene.

Please recall that the Dirac equation in graphene is valid only in the limit of low energy excitations, where dispersion curves follow the linear regime. Far away from the Fermi energy this approximation is no longer valid and helicity is no more well-defined.

1.3.2 Electronic Edge States

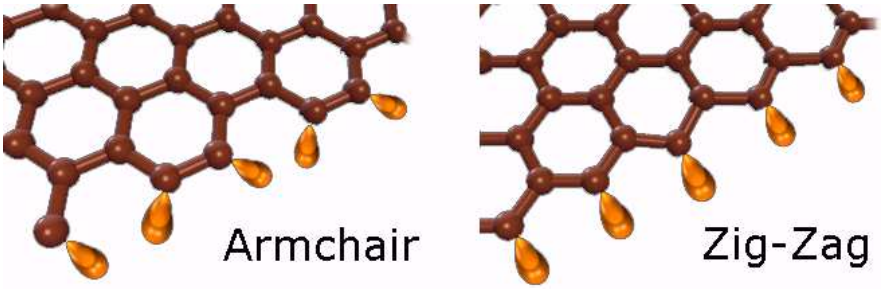

Figure 13. σ dangling bonds at graphene armchair and zigzag edges.

Electrons behaviour is completely different at the edges of the graphene layer, where geometry and localization effects play the major role. Each carbon atom at the edge has one of its sp^2 electrons free form the carbon network. Usually most of these orbitals are saturated by atomic hydrogen or hydroxyl groups and, in a few cases, by larger functional groups. However, if the sample is annealed under vacuum at sufficiently high

[9] Notice that in both the given eigenfunctions (due to the factor 1/2) a 2π rotation of the phase θ causes the wavefunction to change sign, that is introduce a phase difference of π. This change of phase is typical of spinors and is called the Berry's phase [38].

temperature (above 750°C) [45, 46], or if the edges are generated in inert atmosphere, it is possible to have these σ electrons unbound, as sketched in the figure. In this case they're named *dangling bonds*. On the zigzag edge, where atoms are all identical, the dangling bonds are perpendicular to the edge line, while on the armchair edges they preserve the hexagonal symmetry.

The behaviour of *pi* electrons further distinguish the two edge configurations. Indeed along the zigzag edge they combine to form a unique quasi-localized electronic state, distributed along the edge (fig.14). Its electron density decay exponentially while entering the graphene sheet and its penetration depth, function of the electron wavector, is typically of the order of a few atomic rows. This electronic state was first derived theoretically by Fujita in 1996 [47] and then experimentally observed by Scanning Tunneling Microscopy in 2005 [16, 48, 49].

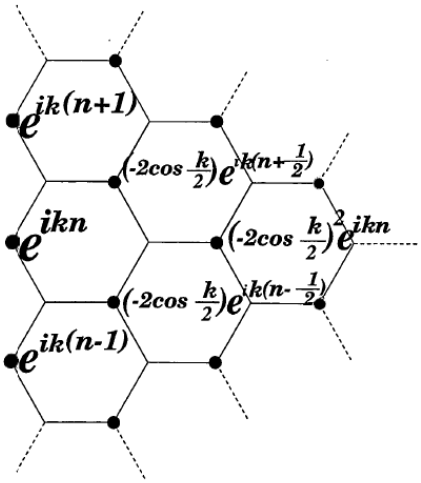

(a). Schematic representation of the quasi-localized state originating from π electrons at graphene zigzag edge. Adapted from [47].

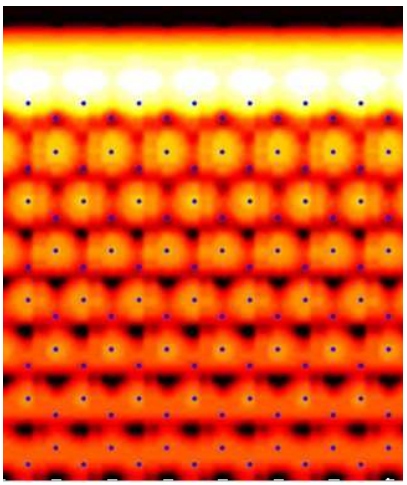

(b). Simulated STM image (constant current mode) of graphene zigzag edge. Adapted from [50].

Figure 14

In the present work these edge states have been investigated by μSR spectroscopy and their characterization is shown in chapter 4. Mechanical high energy ball-milling of graphite in Argon atmosphere was used to obtain samples with a high concentration of edges and dangling bonds.

1.4 Transport Properties

Thanks to the relativistic behaviour of the electrons and to their zero effective mass, exceptional transport properties are observed in graphene. The following paragraphs, far from an exhaustive description of graphene's physical properties, will outline only the main phenomena observed. These will made apparent why graphene has gather so much interest from the scientific community and why it is considered a useful material for future technological applications[10].

1.4.1 Conductivity in graphene

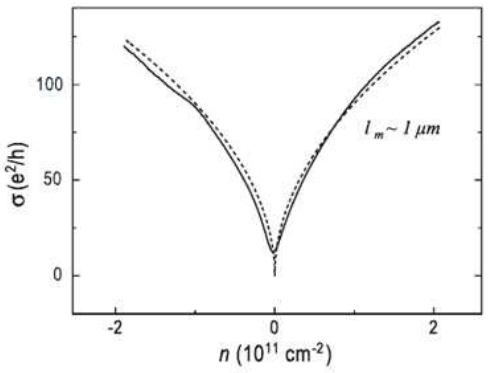

Figure 15. Conductance of a suspended graphene sample as a function of carrier density at 40 K. Carrier density is controlled by a gate voltage. The dashed line indicates the behaviour theoretically expected for ballistic conduction.

Charge transport is characterized by ballistic conduction, with large mean free path and extremely high mobility. In the first graphene samples, produced by the scotch tape technique and deposited on silicon oxide substrates, mobility at room temperature was of the order of 2 000 $cm^2 \,/\, V\,s$ [53], value probably inhibited by an high concentrations of defects. Rapidly, improvement of sample preparations and removal of adsorbed molecules led to devices with mobility higher than 20 000 $cm^2 \,/\, V\,s$. In these systems, charge carrier diffusion is limited by scattering from charged impurities and from the phonons of the substrate [54, 55]. Indeed recent measurements on free-standing graphene [56, 57] highlighted a mobility increased by another order of magnitude with respect to the first samples, exceeding 200 000 $cm^2 \,/\, V\,s$. This value and the measured dependence on charge carrier concentration (fig.15) have confirmed the expectations in case of **ballistic transport**, with mean free paths on the micrometer scale ($l \simeq 1\,\mu m$)[11]. As it is evident from this exceptional mobility, the electron-phonon interaction in graphene is small and will not be discussed here. The reader can find a detailed account on this topic in a recent paper by Mariani and von Oppen [60].

[10] For the mathematical aspects of transport phenomena in graphene the reader should refer to the works of Gusynin and Sharapov [51], Adam and coworkers [52] and to the already cited review [44].

[11] Notably the same characteristic length scale apply to spin transport, allowing the fabrication of graphene-based spintronics devices [58] and the observation of Andreev reflections [59].

Figure 15 also shows that, despite the density of states vanishes in the zero-energy limit, conductivity never drops below a minimum value, namely e^2/h (or, equivalently, resistivity never exceeds 6.45 $k\Omega$). This minimum conductivity is observed only in monolayer graphene [61] and is an instrinsic property of bidimensional Dirac fermions. Indeed in such systems no localization effects are expected [62] and Mott's argument [53] for metals can then be used: this states that the mean free path of charge carriers cannot be shorter than their wavelength at the Fermi energy λ_F. For the case graphene, the corresponding minimum conductivity turns out to be $\sigma \simeq e^2/h$, as experimentally observed.

1.4.2 Magnetotransport: the anomalous QHE and SdH oscillations

The first experimental proofs of the presence of Dirac fermions in graphene came from magnetotransport measurements. Indeed standard devices like the one shown in fig.16, made out from deposited as well as suspended graphene, allowed to easily observe the half-integer quantum Hall effect and Shubnikhov-de Haas oscillations [53, 38], already from the beginning of graphene's story. In the following, the characteristics of these phenomena in graphene are described and are shown to be fully consistent to the Dirac-like energy spectrum.

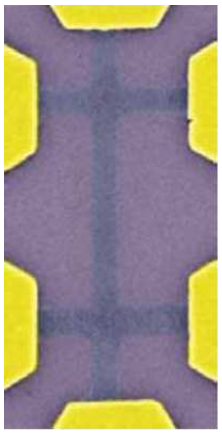

Figure 16. SEM micrograph of a graphene (dark violet) device for Hall measurements.

According to classical physics, in two dimensions electrons subjected to a magnetic field $\vec{B}$ (perpendicular to the plane) follow circular orbits with the so-called cyclotron frequency $\omega_c = \frac{eB}{m}$. When the field is large enough compared to thermal energy $\hbar\omega_c \gg k_B T$ these orbits are quantized and their possible energies are given by

$$E_N = \pm\left(N + \frac{1}{2}\right)\hbar\omega_c \quad . \tag{1.6}$$

For the case of relativistic fermions in graphene this equation becomes

$$E_N = \pm v_F\sqrt{2e\hbar\, B\, N} \quad . \tag{1.7}$$

These Landau Levels are plotted in figure 17 as a function of magnetic field for both cases. When increasing the magnetic field the degeneracy of each Landau level also increase, that is, the higher energy levels gradually empty and all the electrons fall into the lower energy states. This is represented in fig.18.

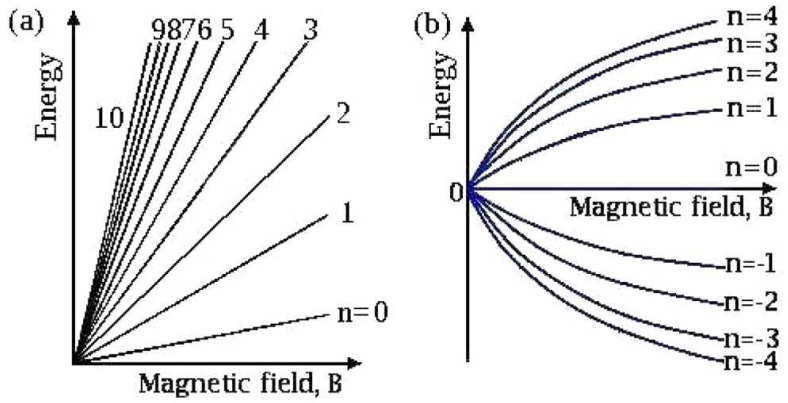

Figure 17. Landau energy level of a charged particle in a strong external magnetic field $\vec{B}$. (**a**) for a bidimensional electron gas in a normal metal and (**b**) for the case of graphene.

For a normal metal or small-gap semiconductor, each time the Fermi energy crosses a Landau level (as in fig.18b) we have a sharp maximum in the density of states at the Fermi energy and consequently a minimum is observed in the **longitudinal resistivity** ρ_{xx}. As a function of the applied field, $\rho_{xx}(B)$ thus display the well known Shubnikov-de Haas oscillations. They're displayed for the case of graphene in fig.19.

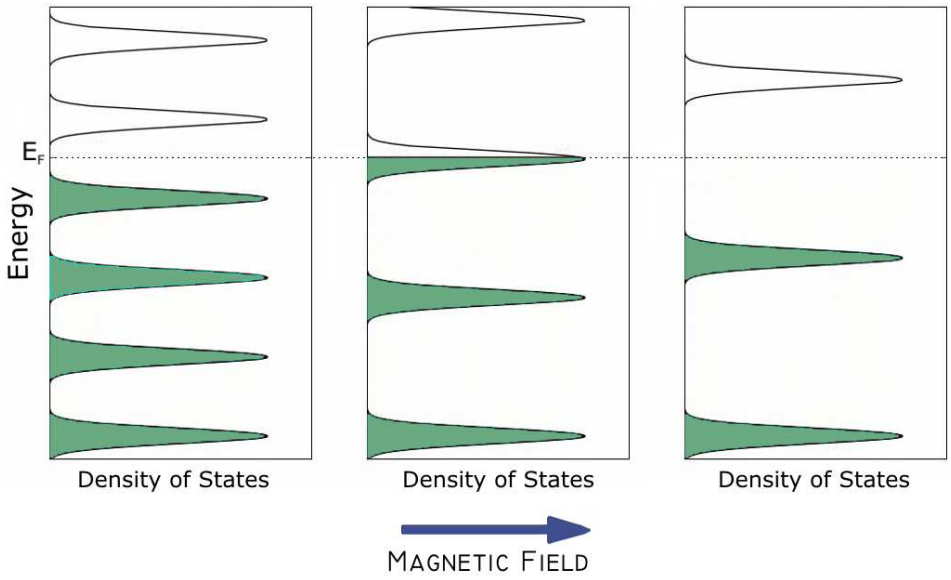

Figure 18. Density of electronic States in the Landau Levels. At constant Fermi Energy, the degeneracy of the levels increases for increasing magnetic field (the DoS "stretches" in energy). Each time a Landau level empties (its energy exceeds the Fermi energy, panel b) a new plateau in the QHE and a new maximum in SdH oscillations are observed.

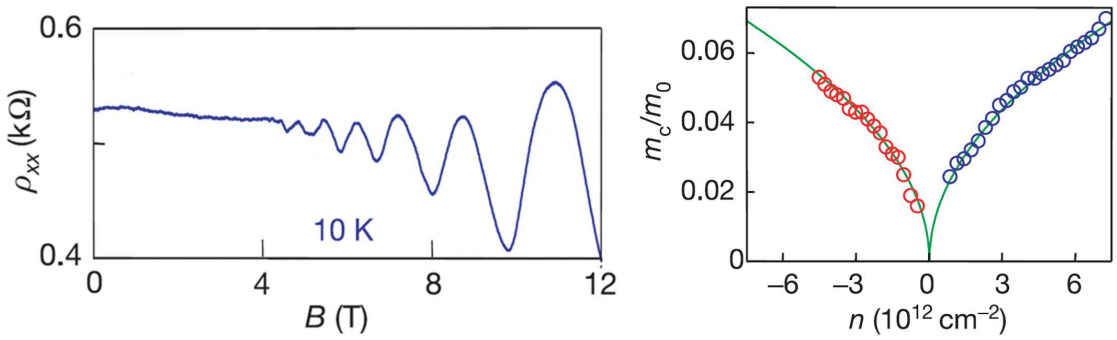

Figure 19. **(a)** Shubnikov-de Haas oscillations in monolayer graphene at 10 K. **b** Cyclotron Mass as a function of carrier concentration, extracted from the experimental data according to eq.(1.8). The square root dependance is consistent with the linear energy spectrum. Adapted from [53].

Three important features have emerged from the investigations of such oscillations:

1. the resistivity show maxima rather than minima when the energy matches a Landau level. This can be seen as a manifestation of Berry's phase or, equivalently, can be traced back to the existence of a Landau level at the charge neutrality point, which will be further discussed below.

2. the fundamental frequency of SdH oscillations follow a linear dependance as a function of the charge carrier concentration n, as expected in any 2DIM system $B_{SdH} = \beta\, n$. The measured value of $\beta = 1.04 \cdot 10^{-15}\, T\, m^2$ [53] can be related to the degeneracy d of each electronic state, yielding $d = 4$, as expected for graphene due to the double-valley (K, K') and double-spin degeneracy.

3. from the temperature dependance of the oscillations amplitude A it is possible to extract the cyclotron mass m_c of the charge carriers[12] thanks to the expression [53]

$$A = \frac{T}{\sinh\left(\frac{2\pi^2 k_B T m_c}{\hbar e B}\right)}\,. \tag{1.8}$$

The cyclotron masses estimated from the experiments follow a square root dependence on the carrier concentration $m_c \propto n^{1/2}$, result that is fully consistent with the linear dispersion relations (eq. 1.2). Indeed, called $A(E) = \pi k^2$ the area of Landau orbits in momentum space, the following relations hold

$$\begin{aligned} B_{SdH} &= \tfrac{\hbar}{2\pi e}\, A(E) \\ B_{SdH} &= \tfrac{h}{4e}\, n \end{aligned} \qquad \Longrightarrow A(E) \propto n$$

[12] SdH oscillations in single-layer graphene are exactly identical for holes and electrons.

$$\begin{aligned} m_c &= \tfrac{\hbar^2}{2\pi}\tfrac{\partial A(E)}{\partial E} \\ m_c &\propto n^{1/2} \end{aligned} \qquad \Longrightarrow \frac{\partial A(E)}{\partial E} \propto n^{1/2}$$

yielding

$$A \propto \left(\frac{\partial A}{\partial E}\right)^2 \implies A \propto E^2 \implies E \propto k \quad .$$

At higher magnetic fields, when a few Landau Levels are populated, also the quantum Hall effect (QHE) becomes visible in the **transversal magnetoconductivity** σ_{xy}. In the case of a standard electron gas, under increasing magnetic field, conductivity plateaux are expected for integers value ν of the conductance quantum $\nu\,(\frac{4e^2}{h})$ and a step between two subsequent conductance eigenstates is observed when the Fermi level crosses one of Landau energies. No plateaux are present for $\nu = 0$. On the contrary, in the case of graphene, the plateaux are observed for half-integer values ν of the conductance quantum $\left(N + \frac{1}{2}\right)\,(\frac{4e^2}{h})$ and the sequence is not interrupted across zero, when switching from holes to electrons (both the plateaux for $\nu = \pm\frac{1}{2}$ are observed).

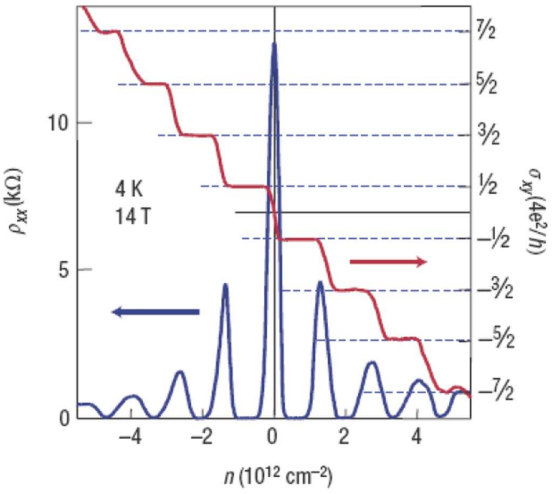

(a). QHE at low temperature (4 K), in a constant field of 14 T.

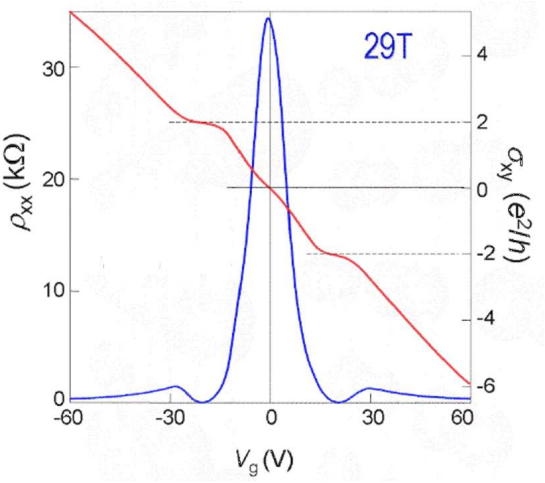

(b). QHE at room temperature, in a strong magnetic field of 29 T.

Figure 20. Quantum Hall Effect in graphene. Measurements are taken at constant magnetic field, as a function of the carrier concentration (gate voltage).

To explain this unique quantum Hall effect, it is necessary to have a closer look to graphene's Landau levels (LL) expressed by eq. (1.7)

$$E_N = \pm v_F\sqrt{2e\hbar\,B\,N} \quad .$$

This relation implies the existence of a LL $N = 0$ at the charge neutrality point (zero energy). Holes and electrons equally contribute to the population of this level, but

they assume only one value of the pseudospin, so that the total degeneracy is the same as in all other eigenstates[13]. In correspondence to its compound population, the $N = 0$ LL is responsible for both the $\nu = \pm\frac{1}{2}$ conductivity plateaux. Apart from this shift by $\frac{1}{2}$, Hall conductivity in graphene display the regular integer steps, resulting in an equispaced ladder at half-integer values of ν.
Thanks to the zero effective mass of the charge carriers and to their low scattering rate in good-quality graphene, the Quantum Hall Effect and Shubnikov-de Haas oscillations can be detected even at room temperature (see fig. 20b).

These last observations are rather impressive, in particular as one may expect that the existence of ripples, bringing field inhomogeneities up to $1\,T$, should quench the QHE already at low temperature. Actually the Atiyah-Singer index theorem can be invoked to show this does not happen in graphene [53, 63]: this theorem, important for superstrings and quantum field theory, guarantees that, as the Landau states are chiral, they're also invariant for gauge fields and space curvature. As a consequence ripples cannot inhibit the QHE [14].

1.4.3 Thermal properties

The electronic properties of graphene, especially the zero effective mass of the charge carriers and their high mobility, reflect into its thermal transport characteristics. Graphene is an exceptional thermal conductor, with conductivity values in the range $4800 \cdots 5300\,\frac{W}{mK}$ at room temperature [64]. This figure can be compared to the thermal conductivities of copper ($400\,Wm^{-1}K^{-1}$) and of graphene "competitors", the parent compounds diamond ($2200\,Wm^{-1}K^{-1}$) and carbon nanotubes ($3000 \cdots 5000\,Wm^{-1}K^{-1}$ [65]). This outstanding conductivity, together with its mechanical stiffness and its lower cost with respect to carbon nanotubes, makes graphene the material of choice for the production of new heat sink devices.

[13] These characteristics of the $N = 0$ LL make it different from all other levels. Each LL for $N \neq 0$ is populated by either holes or electrons (according to the + or − sign), independently of their pseudospin.

[14] In its general formulation, the Atiyah-Singer index theorem states that, under proper conditions, the *analytical index* of an elliptical differential operator equal the *topological index* of the manifold on which the operator is defined. For a full formulation and discussion of the index theorem on graphene the reader can refer to a recent paper by Park [63].

1.5 Graphene inside: towards carbon-based electronics

The International Technology Roadmap for Semiconductors, responsible to pursue cost-effective advancements in microelectronics, has recently indicated carbon, and in particular graphene, as the most promising candidate to replace silicon and go beyond CMOS (Complementary Metal-Oxide Semiconductor) technology.
A look back to the history of electronics also seems to suggest carbon as the basic material for future devices. The first transistors produced in the 50s, indeed, were made out of germanium; this was soon replaced by silicon, which is more energy efficient and far less expensive; from the chemistry point of view silicon is very similar to Germanium and just lie above it in the Periodic Table, in group IV (group 14 according to current IUPAC regulations). The next and latest element up in the series is carbon. In particular a future upgrade to graphene would represent a further major gain in energy efficiency and raw material cost and would break the $10\,nm$ limit of scalability typical of Si-based systems [66].

A wealth of graphene-based electronics devices has already been built: from transistors [67, 68] to electrochemical sensors [69, 70], from transparent electrodes [71] to LCD [72] and touchscreens [1]. Field effect transistors made from pure (epitaxial or CVD-growth) graphene have been engineered into logic gates [73] and basic memory devices [74], while large scale fabrication methods, suitable for industrial processes, have been suggested [75, 76]. State-of-the-art transistors developed at IBM have reached the operating frequency of 100 GHz [77, 78] and, symbol of these fast progresses towards a real carbon-based microelectronics, the ***graphene inside*** logo, in place of *intel inside*, has already appeared on the web. Nevertheless it's rather difficult to think that devices such as graphene microprocessors will be on the market in the next ten or fifteen years. More readily available applications of graphene are based on its use as a material for transparent electrodes. The scientific community has made strong efforts towards the fabrication of graphene films [31, 79, 33, 32] (see section 3.1) which can be used in device like solar cells [80, 81] and as replacement of the expensive Indium Tin Oxide in LCDs [72]. In particular researchers from Sung Kyun Kwan University, in Korea, have centered a double success, published as the cover story in Nature Nanotechnology [1]: they have managed to growth record graphene sheets as large as $1\,m^2$, with standard chemical vapor deposition on metal substrates and, most importantly, they have developed a simple technology to transfer these graphenes onto plastics surfaces, reaching the fabrication of a flexible, graphene-based touchscreen.

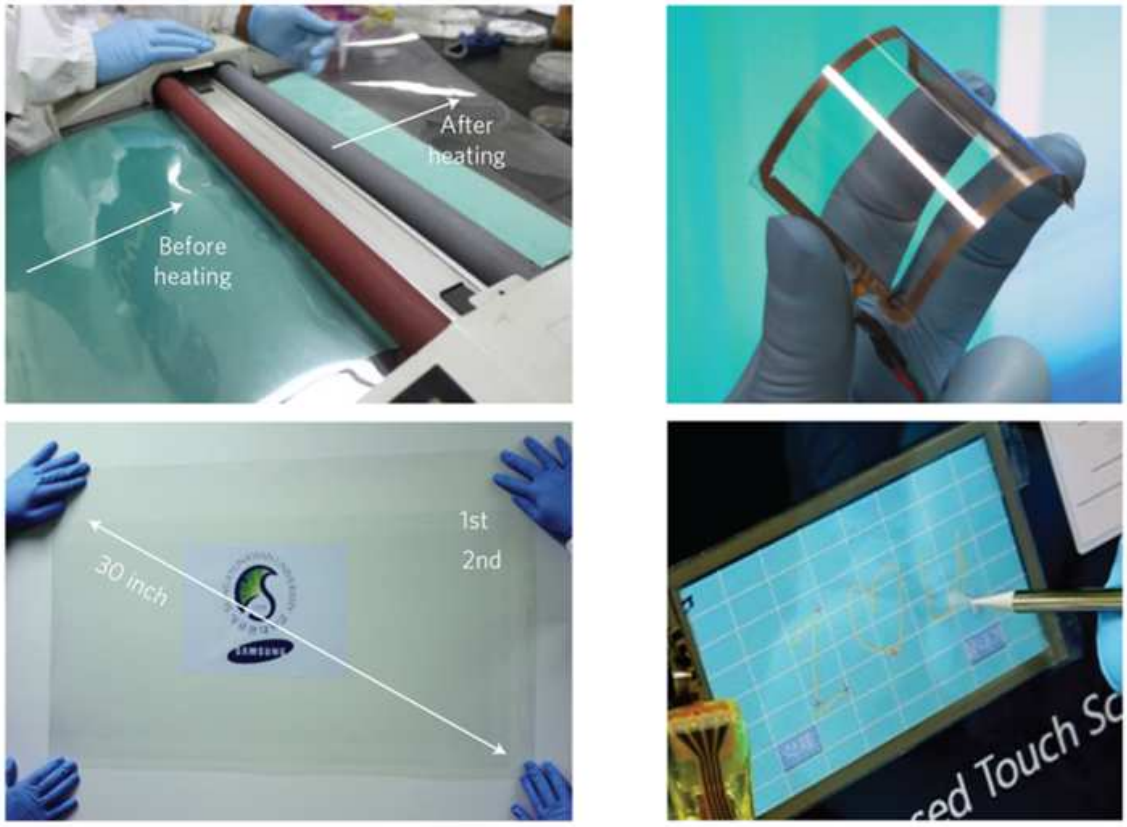

Figure 21. Left: Roll-to-roll transfer process of graphene layers onto plastics substrates and below the largest graphene sheet ever made deposited on PET. **Right**: The graphene-based touchscreen, flexible and transparent (upper panel) is connected to a computer with control software for operation (bottom panel).

1.6 Optics, Photonics and Optoelectronics

The application of graphene as a material for transparent electrodes suggests the importance of its optical properties, which deserve to be briefly discussed here. Experimental measurements in the visible and infrared frequency range [82, 83], displayed in fig.22, have shown that graphene is almost transparent, as each layer invariably absorbs only $\simeq 2.3\%$ of normal incident light, almost independently from wavelength. The observed **universal transmittance** perfectly matches the theoretical expectations for massless fermions in graphene [84] given by

$$\mathcal{T} = \frac{I_{out}}{I_{in}} = \left(1 + \frac{1}{2}\pi\alpha_0\right)^{-2} \qquad \mathcal{R} = \frac{1}{4}\pi^2\alpha_0^2\mathcal{T} \qquad \mathcal{A} \simeq \pi\alpha_0 = 2.293\% \quad (1.9)$$

for transmittance, reflectance and absorbance respectively ($\mathcal{A}$ is approximated to the first order term). Here $\alpha_0 = \frac{e^2}{4\pi\epsilon_0 c\hbar} = \frac{1}{137}$ is the ordinary fine structure constant.
Actually effects related to finite temperature, doping (non-zero chemical potential μ) and intraband scattering (this last one only for the lower energy photons), result in a residual frequency dependence of the optical conductivity [83]. The right panel in figure 22 show that this deviation from the universal behaviour is almost negligible for photon energies above 0.5 eV, i.e. in the near-infrared and visible region.

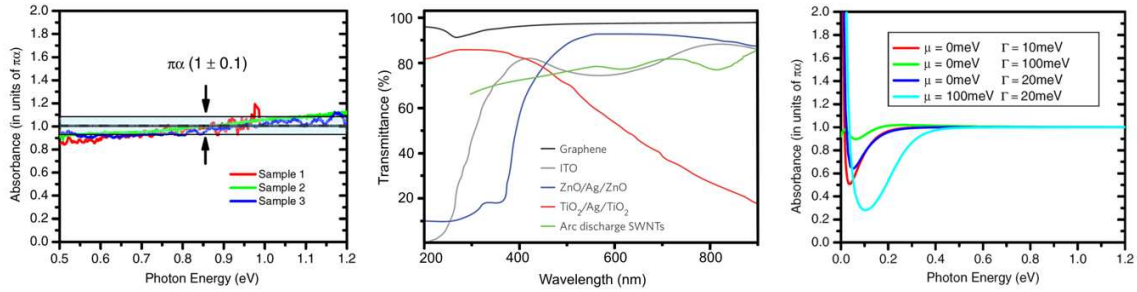

Figure 22. Optical properties of graphene monolayers. **Left**: Absorbance measurements yields an almost constant value $\pi\alpha_0$, in agreement with the theoretically expected behaviour. **Center**: Transmittance (transparency) of graphene, compared to other applicative materials including ITO and single wall CNT. **Right**: Calculated graphene absorption spectra at $T = 300\,K$, showing that deviations from the universal constant behaviour (see text) are relevant only below $0.5\,eV$ (far infrared). Results are shown for different values of the chemical potential μ and scattering rate Γ.

Applications of graphene's optical properties are not limited to exploit its transparency, as discussed above for electrodes, but also its broad absorption range has proved useful [85, 86]:

- in the nonlinear response regime, graphene has been used as a broadband *saturable absorber* in pulsed lasers;

- Graphene films can serve as optical frequency converters and second-harmonic generators, in order to expand the wavelengths accessible to lasers;
- Graphene dispersions can act as *optical limiters*: the absorbed light energy converts into heat, resulting in reduced transmission. Functionalized graphene has shown to outperform C_{60} for these applications.
- graphene-metal junctions and graphene-based transistors can be used as photodetectors over the whole visible range. Optimized devices «were shown to reliably detect optical data streams of 1.55 μm light pulses at a rate of 10 GBits/S» [86].

A comprehensive review about the mentioned and further applications in the field of photonics and optoelectronics can be found in [85].

1.7 Defects in graphene

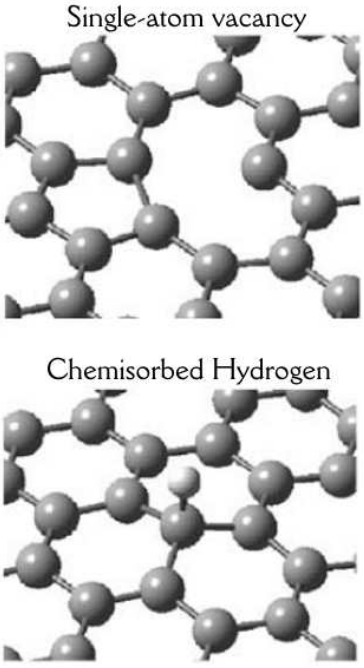

Figure 23. Schematic representation of two common in-plane defects in graphene.

In mesoscopic materials and structures the distribution and type of defects can affect dramatically the electronic and transport properties of the system and are thus relevant for technological applications. On the one hand, as in the realm of semiconductors and microelectronics, clean and pure materials may be required, to minimize the scattering centers and get uniform transport behaviour (as seen before for the conductivity of graphene samples with different purity); on the other hand the control and even the maximization of defects concentration is sometimes important to engineer a specific property of interest inside the material. In the following the different types of defects commonly present in graphene are shortly reviewed.

In-plane defects

Carbon vacancies

The simplest defect on the graphene plane are isolated carbon vacancies. In such cases two of the freed electrons bind each other to form a pentagonal ring, while the third *dangling bond* becomes a paramagnetic center. Such type of defects can then be easily detected as a Curie contribution in SQUID magnetometry.

Adsorbed molecules

In samples derived from wet chemical methods (see chapter 3) a variety of functional groups can be bound to the carbon network, but the most common chemisorbed species is atomic hydrogen. In next section it will be shown that hydrogen impurities generates localized spin states closely analogue to the vacancy case.

Structural modifications

In some cases array of carbon vacancies, fractures and cluster of non-hexagonal rings have been observed in graphene or even engineered for specific purposes like the opening of a band gap. These types of defects are of minor importance within this study and will not be further discussed.

Defects at graphene edges

Different types of defects have been observed along graphene edges, including protruding atoms [87], folding edges [87, 88], pair of pentagonal and heptagonal rings [50] and single atom vacancies [16]. On zigzag edges the latter defect causes the π electron quasi-localized state to break in two separate regions and eventually quench possible hyperfine interactions along the edge, which are allowed by the superexchange across the π state [89]. Edges themselves can be considered as defects with respect to the ideal graphene plane.

In μSR spectroscopy electronic states of edges and defect sites have revealed radically different signals with respect to the standard case of graphite (or of an ideal graphene plane) [90] and their throughout investigation with this technique will be discussed in chapter 4. The distribution of different defects types in graphene is of interest because it is strongly related both to the existence of possible magnetic phases in graphene, as explained in the next section, and to the interaction between hydrogen and the bidimensional carbon lattice, which makes graphene a promising material for hydrogen storage applications [6, 91, 92].

1.8 Magnetic interactions in graphene

Magnetometry investigations in samples produced by different chemical routes[15] show [90] that monolayer and few-layers graphenes are essentially diamagnetic materials. In addition a paramagnetic contribution, originated by electrons at dangling bonds and defects sites, can be easily observed in the temperature dependent magnetization and a slight ferromagnetic signal is detected at 300 K: the latter has proven fully compatible with the few ppm of magnetic impurities present in these samples. These results, obtained within the present study and described in chapter 4, allow to conclude that **no long range magnetic order is present in graphene** down to 2 K, as recently confirmed in a work published by Geim's group [93].

Nevertheless other magnetometry experiments [95, 96, 97] have renewed the interest towards possible carbon-based magnetism in graphene. Figure 24 [16] shows the hysteresis curves registered by Rao and coworkers [94] in samples obtained by exfoliation of graphite oxide (EG), conversion of nanodiamonds (DG) and arc evaporation of graphite in hydrogen atmosphere (HG): the latter sample display the highest ferromagnetic contribution, with a saturation magnetization which should be above possible impurities contaminations. Once again in the history of carbon magnetism, hydrogen and defects [96] appear as the main actors that can be held responsible for the rise of magnetic order.

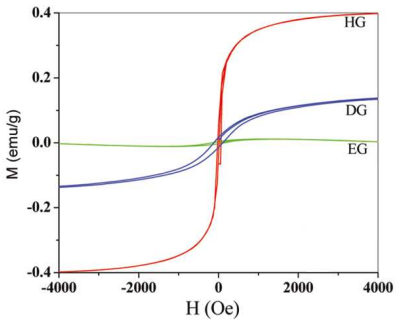

Figure 24. Magnetic hysteresis curves at 300 K, reported in ref.[94] for graphene samples produced by 3 different methods: exfoliation of graphite oxide (EG), conversion of nanodiamonds (DG) and arc evaporation of graphite in hydrogen atmosphere (HG).

Many different theoretical studies [9, 98, 99, 32], based on *ab initio* calculations, also converge to expect the existence of magnetic interactions in graphene,as a result of correlations among electronic states localized at defects. In particular it is worth discussing here the model proposed by prof. Oleg Yazyev and coworkers [10, 100, 101]. His studies and personal collaboration, indeed, served as one of the bases of discussion for the experimental results obtained within the present work.

[15] Synthesis of graphene samples used in this study are detailed in chapter 3.

[16] This figure is not intended to be representative of graphene's magnetic properties, but only to evidence that magnetic order have been observed in some graphene-based systems.

Consider the two types of in-plane defects discussed above, namely chemisorbed hydrogen atoms and carbon vacancies. Their electronic properties are quite similar and can be summarized as follow: each defect generates a quasi-localized electronic density, which is distributed on the sites of the complementary sublattice (odd nearest neighbours) and decay as a function of the distance according to a power law. On these sites a positive spin polarization is found due to the exchange energy brought by the defect states (see fig.25a). The resulting exchange field polarizes the remaining electronic orbitals, originating a negative spin polarization on the even nearest neighbours and a further positive contribution on the odd nearest neighbours. The spin density map for the two types of defects is represented in fig. 25a and its decay as a function of the distance is plotted in fig. 25b. Here the solid line describes the behaviour for the chemisorbed hydrogen defect, while the dashed line correspond to the carbon vacancy: the spin polarization in this case is not defined at the defect sites (index 0) where the atom is missing, and is out of scale (0.39) on site 1, due to the contribution of the paramagnetic electron of the dangling bond. This is the main difference among the two cases.

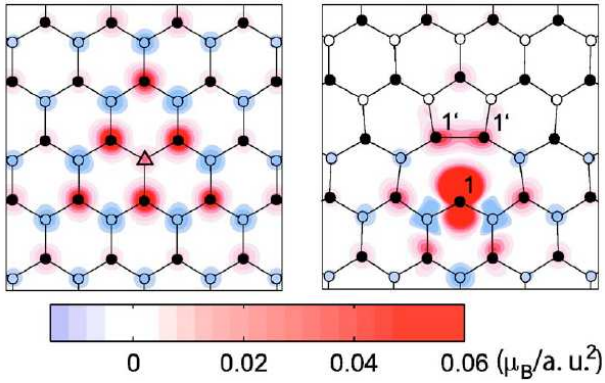

(a). Electron spin density maps around a hydrogen chemisorption defect and a carbon vacancy. Black atoms denote the odd nearest neighbours and white atoms denote the even nearest neighbours.

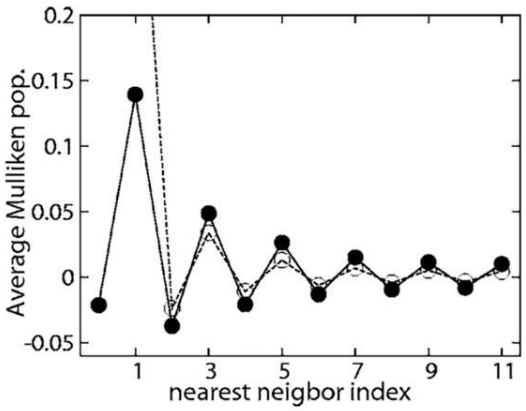

(b). Spin populations as a function of the distance from the defect site, averaged over the i-th nearest neighbours, for hydrogen chemisorption defects (black circles) and vacancies (white circles).

Figure 25. Spin polarization density around point defects on the graphene plane. Adapted from [10].

The polarized electronic states located at defects can interact among themselves if the defects concentrations is high enough (that is if the defects are close enough so that their spin densities, represented by fig. 25b, can spatially superimpose). These magnetic interactions among localized states can be described in terms of the Stoner model for itinerant magnetism [102, 10] and two different situations are expected on

graphene (fig.26):

- defects located on the same sublattice should give rise to *ferromagnetic* correlations;
- on the contrary, defects located on different sublattices has an *antiferromagnetic* ground state.

In the bulk material as a whole, in the hypothesis that the defects are randomly distributed on the honeycomb lattice, an antiferromagnetic order should then be favoured.

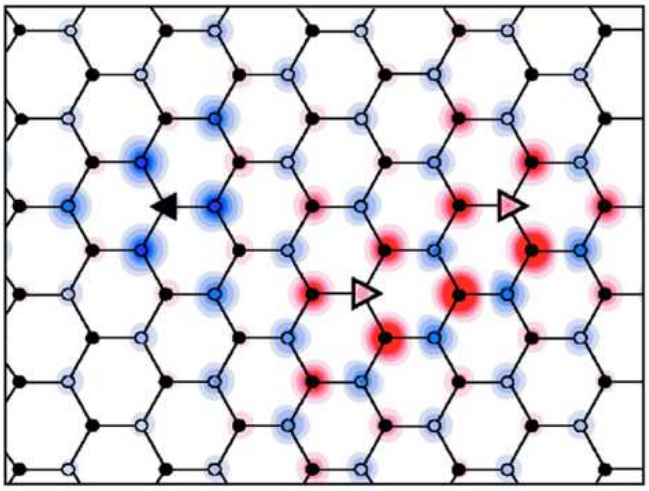

Figure 26. Magnetic interactions among defect states: spin density distribution in a system with three hydrogen chemisorption defects, two in one sublattice and one in the other. The same colour scale of the previous figure apply. Adapted from [10].

Chapter 2

Solid state spectroscopies applied to Low-Dimensional and Nanostructured materials

One of the most intriguing challenges in today materials physics is to exploit spectroscopies and experimental techniques traditionally devoted to bulk solid state materials for low-dimensional and nanoscopic systems. To face this challenge many efforts are spent by the research community especially in two directions:

The development of the technique in both its experimental and theoretical aspects. This includes on the one hand the optimization of experimental procedures and instruments performance for 1DIM and 2DIM materials; this is, for example, intensively pursued on large scale facilities, even with the construction of dedicated beamlines. On the other hand, there is the need to elaborate new theoretical models and adapt existing ones to properly described the significant interactions in the system under study, taking into account low-dimensionality and finite-size effects.

The fulfilment of experimental requirements by these systems, in spite of their nanoscopic structure. In particular the development of synthetical methods for the production of gram-scale amounts of samples is needed for techniques like neutron scattering and μSR, which employ particles with a relatively large penetration depth.

Next chapter will take care of the latter issue, describing the synthesis procedures used to obtain graphene samples, while in the following sections the different experimental techniques applied for their characterization are discussed.

In particular Muon spin rotation and relaxation (μSR), Nuclear magnetic resonance (NMR), Inelastic neutron scattering (INS) and SQUID magnetometry are shortly reviewed: for each technique an introduction, an explanation of the basic mechanisms and an overview of the possibly probed interactions are given. These are not intended to be comprehensive descriptions, but only to provide fundamental insights into the interactions encountered in graphene and discussed in the experimental section.

2.1 Nuclear Magnetic Resonance

NMR spectroscopy studies the magnetic response of atomic nuclei, in order to gain valuable information on them and on their environment.
Since its development at the end of World War II, the NMR technique has been rapidly spreading in the scientific community and it has become one of the most exploited spectroscopies in analytical organic chemistry, as well as a powerful tool for the investigation of the physical properties of materials. Another commonly known application of this technology is the Magnetic Resonance Imaging (MRI), routinely used in hospitals to obtain direct images of soft tissues in the human body.

The employment of a *resonance* technique is necessary to reach enough selectivity, as it's often the case in the observation of very weak phenomena, like nuclear magnetism, which would be otherwise hidden by electronic interactions. In NMR nuclear spin energy levels are splitted by the application of a strong static magnetic field and the system is then excited with an electromagnetic radiation whose frequency exactly matches the energy difference between these levels. Typical frequencies, proportional to the applied field through the gyromagnetic ratio $\omega = \gamma H_0$, are within the radiowave spectral region ($10 \cdots 800 MHz$). The transitions induced by this resonant radiation cause the energy levels population to vary, that is generate a net magnetization not aligned with the external field. At the end of the excitation, the relaxation of magnetization as a function of time is measured: indeed, valuable information on structure, chemical composition, electronic configuration and other properties can be obtained by studying how the system lose its energy to the environment.
In the following the basic principles of NMR spectroscopy are discussed and it is shown that, despite nuclear spin is namely a quantum observable, it is possible to describe an NMR experiment even in a semi-classical picture. Within this frame the phenomenological Bloch equations are also introduced. The fundamental nuclear interactions are then considered, but only the electric quadrupole effects, important for the present study, are thoroughly analyzed.

2.1.1 NMR Nuclei

It's first important to specify which nuclei can be (more or less easily) studied by NMR. To interact with external magnetic fields the considered nucleus must have a non-zero spin $I \neq 0$, condition satisfied by almost all chemical elements (except Argon, which result NMR silent), but only for specific isotopes. Using the composition of angular momenta, one easily discover that the nuclei with zero spin are the ones with an even number of both protons and neutrons (e.g. ^{12}C and ^{16}O).
A further limit is that each isotope is characterized by a NMR *sensitivity*, defined as the signal intensity with respect to a reference nucleus (usually ^{1}H). The product of sensitivity and isotopic abundance is named NMR *receptivity* and provide an estimation of the actual possibility to observe a NMR signal: a too low receptivity, as it happens for ^{43}Ca ($R^H \simeq 8 \cdot 10^{-6}$), indicates that the signal is completely hidden by electronic noise and it's not detectable within a reasonable time. Isotopic substitutions are sometimes used to enhance the receptivity.
Easily observed nuclei include ^{1}H, ^{7}Li and ^{19}F, while ^{13}C is an example of nucleus with a rather low receptivity and can be studied only waiting for a large number of acquisitions. Nevertheless carbon NMR is widely applied in chemistry and materials science. The following table lists the NMR properties for some relevant nuclei.

2.1.2 Basic theory and mechanism of NMR spectroscopy

In a nuclear magnetic resonance experiment the sample is subjected to a static magnetic field, of high intensity[1] and good homogeneity. In these conditions the behaviour of a nucleus of magnetic moment $\vec{\mu}$ and angular momentum $\vec{I}$ is described by the Zeeman Hamiltonian

$$\mathcal{H} = -\vec{\mu} \cdot \vec{H}_0 = -\gamma \vec{I} \cdot \vec{H}_0 \,. \tag{2.1}$$

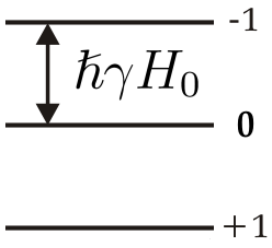

Figure 27. Zeeman energy levels for a nucleus with spin $I = 1$.

In a reference frame whose z axis is directed along the external field, as usual in quantum mechanics, this is written as $\mathcal{H} = -\gamma J_z H_0$ and by solving the steady-states Schroedinger equation one obtain the Zeeman nuclear energy levels

$$E_m = -\gamma \hbar H_0 m \qquad m = -\mathrm{I}, \ldots, +\mathrm{I}$$

that can be experimentally observed by inducing transitions among the corresponding spin eigenstates.

[1] Typical field values obtained from laboratory superconducting magnets range form 6 to 10 T.

Isotope	Spin I	γ (MHz/T)	Nat.Abundance	R^H	$\mu(\mu_N)$	$Q(fm^2)$
^{1}H	1/2	42.576	99.985%	1.00	4.837	–
^{2}H	1	6.536	0.015%	$1.45 \cdot 10^{-6}$	1.213	0.286
^{7}Li	3/2	16.5478	92.58%	0.27	4.204	−4.01
^{10}B	3	4.575	19.9%	0.0198	1.801	8.46
^{11}B	3/2	13.663	80.1%	0.165	2.689	4.06
^{13}C	1/2	10.708	1.10%	0.0159	0.702	–
^{14}N	1	3.078	99.63%	$1.01 \cdot 10^{-3}$	0.404	2.02
^{17}O	5/2	5.774	0.038%	0.029	−1.894	−2.558
^{19}F	1/2	40.0765	100%	0.834	2.62	–
^{23}Na	3/2	11.2686	100%	0.093	2.217	10.89
^{25}Mg	5/2	2.6083	10.00%	$2.68 \cdot 10^{-4}$	−1.012	19.94
^{27}Al	5/2	11.103	100%	0.207	3.64	14.03
^{31}P	1/2	17.25	100%	0.0665	1.13	–
^{35}Cl	3/2	4.176	75.77%	$4.72 \cdot 10^{-3}$	0.92	−8.165
^{39}K	3/2	1.989	93.26%	$5.1 \cdot 10^{-4}$	0.39	6.01
^{41}K	3/2	1.092	6.73%	$8 \cdot 10^{-5}$	0.215	7.33
^{59}Co	7/2	10.08	100%	0.278	4.63	42
^{63}Cu	3/2	11.3187	69.17%	0.065	2.875	−22
^{65}Cu	3/2	12.1027	30.83%	0.0354	3.0746	−20.4
^{75}As	3/2	7.315	100%	0.025	1.44	31.4
^{85}Rb	5/21	4.125	72.165%	0.11	1.35	27.4
^{115}In	9/2	9.385	95.7%	0.353	5.54	81
^{151}Eu	5/2	10.58	47.8%	0.18	3.47	90.3
^{153}Eu	5/2	4.674	52.2%	0.015	1.53	241

Table 1. The most important NMR parameters for some nuclei: the spin angular momentum I, the gyromagnetic ratio γ, the natural isotopic abundance, the NMR receptivity relative to hydrogen, the nuclear magnetic moment in units of nuclear magneton (in SI units $\mu_N = \frac{e\hbar}{2m_p} = 0.505 \cdot 10^{-26}\, Am^2$), the electric quadrupole moment Q (in fm^2 or $10^{-2} barn$).

The simplest possible excitation is an alternate magnetic field $\vec{H}_1$, linearly polarized on the (xy) plane

$$\mathcal{H}_{pert} = -\gamma H_1 \cos wt I_x$$

whose frequency should exactly match the energy differences among nuclear levels

$$\omega = \omega_0 = \gamma H_0.$$

This is why we talk about a *resonance* technique.

In a NMR experiment magnetization, rather than energy, is measured and it's then useful to evaluate this observable. The expectation value of the magnetic moment $\vec{\mu}$ for a singular nuclear spin can be computed with the methods of quantum mechanics, but as it will soon be evident, one can limit to the calculation of its time derivative $\frac{d\vec{\mu}}{dt}$ in a generic magnetic field $\vec{H}$. In particular, since $\vec{\mu} = \gamma\vec{I}$, it's convenient to evaluate first the derivative of the angular momentum

$$\begin{aligned}
\tfrac{d\vec{I}_k}{dt} &= \tfrac{i}{\hbar}\left[\widehat{\mathcal{H}}, \widehat{I}\right] \\
\tfrac{d\vec{I}_x}{dt} &= -\tfrac{i}{\hbar}\left[\gamma H I_z, I_x\right] = -\tfrac{i}{\hbar}\gamma H i\hbar I_y = \gamma H I_y \\
\tfrac{d\vec{I}_x}{dt} &= -\gamma H I_x \\
\tfrac{d\vec{I}_x}{dt} &= 0\,.
\end{aligned}$$

These relations are summarized by the vector equation $\frac{d\vec{I}}{dt} = \vec{I} \times \gamma\vec{H}$ and in turn for the magnetic moment we obtain

$$\frac{d\vec{\mu}}{dt} = \vec{\mu} \times \gamma\vec{H}\,. \tag{2.2}$$

This last expression matches the second cardinal equation of classical dynamics and it's then possible to conclude that the response of nuclear magnetic moments to any external field (no restrictions on $\vec{H}$ have been considered) follow the classical equations of motion. *Therefore a semi-classical picture is fully adequate to properly describe the basics phenomena of a NMR experiment.*

In case only the static magnetic field $\vec{H}_0$ is considered, eq.(2.2) represents the well-known *Larmor precession* (fig.28a), with the nuclear magnetic moment precessing around the external field at the frequency $\vec{\omega}_L = -\gamma_0\hat{k}$. If both $\vec{H}_0$ $\vec{H}_1$ are present, instead, according to (2.2) the nuclear spin follow a nutation motion (fig.28b), resulting from the composition of Larmor precession and of a further rotation around $\vec{H}_1$.

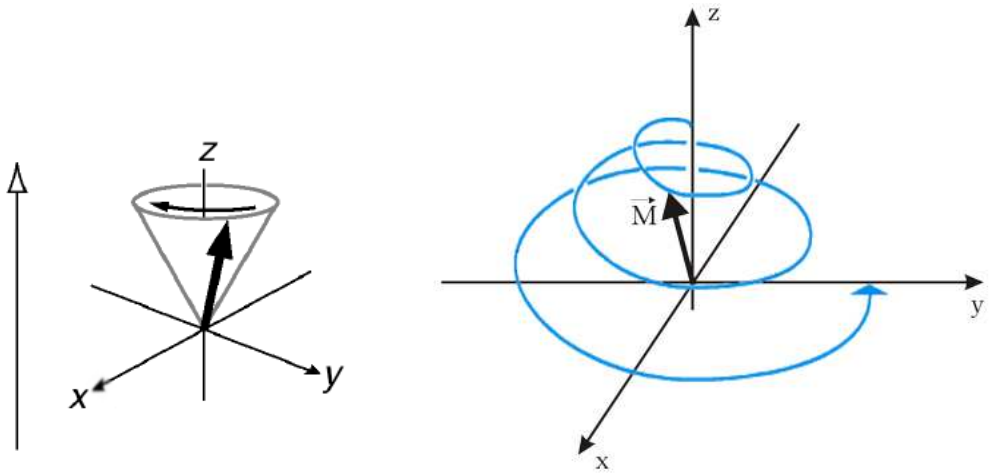

(a). Larmor precession of a magnetic moment around the external field. The spin precess clockwise for $\gamma > 0$ and counterclockwise for $\gamma < 0$.

(b). Nutation motion of the magnetization vector under the contemporary action of a static field $\vec{H}_0$ directed along z and a rotating field $\vec{H}_1$, polarized in the (xy) plane.

Figure 28. Motions of a magnetic moment in the presence of external fields.

Therefore starting from the thermal equilibrium, where the total nuclear magnetization $\vec{M}$ is directed along the z axis ($\vec{H}_0$), if a field pulse $\vec{H}_1$ is applied for a time t, it is possible to rotate the magnetization by an arbitrary angle θ, according to

$$\begin{aligned} \theta &= \gamma H_1 t \\ M_z &= M_0 \cos(\gamma H_1 t) \\ M_\perp &= M_0 \sin(\gamma H_1 t) . \end{aligned}$$

When the pulse is complete, the magnetization will continue to precess around the static field and, if $\theta = 90°$ has been chosen, it will be possible to detect it on the (xy) plane, by means of a proper induction coil. The registered signal is commonly known as FID (Free Induction Decay), because it's the electric signal induced in absence of $\vec{H}_1$ (i.e. free from external perturbations), which spontaneously decay according to an exponential relaxation function. This signal is made up of the contributions of all the nuclei and its decay is the result of the energy exchange among spins (*spin-spin relaxation*), which rapidly lose their coherence, and with the crystal lattice (*spin-lattice relaxation*), that allow to restore thermal equilibrium.

The procedure we have just shortly described is the basic idea underlying Fourier Transform NMR spectroscopy. Nowadays this is the most commonly used form of NMR and takes this name as usually information are extracted not from the signal in

time domain, but from its frequency spectrum[2].
In order to model the characteristics of the NMR signal the relaxation processes must be properly taken into account and eq.(2.2) must be modified accordingly. This yield the phenomenogical equations proposed by Bloch in 1946, where the magnetization is expected to decay exponentially towards M_0 along z and towards 0 in the perpendicular plane:

$$\begin{cases} \frac{dM_x}{dt} &= \gamma \left(\vec{M} \times \vec{H}\right)_x - \frac{M_x}{T_2} \\ \frac{dM_y}{dt} &= \gamma \left(\vec{M} \times \vec{H}\right)_y - \frac{M_y}{T_2} \\ \frac{dM_z}{dt} &= \gamma \left(\vec{M} \times \vec{H}\right)_z + \frac{M_0 - M_z}{T_1} \end{cases} \qquad \text{Bloch's Equations} \tag{2.3}$$

In NMR T_1 and T_2 are commonly known as *longitudinal* and *transverse* relaxation times respectively, as they are the characteristic time constants of the exponential functions obtained by integrating eqs.(2.3)

$$\begin{aligned} M_x &= M_{x0}\, e^{-\frac{t}{T_2}} \\ M_y &= M_{y0}\, e^{-\frac{t}{T_2}} \\ M_z &= M_0 \left(1 + e^{-\frac{t}{T_1}}\right). \end{aligned}$$

Please notice that if on the one hand the phenomenological introduction of Bloch's equations may not be "convincing", on the other it's possible to derive eqs.(2.3) in the framework of Redfield theory, by applying the standard methods of statistical quantum mechanics [103].

2.1.3 Nuclear interactions

The Spin Hamiltonian hypothesis. The following description of nuclear interactions is based on the adiabatic approximation, i.e. the assumption that electronic and nuclear dynamics have different timescales (typically of the order of femtoseconds and picoseconds respectively) and that their wavefunctions are therefore *separable*. The nuclear spin Hamiltonian can then be expressed as a function of nuclear coordinates, while the electronic motions are so fast that there's no need to include the details of the related electromagnetic fields, but only effective potentials which can model their interaction with nuclei.

[2] As the Fourier transform of an exponentially decaying sinusoidal function, the spectrum is usually a Lorentzian peak centered at the resonance frequency ω_L. More generally it will be a set of peaks, one for each different effective field probed by the different nuclei

The total spin hamiltonian can be written as[3]

$$\mathcal{H} = \mathcal{H}_{magn} + \mathcal{H}_{elet} = \mathcal{H}_{ext} + \mathcal{H}_{dip} + \mathcal{H}_{CS} + \mathcal{H}_{Knight} + \mathcal{H}_{J} + \mathcal{H}_{Q} \tag{2.4}$$

and it is made up of two contributions:

1. An ELECTRIC PART which describes the interactions of the nuclear electric charge distribution with the surrounding electric forces. We will deal with this part in detail and we will notice that its most important term is the quadrupolar interaction.

2. A MAGNETIC PART which entail all the interactions listed in table 2.

As the magnetic interactions are not relevant within this work, we will not discuss the latter part and the reader may refer to the excellent textbooks of Levitt [104] and Slichter [103].

Map of Magnetic Nuclear Interactions

EXTERNAL	Nuclear Zeeman Energy due to H_0		
	Transitions among nuclear spin states due to H_1		
INTERNAL	MAGNETIC COUPLINGS OF NUCLEAR SPINS	with the electrons orbital motion generated by H_0	- CHEMICAL SHIFT
		Dipolar interactions with other nuclear spins	- DIPOLAR BROADENING
		Hyperfine Interactions with electronic spins: dipole-like for ***p*** and ***d*** states and via the Fermi contact potential for ***s*** states ↳ 1st perturbative order – KNIGHT SHIFT ↳ 2nd perturbative order – J-COUPLING	

Table 2. Map of the magnetic nuclear interactions of interest in a NMR experiment.

[3]Some minor contributions, like spin rotation, are neglected here.

Electric Spin Hamiltonian

To discuss the electric interactions between the nucleus and its environment, it's useful to write the *nuclear charge distribution* as a multipole expansion

$$\mathbb{Q}(\vec{r}) = \mathbb{Q}^{(0)}(\vec{r}) + \mathbb{Q}^{(1)}(\vec{r}) + \mathbb{Q}^{(2)}(\vec{r}) + \mathbb{Q}^{(3)}(\vec{r}) + \dots \tag{2.5}$$

In (2.5) the terms $\mathbb{Q}^{(n)}(\vec{r})$ are proportional to the corresponding spherical harmonic functions and each represent respectively a spherical, dipolar, quadrupolar charge distribution and so on. The modulus of the zero-order term $\mathbb{Q}^{(0)}(\vec{r})$ is the total nuclear electric charge, while the subsequent terms are referred to as nuclear *dipolar* moment, *quadrupolar* moment, etc.
We can correspondingly expand also the electric potential to a Taylor series

$$V(\vec{r}) = V^{(0)}(\vec{r}) + V^{(1)}(\vec{r})\, r + V^{(2)}(\vec{r})\, r^2 + V^{(3)}(\vec{r})\, r^3 + \dots \tag{2.6}$$

Here $V^{(0)}$ is the electric potential from the center of the nucleus, $V^{(1)}$ the gradient of the potential, that is the electric field, $V^{(2)}$ the gradient of the electric field.

Two observations on the nuclear charge distribution are of fundamental importance:

1. For any nucleus the dipolar electric moment is identically zero (within experimental error) as a consequence of the parity of the nuclear wavefunction. Therefore all the odd order terms $\mathbb{Q}^{(2m+1)}$ vanish.

2. As can be inferred from the Wigner-Eckart theorem, the $\mathbb{Q}^{(n)}$ series is truncated at $2I$, where I is the nuclear spin quantum number.

For **spin** $1/2$ **nuclei** the multipole expansion is therefore limited to the zero-order term and the electric energy does not depend on the structure or orientation of the nucleus, which act as a point charge.

For all other **nuclei with spin** $I > 1/2$ the charge distribution has a non spherical symmetry and critically depend on the orientation. The most important energy contribution is the interaction of the nuclear quadrupole moment $\mathbb{Q}^{(2)}$ with the electric field gradient $V^{(2)}$, while higher order terms can be neglected. When present, the quadrupolar interaction is quite intense, with frequencies ranging from several kHz up to tenths of MHz and can be even comparable to Zeeman energy. In the following the effects of the quadrupolar interaction in NMR are thoroughly discussed, as they will be of particular interest for the analysis of experimental results.

The quadrupolar interaction

The interaction of the nuclear quadrupole moment with the surrounding environment depends on on the *electric field gradient*. This is a second order tensor, whose elements V_{ij} are the second derivatives of the potential $\frac{\partial^2 V}{\partial x_i \partial x_j}$. In other words it is defined as the Hessian matrix of V. We notice that, according to Laplace equation $\nabla^2 V = 0$ this tensor has a vanishing trace.

In the reference frame where V_{ij} assumes a diagonal form

$$\begin{pmatrix} V_{XX} & 0 & 0 \\ 0 & V_{YY} & 0 \\ 0 & 0 & V_{ZZ} \end{pmatrix} \text{ (where we assume } |V_{XX}| \leqslant |V_{YY}| \leqslant |V_{ZZ}|)$$

the quadrupolar hamiltonian can be written as

$$\mathcal{H}_Q = \frac{eQ}{4\mathrm{I}(2\mathrm{I}-1)} \left[V_{ZZ}(3\widehat{I}_z^2 - \widehat{I}^2) + (V_{XX} - V_{YY})(\widehat{I}_x^2 - \widehat{I}_y^2) \right]. \tag{2.7}$$

where Q is the intensity of the nuclear quadrupole moment (constant depending on the considered chemical element), I is the nuclear spin quantum number and $\widehat{I}^2, \widehat{I}_x^2, \widehat{I}_y^2, \widehat{I}_z^2$ are the spin angular momentum operators [4].

One can notice from eq.(2.7) that to describe the quadrupolar interaction only the parameters V_{ZZ} and $(V_{XX} - V_{YY})$ are needed.

It's customary to define also the *asymmetry coefficient*[5]

$$\eta = \frac{V_{XX} - V_{YY}}{V_{ZZ}} \quad , \; 0 \leqslant \eta \leqslant 1 \tag{2.8}$$

so that eq.(2.7) becomes

$$\mathcal{H}_Q = \frac{eQ}{4\mathrm{I}(2\mathrm{I}-1)} V_{ZZ} \left[3\widehat{I}_z^2 - \widehat{I}^2 + \eta(\widehat{I}_x^2 - \widehat{I}_y^2) \right]. \tag{2.9}$$

To switch from the coordinate system defined by the principal axes of the quadrupolar interaction to the laboratory reference frame, it is necessary to introduce in the Hamiltonian a term dependent on the Euler angles α, β, γ that defines the transformation

$$\mathcal{H}_Q = \frac{eQV_{ZZ}}{4\mathrm{I}(2\mathrm{I}-1)} \left[3\widehat{I}_z^2 - I(I+1) \right] \left(\frac{3\cos^2\beta - 1}{2} + \frac{\eta}{2}\sin^2\beta\cos 2\alpha \right). \tag{2.10}$$

[4] This Hamiltonian is restricted to 1^{st} order term (in the quadrupolar frequency ω_Q), but 2^{nd} order terms are also often important. However, as it is not the case for the deuterium nucleus investigated here, these 2^{nd} order contributions will not be considered.

[5] In the literature it's not uncommon to define also the electric field gradient in elementary charge units $q = \frac{V_{ZZ}}{e}$ and the quadrupolar coupling constant $C_{QCC} = \frac{e^2 qQ}{h}$.

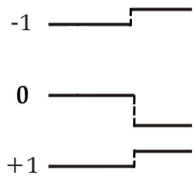

Figure 29. Effect of the quadrupolar interaction on the energy levels of a nucleus with spin 1.

In order to show the effects of the quadrupolar interaction in solid state NMR we consider the case of a spin 1, in the hypothesis of $\eta = 0$ (we will discuss the role of asymmetry later on). Considering the Hamiltonian (2.10) as a perturbation to Zeeman energy levels, it's easy to see that they become

$$\mathcal{E}_m = -\gamma\hbar H_0 m + \frac{eQV_{ZZ}}{4\mathrm{I}(2\mathrm{I}-1)}\left(\frac{3\cos^2\beta - 1}{2}\right)\left[3m^2 - \mathrm{I}(\mathrm{I}+1)\right] \quad (2.11)$$

As displayed in figure 29, the quadrupolar coupling does not change the center of the energy levels, as is expected for an operator with vanishing trace. The energy perturbations are identical for the two $\pm m$ levels, so that both transitions, $(-1 \to 0)$ and $(0 \to +1)$, results translated in frequency with equal and opposite changes. The resonance for $\omega = \omega_L$ is therefore splitted into a doublet.

More generally, for any I, symmetrical side peaks are generated and they are the fingerprint of quadrupolar interactions in NMR. In a natural way, their distance is called *quadrupolar frequency*, but unfortunately there is no general consensus on the definition of this quantity in the literature. We will adopt the most common convention, fixed by Freude [105, 106]

$$\omega_Q = \frac{3eQV_{ZZ}}{2\mathrm{I}(2\mathrm{I}-1)\hbar}. \quad (2.12)$$

Figure (30) shows the quadrupolar powder spectra for different spin values and help to clarify the relation among the definition (2.12) of ω_Q e and the spectroscopic line shape. Notice that for half-integer spins corresponding peaks are separated by ω_Q, while for integer spins the peak-to-peak distance is $\frac{\omega_Q}{2}$.

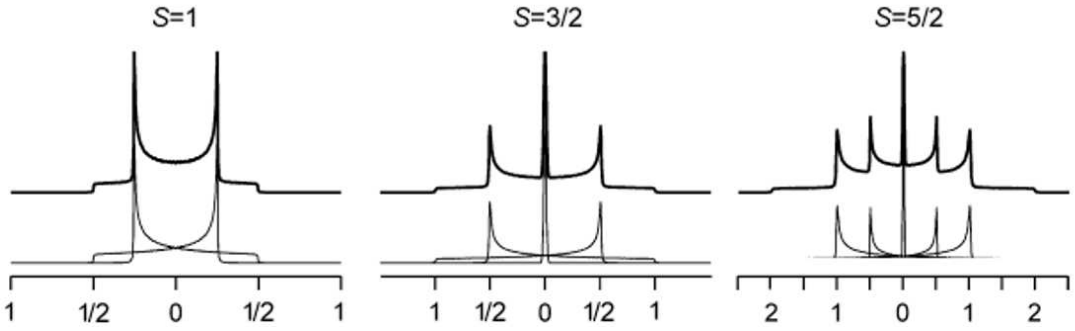

Figure 30. NMR powder line shapes in presence of first order quadrupolar interaction, for integer and half-integer spins. For clarity a slight Gaussian broadening has been added to the theoretical lineshape. Adapted from [107].

To avoid this inconsistency it is generally preferred to adopt a separate definition for integer spin

$$\omega_Q = \frac{3eQV_{ZZ}}{4\mathrm{I}(2\mathrm{I}-1)\hbar}\,, \qquad I = 1, 2, \ldots \quad . \tag{2.13}$$

Within this work NMR investigations have been extended only to spin 1 nuclei and therefore this last definition of ω_Q is adopted from here onward.

Asymmetry of the quadrupolar interaction

It is now appropriate to go beyond the initial assumption $\eta = 0$: with the help of fig.31 we shall shortly study the effect of the asymmetry parameter on NMR powder line shapes[6].

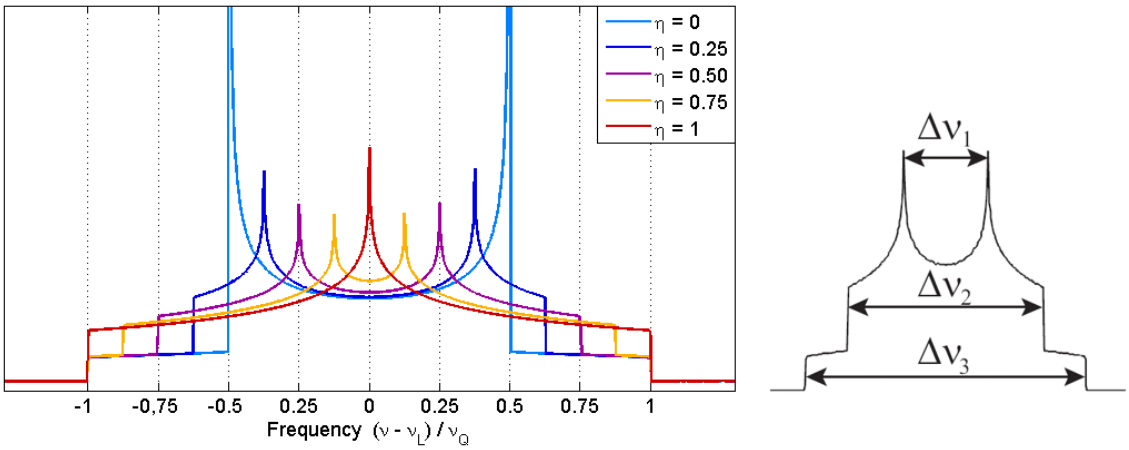

Figure 31. Left: Evolution of NMR powder spectra as a function of η, for a spin 1 nucleus. For clarity a slight Gaussian broadening has been added to the theoretical lineshape. Right: NMR powder spectrum for $I = 1$, $\eta = 0.4$. The different widths $\Delta\nu_i$ are defined in the text.

For increasing η the two peaks gradually shift towards the centre of the spectrum, according to the expression $\Delta\nu_1 = \nu_Q\,(1-\eta)$
until they collapse into a single peak for $\eta = 1$. Meanwhile the peaks intensity drop and the corresponding spectral density is found at higher frequencies (in modulus), so that pronounced shoulders outside the peaks become visible. Their distance increase with increasing η as $\Delta\nu_2 = \nu_Q\,(1+\eta)$, while the broadest part of the quadrupolar spectrum keeps the fixed width $\Delta\nu_3 = 2\,\nu_Q$.

[6]The following observations are made for a spin 1.

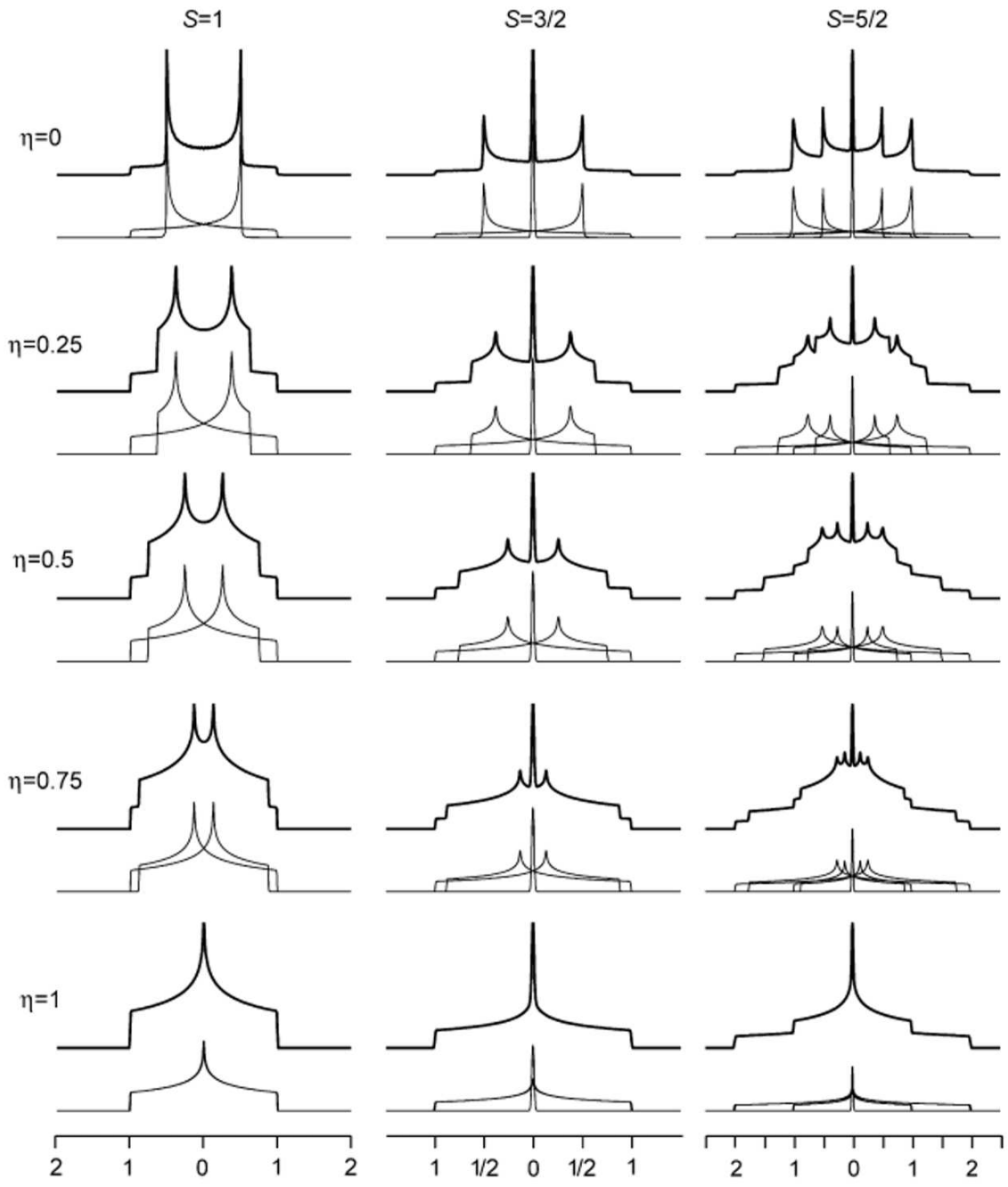

Figure 32. NMR powder line shapes in presence of first order quadrupolar interaction, for different values of the spin quantum number and of the asymmetry parameter η. Here the different definitions for integer nd half-integer spins are used. For clarity a slight Gaussian broadening has been added to the theoretical lineshape. Adapted from [107].

2.2 μSR spectroscopy

Muons are spin 1/2 particles, easily produced in fully polarized beams, which can be implanted into matter to study its magnetic and electronic properties. The related experimental technique is named μSR spectroscopy, where the acronym assumes different meanings: Muon Spin Rotation, Relaxation or Resonance, depending on the type of experiment performed.

The Muon	
Classification in SM	Lepton
Mass	$105.6585\ MeV/c^2$ $\simeq 207\, m_e \simeq \frac{1}{9}\, m_p$
Charge	$\pm e$
Spin	1/2
Mean Lifetime	$2.197 \mu s$
Gyromagnetic Ratio	$\gamma_\mu = 8.5161 \cdot 10^8\ rad/T$ $\gamma_\mu/2\pi = 13.554\ kHz/G$

Table 3. Main Muon properties.

Conceptually analogue to NMR and EPR, it provides information on the distribution of internal magnetic fields in matter and therefore its original and most common areas of application are superconductivity and magnetism [108, 109, 110, 111]. With respect to the latter μSR has important advantages over other techniques:

- because of their high magnetic moment, about $4.5 \cdot 10^{-26}\, J/T$, the muons are sensitive to extremely weak internal magnetic fields, down to $10^{-5}\, T$;
- opposite to magnetometry, which measure the bulk magnetic response of the sample, μSR probes the LOCAL hyperfine interactions present at the muon site. For example muons can give a direct measurement of the internal field of an antiferromagnet.
- In principle the muons implantation takes place randomly in the sample and the signal amplitude in the spectrum turns out to be proportional to the volume fraction. On the one hand μSR is thus insensitive to magnetic impurities. On the other, it is very useful in the study of multiphasic or partially ordered samples.

These characteristics of μSR make it suitable also for the exploration of magnetic phases in carbon-based materials [112], where the possible magnetic interactions are expected to be weak and extended to limited regions [98].

Nevertheless μSR is also widely applied in the field of chemistry: as we will discuss later, the muon can bind to an electron to form Muonium, *a light hydrogen isotope* [113], which has been exploited for many different studies, from electronic radicals (especially in organic compounds) [114, 115] to endohedral fullerenes [116, 112].

Muons were first observed in 1933 by Kunze [117] in the tracks of a Wilson chamber exposed to cosmic rays, where he noticed a new ionizing particle having electric charge $\pm e$ and a lifetime of $\simeq 2.2\,\mu s$. Because the existence of this particle was really unexpected[7], further experiments by Anderson and Neddermeyer [118] at Caltech in 1936 and by Street and Stevenson [119] in 1937 were needed to confirm the muon discovery. In a later experiment it turned out that muons may reach the earth surface only thanks to the relativistic time delation, providing the first experimental proof of the special relativity predictions. The μSR technique was conceived 20 years later, by Garwin and coworkers [120] in 1957 and was developed during the 60s and 70s[8].

Muons are available for condensed matter studies only at a few large accelerator facilities: in Europe there are ISIS, at the Rutherford Appleton Laboratory in the UK, and SμS, at the Paul Scherrer Institute in Switzerland[9]. The latter is a continuous muon source, where muons are "observed one by one", while the former is a pulsed source, where a bunch of many muons is implanted into the sample all at a time. All the μSR experimental studies for this work were carried out at the EMU and MuSR spectrometers at ISIS.

2.2.1 The Muon fate in a μSR experiment

Muons are the products of the β decay of heavier particles, pions, which are in turn obtained from the "bombardment" of a graphite target with an accelerated proton beam. The weak interaction lead the pion to decay with a mean lifetime of $26\,ns$ into a muon and a neutrino, following the scheme

$$\pi^- \longrightarrow \mu^- + \bar{\nu}_\mu \qquad \pi^+ \longrightarrow \mu^+ + \nu_\mu \,. \tag{2.14}$$

A parity violation takes place and hence the emerging muons all have a negative helicity $\mathbf{h} = -1$, that is their spins are 100% polarized against the direction of motion[10].

[7] An expression has become famous and is often reported to stress the surprise for muon discovery at the time: when Nobel laureate I.Rabi was told about the muon he exclaimed ≪Who ordered that?≫.

[8] Further detail on the history of muons and μSR can be found here [121].

[9] Other Muons laboratories are TRIUMF, near Vancouver, in North America and KEK in Japan

[10] Helicity, indeed, is defined as the scalar product of the particle's momentum and spin $\mathbf{h} = \vec{p} \cdot \vec{I}$.

This is also one of the major advantages of μSR over NMR: no magnetic fields are needed to polarize the spins and therefore many experiments can be performed in zero external field (ZF). The polarization is maintained as the beam is transported to the muon spectrometers, while positive muons only are selected for experiments, since the negative ones may undergo a nuclear capture, which yields not negligible effects in case of nuclei with high atomic number.

Polarized muons are implanted in the sample, where they rapidly lose energy and in about 1 ns come at rest in some positions in the bulk sample. Here their spin polarization evolve as an effect of the local magnetic interactions, until the particles decay according to

$$\mu \longrightarrow e^+ + \nu_e + \bar{\nu}_\mu \tag{2.15}$$

with a mean lifetime of approximately $2.2\,\mu s$, which makes muons suitable to probe magnetic interactions on the microseconds timescale. Once again the decay is led by the weak interaction and a parity violation occurs: this yields an anisotropic emission of the positron, more pronounced for higher positron energy.

The angular distribution of the decay probability density is shown for different positron energies in figure 33 and is given by

$$W(\theta) = 1 + a\cos\theta, \tag{2.16}$$

where θ is the angle between the muon spin and the direction of the positron emission and the factor $0 \leqslant a \leqslant 1$, increases monotonically with the positron energy. Most of the positrons are emitted in the direction the muon spin was pointing at just before the decay and thus their detection allow to **measure the time evolution of the muon spin polarization P(t)**.

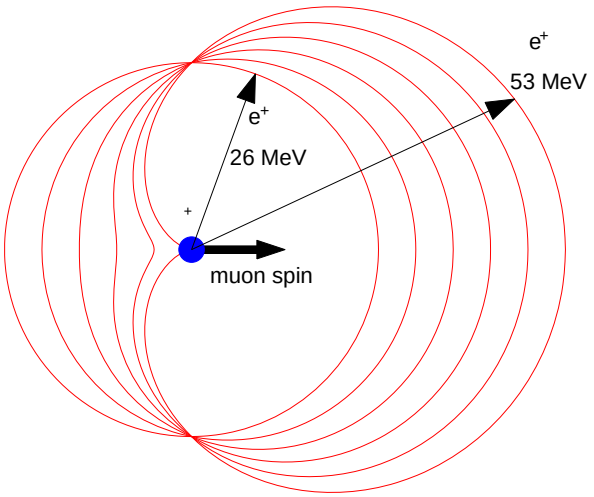

Figure 33. Angular probability distribution for the positrons emitted by the decay of a μ^+, for different positron energies. The positrons are preferentially emitted in the direction the muon spin had just before the decay.

In summary, in a μSR experiment muons are implanted in the sample, their spin polarization evolve as an effect of the external and local magnetic fields and finally they decay emitting a detectable positron in the direction of their final polarization. These positron are detected by means of scintillators, connected to photomultipliers for amplification, to obtain P(t) measurements.

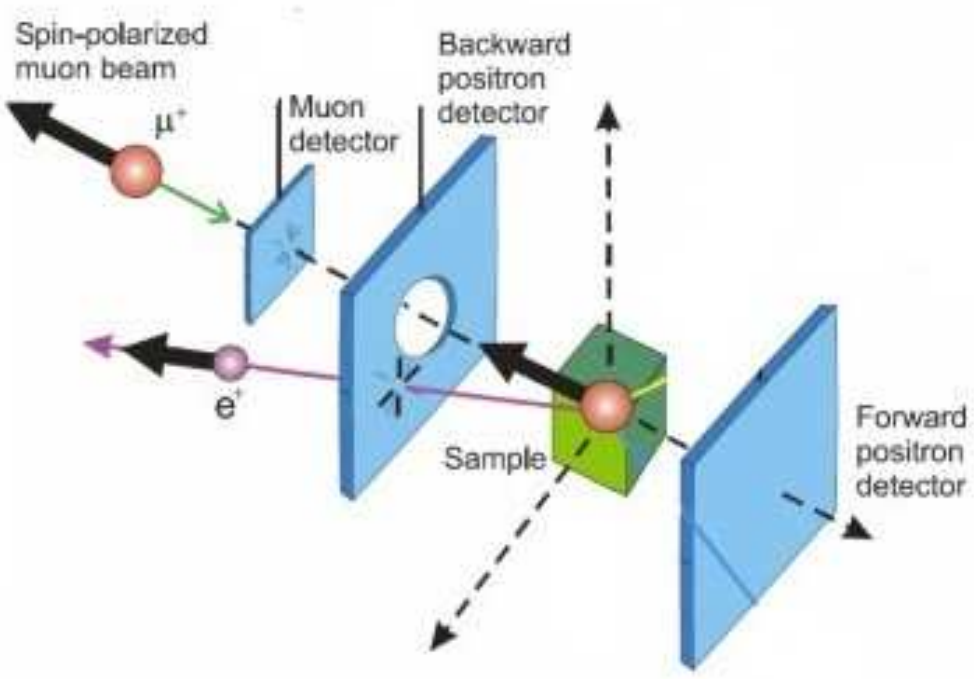

Figure 34. Schematic representation of a ZF or LF μSR experiment. The detectors are arranged in two groups (forward and backward).

Because of geometrical constraints, generally two sets of detectors are employed: for ordinary longitudinal field measurements they are disposed as sketched in figure 34, in forward and backward directions with respect to the muon momentum. The counts of these two detector banks are separately summed up and the time evolution of the difference between forward (F) and backward (B) counts in principle describes the time evolution of the muon spin polarization. However, two important corrections must be taken into account:

- The exact difference of the F and B counts correctly describes the system only if the two sets of detectors are arranged in an ideal geometrical way, which is never the case. For this reason the counts of the backward detectors N_B are considered as miscalibrated by a factor α, called the *asymmetry* of the detectors. The effective backward counts are given by $N_B^{true} = \alpha \cdot N_B$.

- The number of counts exponentially reduces with time by the effect of the radioactive decay of the muons. This reduction of the signal is intrinsic in the technique, but it contains no useful information and can be removed. The most relevant physical quantity is considered the *decay asymmetry* or *polarization*

$$P = \frac{N_F - \alpha N_B}{N_F + \alpha N_B} \tag{2.17}$$

  P represents the asymmetry of the forward and backward counts normalized point by point for the effect of the statistics of muon decay and therefore its time evolution reflects the true sample behaviour. The parameter α can be directly calibrated by a measurement in a low applied transverse field, typically of 20 or 100 G (these measurements are known as TF20 and TF100).

The two most common experimental configurations used in μSR experiments (actually we have already mentioned them) are the transverse field (TF) and longitudinal field geometry (LF or ZF if the magnetic field is set to zero). In the former the magnetic field is applied in a direction perpendicular to the muon polarization: the spins are thus forced to precess around this field at the frequency $\omega = \gamma_\mu H$ and an oscillating signal is observed[11]. In the latter, on the contrary, the external field $\vec{H}$ is applied along the same direction of the muon spin. In general it will add to the local fields and, if it is large enough, it will keep the muon polarization fixed in the original direction.
The measurements performed on graphene and ball-milled graphite, shown in the experimental sections, were mainly performed in the longitudinal ZF geometry, with the aim to observe the muons precession induced by the internal fields[12]. Therefore it is worth discussing here the different behaviours that can be expected for the muon spin polarization in ZF, at least in the most significative physical situations. Next section takes care of this issue for the case of solid state powder samples, with a special focus on the dipolar interaction among nuclear and muon spins.

[11] A spin precession motion is seen as an oscillating signal because the detectors are disposed along one direction only (let's say the z axis) an the projection of a circular motion onto an axis is a cosinusoidal oscillation.

[12] TF measurements were routinely used too, but only for calibrations and they will not be further discussed. In the experimental section, instead, minor experiments dedicated to the study of the signal changes under increasing LF are also reported.

2.2.2 Muon precession and relaxation in ZF

When the muon μ^+ is implanted in the sample it can either remain as a free particle in an equilibrium position of minimum electrostatic energy, "jump" among different equivalent sites, or form a bound state with an electron, called *Muonium*: this is essentially a light hydrogen isotope and from the chemical point of view acts exactly as an hydrogen atom and can covalently bind to the sample.
Once stopped in the sample, each muon spin, in principle, precesses around the local effective field $\vec{H}_{eff}$ present at the muon site. However only in a few cases it is actually possible to observe a single frequency *coherent oscillation* in the μSR signal. In particular the polarization can be described by an harmonic wave in two main situations of interest:[13]

- if all the muons probe a constant and uniform local field within the sample, that is in the presence of **long range magnetic order**, either of ferromagnetic (FM) or antiferromagnetic (AFM) type.

- for muonated **radical species**, which is often the case for organic unsaturated molecules [114]; like in an hydrogen addition reaction, muonium *breaks* a double bond present in the molecule and yields a *muonated* molecule with an unpaired electron. A simple example is ethylene $H_2C = CH_2$ which forms the paramagnetic *ethyl radical* $H_2\dot{C} - CH_2Mu$. Actually in a such a state, a ZF analysis generally shows a *missing fraction* rather than an oscillation, as the related frequency is so high (typically a few hundreds kHz or more) that most of the times is out of the spectrometer bandwidth[14]. The radical formation can be verified either by the application of a small TF (2 G), which is expected to induce transitions among the muonium triplet states (see fig.35), or by measurements as a function of an applied LF, which allow to observe the repolarization of the initial asymmetry[115].

Coherent oscillations that are beats made up of more than one frequency can instead be observed when the muon interacts with a few surrounding nuclei, case that will be discussed in detail below, as it is of particular interest for the present study.

[13]Here we are leaving out several special cases where coherent oscillations are also observed, like spin density waves [122], where however the polarization is described by a Bessel function rather than by an harmonic wave.

[14]The expression missing fraction is used to indicate that in the μSR signal at $t = 0$ only a part of the full asymmetry is observed, while the fraction of muons which form the radical species is missing.

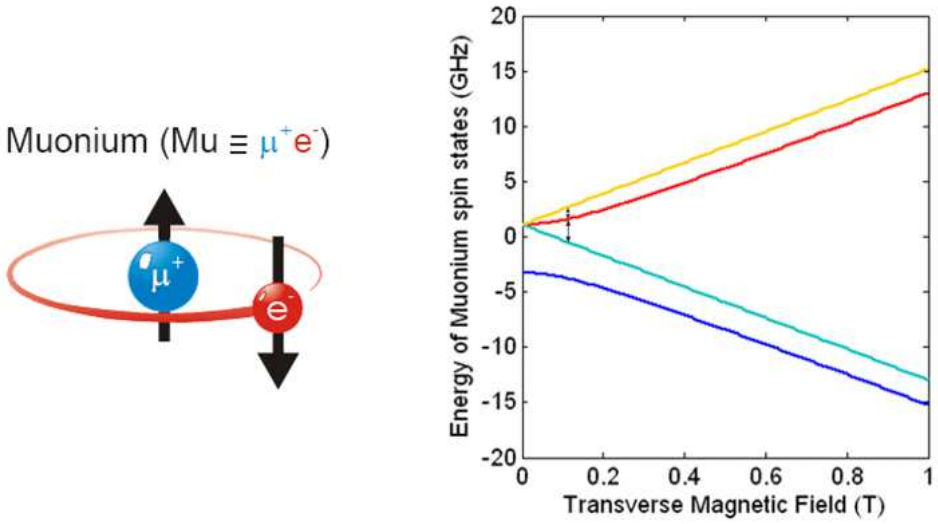

Figure 35. a. A simple picture of Muonium. **b.** The Breit-Rabi diagram for free Muonium in vacuum: the plot shows Muonium spin energy levels as a function of the applied transverse magnetic field. In a low TF (a few Gauss) is possible to observe the two nearly degenerate transitions among the triplet states, highlighted by the black arrows on the left (the corresponding precession frequency can be detected).

In most situations, on the contrary, a *relaxation* of the muon polarization is expected. A common case is when the muon, stopped in an electrostatic equilibrium position, experiences randomly oriented dipolar fields (with zero average) from neighbouring electrons and nuclei: this is usually described by a Gaussian (approximation of relatively high concentration [123]) or Lorentzian (approximation of dilute spin system [124]) **static field distribution**. The resulting polarization turn out to follow the gaussian or lorentzian Kubo-Toyabe function:

$$\begin{aligned} P(t) &= \frac{1}{3} + \frac{2}{3}\left(1-\sigma^2 t^2\right) e^{-\sigma^2 t^2/2} \\ P(t) &= \frac{1}{3} + \frac{2}{3}\left(1-\lambda t\right) e^{-\lambda t} \end{aligned} \tag{2.18}$$

where the relaxation rate σ and λ describe the width of the local field distribution function at the muon site[15].

If the muons jump between different positions or if static muons sense **fluctuations in the local fields** the mathematical description is more complicated and, in principle, system-specific numerical simulations should be performed.

[15]The constant factor 1/3 is present in most functions describing muon polarization in powder samples and deserve a brief explanation. Its mathematical derivation is not simple [125, 123, 126] and we will limit to an heuristic consideration: on the average, 1/3 of the muons sense a magnetic field parallel to the initial polarization direction, while 2/3 feel a transverse field. The latter start to precess and thus dephase progressively yielding the decaying part of the signal

However in the strong collision approximation (extreme motional narrowing regime in NMR language) the resulting relaxation function can be shown to take a simple Lorenztian form ($e^{-\lambda t}$). This is appropriate for several physical situations, including the fast fluctuations of paramagnetic electrons.

2.2.3 Dipolar interactions with a few nuclei: the μ-H and μ-D cases

A special case that is worth discussing in details occurs when the muon stops at particular sites where only one or two nearby nuclei produce a dipolar field much higher than all the others. It is then possible to neglect the rest of the system and solve the quantum mechanical few spins problem, in order to directly obtain the analytical expression for the polarization. In the following we deal in particular with the cases of hydrogen and deuterium and we can anticipate that, as a general result, the muon interaction with the strong nuclear fields gives origin to beats of the dipolar frequency and its multiples in the μSR spectrum.

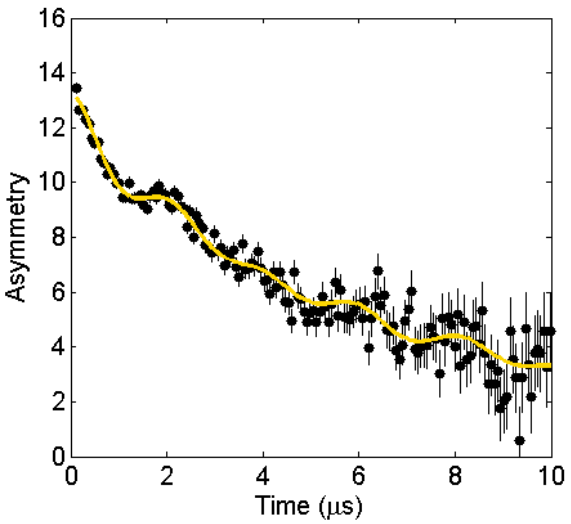

Figure 36. ZF μSR data in $(AsF_6)_2C_{60}$ at 1.4 K, displaying the typical oscillating signal from the F-μ-F dipolar interaction.

The prototype example is the F-μ-F interaction, first investigated in the 80s by Brewer and coworkers [127]. In many fluorinated compounds the muon is easily attracted by the high electrostatic potential of fluorine and tend to sit between two atoms to form collinear F-μ-F configurations. Fingerprint of the dipolar interaction among the muon spins and the two nuclei are beats of the form[16] [128]

$$\langle P(t)\rangle = \frac{1}{6}\left[3 + \cos(\sqrt{3}\,\omega_D\,t) + \left(1+\frac{\sqrt{3}}{3}\right)\cos\left(\frac{3-\sqrt{3}}{2}\,\omega_D\,t\right) + \left(1-\frac{\sqrt{3}}{3}\right)\cos\left(\frac{3+\sqrt{3}}{2}\,\omega_D\,t\right)\right] \tag{2.19}$$

[16]In eq.(2.19) $\langle\cdots\rangle$ denotes that the powder average have been perfomed and ω_D is the dipolar frequency, which accounts for the energy of the interaction. Its precise definition is given below for the μ - H case.

like the one displayed in figure 36 for the case of the fullerenium salt $(AsF_6)_2C_{60}$. This system, recently synthesized and characterized by my coworkers[129], provide an up-to-date example on how μSR can be used to study the local geometry of the fluorinated species [130].

The μ-H interaction

Of direct interest for the present work is the hyperfine dipolar interaction between the muon spin $\vec{I}$ and the spin $\vec{S}$ of a single hydrogen nucleus (μ-**H**). The related Hamiltonian can be written as

$$\begin{aligned} \mathcal{H} &= -\frac{\mu_0}{4\pi r^3}\hbar^2\,\gamma_\mu\,\gamma_H\left[3\left(\vec{I}\cdot\hat{r}\right)\left(\vec{S}\cdot\hat{r}\right)-\vec{I}\cdot\vec{S}\right] \\ &= -\hbar\omega_D\left[3\left(\vec{I}\cdot\hat{r}\right)\left(\vec{S}\cdot\hat{r}\right)-\vec{I}\cdot\vec{S}\right] \end{aligned} \tag{2.20}$$

where, for convenience, the front coefficients and the dipole-dipole distance r are included in the definition of the dipolar frequency $\omega_D = -\hbar\,\gamma_\mu\,\gamma_H\,\frac{\mu_0}{4\pi r^3}$.
Chosen a reference frame with the z axis oriented along the dipole axis this become

$$\mathcal{H} = -\hbar\omega_D\,\left(2I_zS_z - I_xS_x - I_yS_y\right)\,.$$

Starting from ordinary spin Pauli matrices ($I = S = \frac{1}{2}$), it is possible to evaluate this Hamiltonian in the (4×4) tensor space obtained from the spins direct product. The detailed calculations, from the diagonalization of $\mathcal{H}$ to the computation of the muon spin polarization, can be found in the literature [131] and finally yield

$$\langle P(t)\rangle = \frac{1}{6}\left[1 + \cos\left(\omega_D t\right) + 2\cos\left(\frac{1}{2}\omega_D t\right) + 2\cos\left(\frac{3}{2}\omega_D t\right)\right]. \tag{2.21}$$

The latter equation is the model function to be used for the interpolation of ZF μSR data in powder samples where the muon experience the nuclear dipolar field of an hydrogen atom.
The calculations are intentionally omitted here, because they will result apparent in the following, where their extension to the case of deuterated samples is considered[17].

The μ-D interaction

As will emerge in chapter 5 the investigation of isotopically substituted species proved necessary for the correct interpretation of μSR data. It is then worth to extend the

[17]For the sake of completeness and for future reference, however, the calculations for the μ-H case are reported in appendix A.

existing theory to the **muon-deuterium interaction**. The μ-D Hamiltonian is no more limited to the dipolar term, but it must also include the deuterium quadrupolar contribution (spin $D = 1$). ^2H NMR experiments (see section 5.4) have shown that graphene display a vanishing asymmetry of the quadrupolar interaction ($\eta = 0$), as expected for a 2DIM material. Within this approximation the full Hamiltonian is:

$$\begin{aligned}\mathcal{H} \;=& -\hbar\omega_D \left[3\left(\vec{I}\cdot\hat{r}\right)\left(\vec{D}\cdot\hat{r}\right) - \vec{I}\cdot\vec{D}\right] + \\ &+ \frac{eQV_{ZZ}}{4D(D+1)\cdot 2}\left(3\cos^2\beta - 1\right)\left[3D_z^2 - D(D+1)\right]\end{aligned} \tag{2.22}$$

Here the dipolar frequency is defined like in the μ-H case and the quadrupolar parameters are the same introduced in the NMR section (2.1). β is the angle between the dipole axis and the direction of the electric field gradient at the deuterium site (Z principal axis of the quadrupolar interaction).
It is convenient to define also the quadrupolar frequency ω_Q and the quadrupolar constant k_Q as

$$\omega_Q \;=\; \frac{3eQV_Z Z}{4D(2D-1)\hbar} \qquad\qquad k_Q \;=\; \frac{\omega_Q}{2}\left(3\cos^2\beta - 1\right) \tag{2.23}$$

and, if once again a reference frame with the z axis oriented along the dipole axis is chosen, the Hamiltonian reduces to

$$\begin{aligned}\mathcal{H} \;=& --\hbar\omega_D\left(2I_zS_z - I_xS_x - I_yS_y\right) + \\ &+ \frac{\hbar k_Q}{3}\left[3D_z^2 - D(D+1)\right]\end{aligned}$$

The last term $D(D+1)$ is a constant and introduce only a rigid shift of the energy levels: as far as we are interested in the muon precessing frequencies (i.e. in energy differences) this part can be neglected and the latest expression further simplifies to

$$\mathcal{H} \;=\; -\hbar\omega_D\left(2I_zS_z - I_xS_x - I_yS_y\right) + \hbar\, k_Q\, D_z^2\,. \tag{2.24}$$

In the following the time evolution of the muon spin polarization is evaluated starting from the Hamiltonian (2.24). The various steps of these calculations are only sketched out, while algebraic manipulations and some minor maths operation (e.g. computation of some tensor products) are reported in appendix B.

1. First consider the Pauli spin matrices for the muon spin ($I = 1/2$) and for the deuterium spin ($D = 1$):

$$I_x \;=\; \frac{1}{2}\begin{pmatrix}0 & 1\\ 1 & 0\end{pmatrix} \qquad I_y \;=\; \frac{1}{2}\begin{pmatrix}0 & -i\\ i & 0\end{pmatrix} \qquad I_z \;=\; \frac{1}{2}\begin{pmatrix}1 & 0\\ 0 & -1\end{pmatrix}$$

$$D_x = \frac{1}{\sqrt{2}}\begin{pmatrix} 0 & 1 & 0 \\ 1 & 0 & 1 \\ 0 & 1 & 0 \end{pmatrix} \qquad D_y = \frac{1}{\sqrt{2}}\begin{pmatrix} 0 & -i & 0 \\ i & 0 & -i \\ 0 & i & 0 \end{pmatrix} \qquad D_z = \frac{1}{\sqrt{2}}\begin{pmatrix} 1 & 0 & 0 \\ 0 & 0 & 0 \\ 0 & 0 & -1 \end{pmatrix}$$

2. The different terms of the Hamiltonian can be evaluated as direct products of these spins in a (6×6) tensor space (in the products deuterium is chosen as the outer components, while the muon is associated to the inner component). For example:

$$D_z \otimes I_z = \frac{1}{2}\left(\begin{array}{cc:c:cc} 1 & 0 & & & \\ 0 & -1 & 0 & 0 & \\ \hdashline & & & & \\ 0 & & 0 & 0 & \\ \hdashline & & & -1 & 0 \\ 0 & & 0 & 0 & 1 \end{array}\right)$$

The total Hamiltonian turns out to be

$$\mathcal{H} = \hbar\begin{pmatrix} -2\omega_D + k_Q & 0 & 0 & & & \\ 0 & +2\omega_D + k_Q & \frac{\sqrt{2}}{2}\omega_D & & 0 & \\ 0 & \frac{\sqrt{2}}{2}\omega_D & 0 & & & \\ & & & 0 & \frac{\sqrt{2}}{2}\omega_D & 0 \\ & 0 & & \frac{\sqrt{2}}{2}\omega_D & +2\omega_D + k_Q & 0 \\ & & & 0 & 0 & -2\omega_D + k_Q \end{pmatrix} \tag{2.25}$$

For clarity in the subsequent calculations the D and Q subscripts of the dipolar frequency ω and quadrupole constant k will be omitted and we define the additional parameter α as

$$\alpha = \sqrt{6\omega^2 + 4\omega k + k^2} \tag{2.26}$$

3. The computation of the energy eigenvalues λ_i yields

$$\lambda_{1,2} = \hbar(-2\omega + k) \qquad \lambda_{3,4} = \frac{\hbar}{2}(2\omega + k - \alpha) \qquad \lambda_{5,6} = \frac{\hbar}{2}(2\omega + k + \alpha) \tag{2.27}$$

and the matrix U that express the transformation from the basis set of I_z, D_z to the basis set of the energy eigenstates (commonly called the "matrix of the eigenvectors")

results [18]

$$U = \hbar \left(\begin{array}{cc:c:c:c:c} 1 & 0 & 0 & 0 & 0 & 0 \\ 0 & 0 & 0 & \frac{2\omega+k-\alpha}{\omega\sqrt{2}} & 0 & \frac{2\omega+k+\alpha}{\omega\sqrt{2}} \\ 0 & 0 & 0 & 1 & 0 & 1 \\ 0 & 0 & -\frac{2\omega+k+\alpha}{\omega\sqrt{2}} & 0 & -\frac{2\omega+k-\alpha}{\omega\sqrt{2}} & 0 \\ 0 & 0 & 1 & 0 & 1 & 0 \\ 0 & 1 & 0 & 0 & 0 & 0 \end{array} \right) \tag{2.28}$$

4. The diagonal form of the Hamiltonian allows to easily evaluate the time evolution operator

$$E_{diag}(t) = e^{-i\frac{\mathcal{H}}{\hbar}t}$$

which back in the basis set of angular momenta (I_z and D_z) is given by

$$E(t) = U\, E_{diag}(t)\, U^{-1}$$

5. As we deal with LF μSR experiment, we now need to change the reference frame from the principal axes of the dipolar interaction to a new coordinate system (x', y', z') whose z' axis is oriented along the initial muon spin polarization. The muon spin projection along the dipole axis (which we call I_ζ and not I_z anymore, in order to stress we are writing it in a different reference frame) is now given by

$$I_\zeta = I_{z'}\cos\theta + I_{x'}\sin\theta = \frac{1}{2}\cos\theta \begin{pmatrix} 1 & 0 \\ 0 & -1 \end{pmatrix} + \frac{1}{2}\sin\theta \begin{pmatrix} 0 & 1 \\ 1 & 0 \end{pmatrix} = \frac{1}{2}\begin{pmatrix} \cos\theta & \sin\theta \\ \sin\theta & -\cos\theta \end{pmatrix}$$

and in the tensor space it is written as

$$I_\zeta = \mathbb{I}_3 \otimes I_\zeta = \frac{1}{2}\begin{pmatrix} \cos\theta & \sin\theta & 0 & 0 \\ \sin\theta & -\cos\theta & & \\ 0 & & \cos\theta & \sin\theta \\ & & \sin\theta & -\cos\theta \end{pmatrix}$$

6. The polarization observed in μSR is the expectation value of this operator and can be obtained as

$$P(t) = Tr\,[E(t)\, I_\zeta\, E(-t)\, I_\zeta] \tag{2.29}$$

[18] As indicated by the dotted lines, the eigenvectors in these matrix are ordered by columns. Notice that this convention, although very common, is opposite to the one used in the *Mathematica* software, generally used to handle similar symbolic matrices. According to this convention the diagonal form of the Hamiltonian is given by $\mathcal{H}_D = U^{-1}\mathcal{H}U$.

After proper algebraic manipulations this results

$$\begin{aligned} P(t) \;=\; & \frac{1}{2\alpha^2}\,\cos^2\theta\,\left[3k^2 \,+\, 12k\omega \,+\, 14\omega^2 \,+\, 4\omega^2\cos\left(\alpha t\right)\right] \,+ \\ & +\,\frac{1}{4\alpha^2}\,\sin^2\theta\,\left\{2\omega^2\cos\left(\alpha t\right) \,+\, 2\left(\alpha^2-\omega^2\right) \,+\right. \\ & \left(\alpha^2-k\alpha-2\omega\alpha\right)\,2\cos\left(\frac{k-6\omega+\alpha}{2}\,t\right) \,+ \\ & \left.\left(\alpha^2+k\alpha+2\omega\alpha\right)\,2\cos\left(\frac{k-6\omega-\alpha}{2}\,t\right) \,+\right\} \end{aligned} \tag{2.30}$$

This expression describe the muon spin polarization for the case of a single crystal with the dipole axis which form an angle θ with respect to $P(0)$.

7. For polycrystalline samples the "powder average" over all possible orientations [132] must be performed

$$\langle P(t)\rangle \;=\; \frac{1}{8\pi^2}\int_0^{2\pi} d\alpha \int_0^{2\pi} d\gamma \int_0^{\pi} d\theta\,\sin\theta\,P(t) \tag{2.31}$$

This yields

$$\begin{aligned} \langle P(t)\rangle \;=\; & \frac{1}{6\alpha^2}\,\left[\left(5k^2 \,+\, 20\omega k \,+\, 4\omega^2\right) \,+\, 6\omega^2\cos\left(\alpha t\right) \,+\right. \\ & +\,2\left(\alpha^2-k\alpha-2\omega\alpha\right)\,\cos\left(\frac{k-6\omega+\alpha}{2}\,t\right) \,+ \\ & \left.+\,2\left(\alpha^2+k\alpha+2\omega\alpha\right)\,\cos\left(\frac{k-6\omega-\alpha}{2}\,t\right)\right] \end{aligned} \tag{2.32}$$

Eq.(2.32), made up of beating oscillations depending on both the dipolar and quadrupolar frequencies, is the model function that can be employed to fit ZF μSR data for the case of the muon-deuterium interaction.

2.3 DC SQUID Magnetometry

Magnetometry is the experimental technique devoted to measure the bulk magnetic response of a sample. Among all the different types of magnetometers, the Superconducting Quantum Interference Device (SQUID) can reach in principle the highest sensitivity (optimized SQUID devices have been used to measure the magnetic fields of human brain, of the orders of several fT [133]). For this reason SQUID technology has become widely used and it is the most common among commercially available magnetometers. A SQUID-based Magnetic Properties Measurement System from Quantum Design has been used to characterize all the samples studied in this work.
Essentially a SQUID magnetometer is a transducer that convert a magnetic flux variation into a voltage output [134]. Its working principle, outlined below, relies on the electronic properties of a Josephson junction and is an amazingly simple application of superconductivity and quantum physics. Its relative simplicity is probably the reason why SQUID magnetometry was developed in a record short time: in 1962 Brian Josephson postulated the homonymous effect [135, 136], a year later John Rowell and Philip Anderson at Bell Labs built the first Josephson junction and it took only one more year to a team of scientist from Ford Research Labs to develop the idea of the SQUID magnetometer in 1963 (Jaklevic, Lambe, Silver, Mercereau [137]).

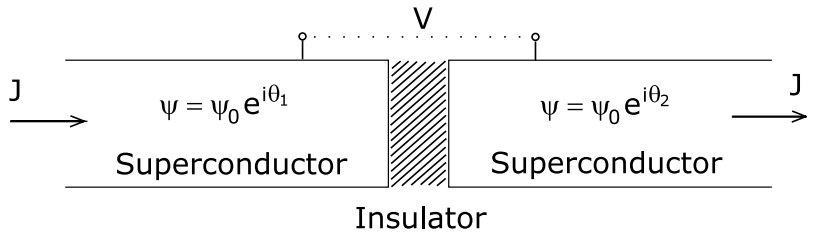

Figure 37. Schematic representation of the Josephson junction.

The Josephson junction

A Josephson junction is made out of two pieces of a superconducting material interrupted by an insulating slab, thin enough to let the superconductor charge carriers (the Cooper pairs) *tunnel* across the junction (fig.37).
The superconducting wavefunction can be written in the form $\psi = \psi_0 e^{i\theta}$ and is identified by a magnitude ψ_0 and a complex phase θ. If the two superconducting regions were in direct contact they would have the same phase, while the finite tunneling probability across the Josephson junction leads to a well-defined relation among the phase values, usually called a *weak link* between the two superconductors. In particular

the phase difference is related to the number of tunneling particles and hence to the current density by the relation

$$J = J_0 \sin\delta_0 \,,\ \delta_0 = \theta_1 - \theta_2 \tag{2.33}$$

The corresponding voltage can be computed as

$$V = \frac{\hbar}{2e}\frac{d\delta_0}{dt}$$

Notice that according to the last equation a static phase difference (and stationary current) does not generate any voltage across the junction. Thus in these conditions the junction can be considered to act as an extended superconductor.

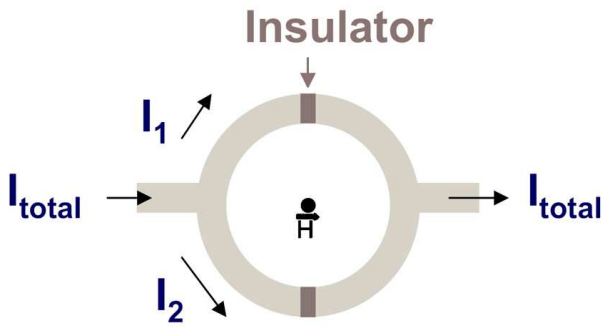

Figure 38. Schematic illustration of a SQUID device, made out of a superconducting ring and two Josephson junctions.

The Superconducting Quantum Interference Device

A Direct Current SQUID consist in a superconducting ring, interrupted by two Josephson junctions in parallel configuration, as depicted in fig.38. A bias current is maintained in the ring and flow equally through the two branches. When a magnetic flux Φ is concatenated with the loop (e.g. due to the magnetic moment of a sample), it generates an extra phase shift in the two tunnel junctions A and B, opposite in sign[19]

$$\delta_A = \delta_0 + \frac{e}{\hbar}\Phi \qquad \delta_B = \delta_0 - \frac{e}{\hbar}\Phi$$

and from eq.(2.33) the total current density becomes

$$J = J_A + J_B = 2\,J_0 \cos\left(\frac{e\Phi}{\hbar}\right) \sin\delta_0 \,. \tag{2.34}$$

[19]The induction of a phase shift by a magnetic field is a quantum mechanical effect, known in quantum optics as the Aharonov-Bohm effect.

The current is therefore periodic in Φ and the **output voltage** turns out to be also periodic with a period which equal a single flux quantum $\Phi_0 = \frac{h}{2e} = 2 \cdot 10^{-15}\, T\, m^2 = 2 \cdot 10^{-5}\, G\, mm^2$.
This accounts for the high sensitivity of SQUID magnetometers.

Actually the SQUID ring is not directly used to measure the sample moment, as it would be strongly disturbed by the possible fluctuations of the high magnetic fields applied for measurements. The SQUID is then generally placed in a region isolated from the effect of external fields and it is coupled to a superconducting circuit where the magnetic flux variation is measured by a specific pick-up coil, arranged in a second order gradiometer configuration. As displayed in fig.40, this is composed by four aligned identical turns, the inner ones wound clockwise and the outer ones counterclockwise: this special geometry has the advantage that it measures only the gradient of the magnetic field, while any constant external field does not contribute to the signal.

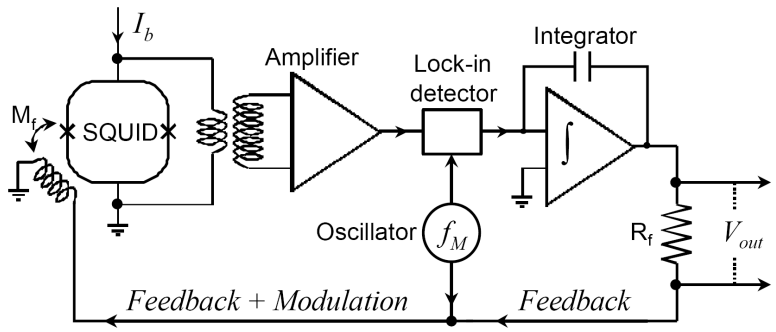

Figure 39. Fluxed Locked Loop (FLL) configuration for SQUID electronics. A change in the magnetic field at the pick-up coil (inductance L_p) induces a change in the field at the input coil (inductance L_i). The SQUID is inductively coupled to the input coil and detects a change in the related magnetic flux. However the SQUID voltage response is not used directly: a Flux Locked Loop modulation circuit is used to reduce electronic noise and improve the linearity of the SQUID response (until now we have neglected the presence of the field in the Josephson junctions regions: the latter cause the current to follow a *sinc* function rather than a sinusoidal function and this intensity loss for high fluxes must be corrected). The final output voltage V_0 is proportional to the field at the pick-up coil [138].

To perform a measurement the sample is moved along the gradiometer's axis and thus generates a signal that is transferred to the SQUID loop to yield the final voltage output, thanks to the control of an appropriate electronics(see fig.39). The flux variation induced by moving the sample through the pick-up coil can be evaluated from the relation

$$\Phi_B = \frac{\mu_0\, m\, R^2}{2\,(x^2 + R^2)^{3/2}}$$

expressing the flux of the magnetic moment **m** having position x along the axis of a coil with radius R. The corresponding induced voltage V turns out to be

$$V(x) \propto \frac{\mu_0\, m\, R^2}{2} \sum_{i=1}^{4} \left[(x+d_i)^2 + R^2\right]^{-3/2} \tag{2.35}$$

where d_i indicate the relative positions of the single coils in the gradiometer configuration. The voltage detected as a function of sample position (averaged over several scans) is fitted with eq.(2.35) to yield the measurement of the magnetic moment (a typical curve is shown in figure 40).

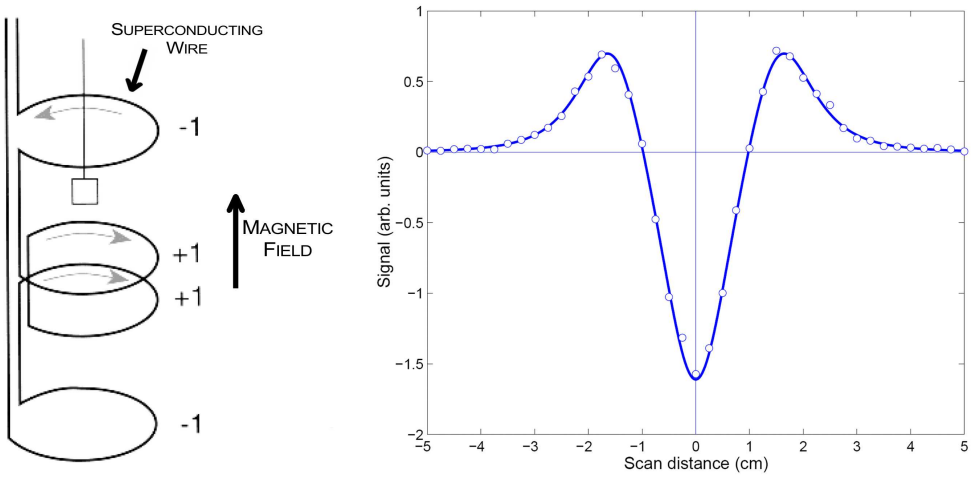

Figure 40. Left. Second-order gradiometer pick-up coil. This configuration decouples the SQUID response from the external applied field, so that only the sample magnetic moment is measured. Adapted from [138]. **Right.** A typical SQUID signal for a diamagnetic sample. Its functional form is described by eq.(2.35).

2.3.1 Probed magnetic properties

Magnetometry measurements can be easily performed as a function of temperature and magnetic field: in the case of the instrument used here, the Quantum Design MPMS XL 5, fields up to 5 T and the temperature range $2 \cdots 400\, K$ were available. Such measurements allow to explore and characterize the magnetic properties of materials. In the following it is assumed that the reader is familiar with the fundamental magnetic phases of matter, whose temperature and field dependence of the magnetization are recalled in fig.42. Therefore the discussion will be limited to the **two aspects that were accurately studied in all the considered graphene samples** and this part is intended only to offer a guideline for the analysis of the magnetic data shown in the next chapters.

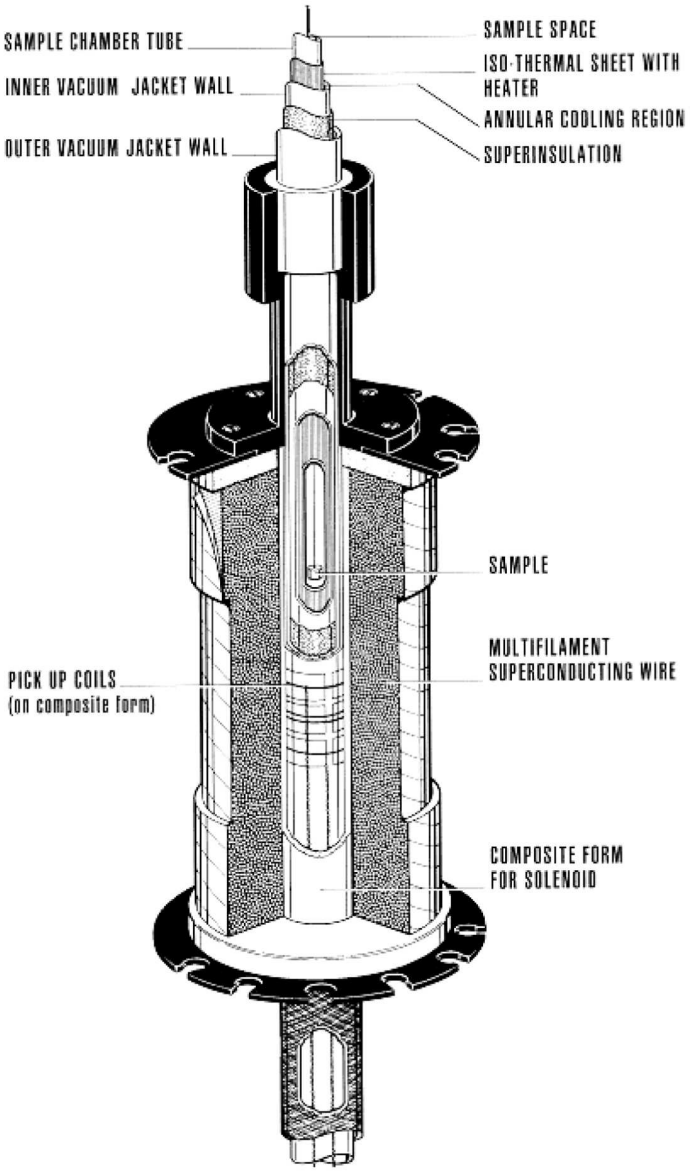

Figure 41. Longitudinal section of the sample space for the commercial SQUID used for this work: the second order gradiometer pick-up coils and the external superconducting main coil for the production fo the magnetic field (up to 5T) are highlighted. From [138].

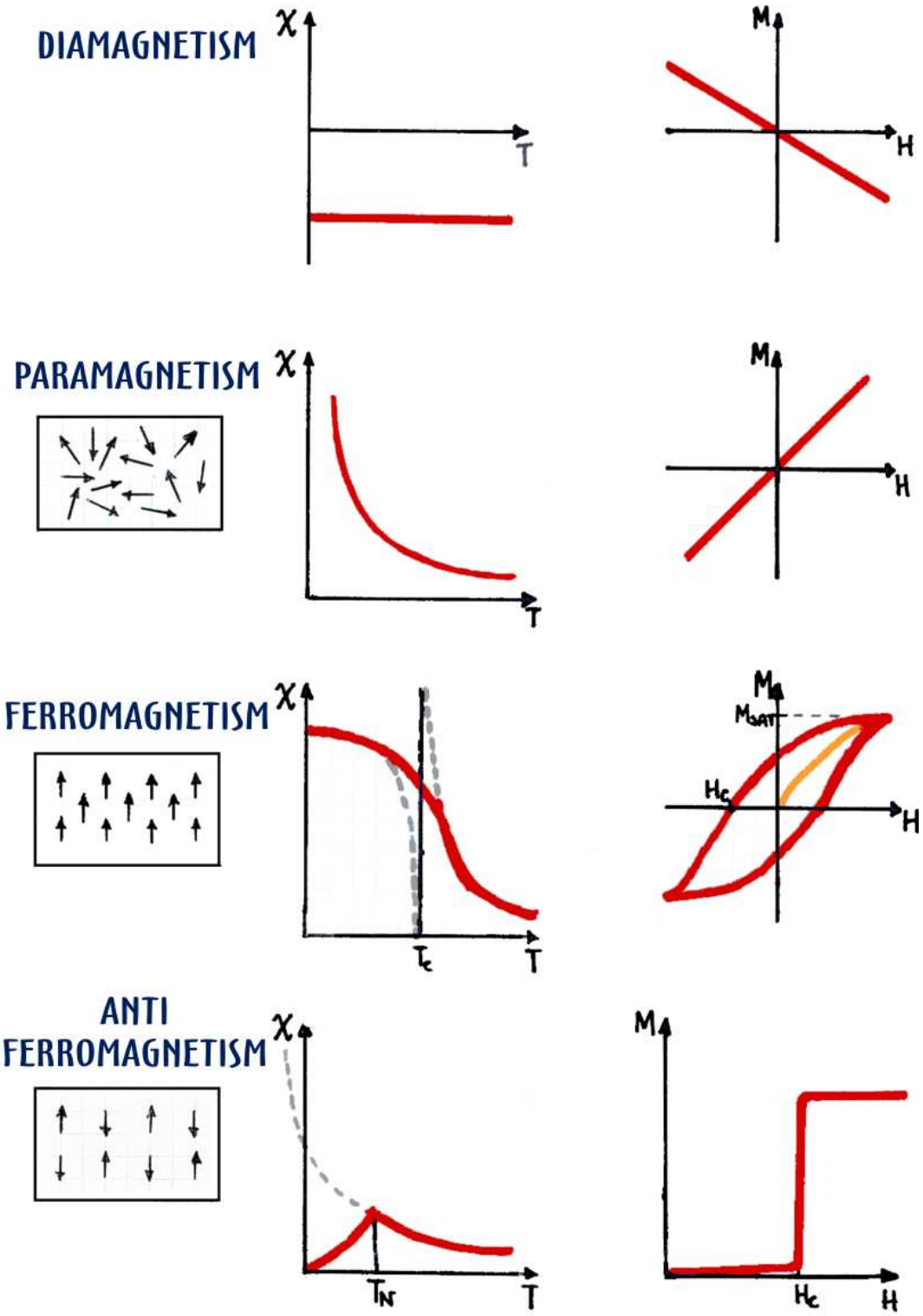

Figure 42. Schematic diagram of the Temperature and Field dependence of Magnetization in the main magnetic phases of solid state materials. For the AFM case it has been represented the $M(H)$ curve in case of strong magnetocrystalline anisotropy.

Magnetic impurities

The first SQUID characterization considered has been the study of the *field dependence of magnetization at room temperature* (M(H) at 300 K). These type of measurement on the one hand offers a first insight into the bulk magnetic response of the material; on the other it allows a fast estimation of the magnetic impurities content in the samples. As already mentioned, graphene revealed to be essentially diamagnetic and thus it's worth focusing our attention to the latter aspect. For clarity, in the following it is assumed that all the ferromagnetic contribution observed come from impurities and not from the sample (this proved to be actually true for the investigated samples).
Ferromagnetic (FM) impurities, like Nickel, Iron and Cobalt are often present in chemically synthesized samples, even when they are prepared with the greatest care. To be aware of the sample impurities content can be important whenever weak magnetic effects are expected, like in the case of the possible magnetic phases of carbon materials [139]. Magnetic metallic elements all have high transition temperatures, well above 300 K and then room temperature is probably one of the best temperature to detect them, as they are not hidden by paramagnetism and other interactions that can dominate at low temperatures.

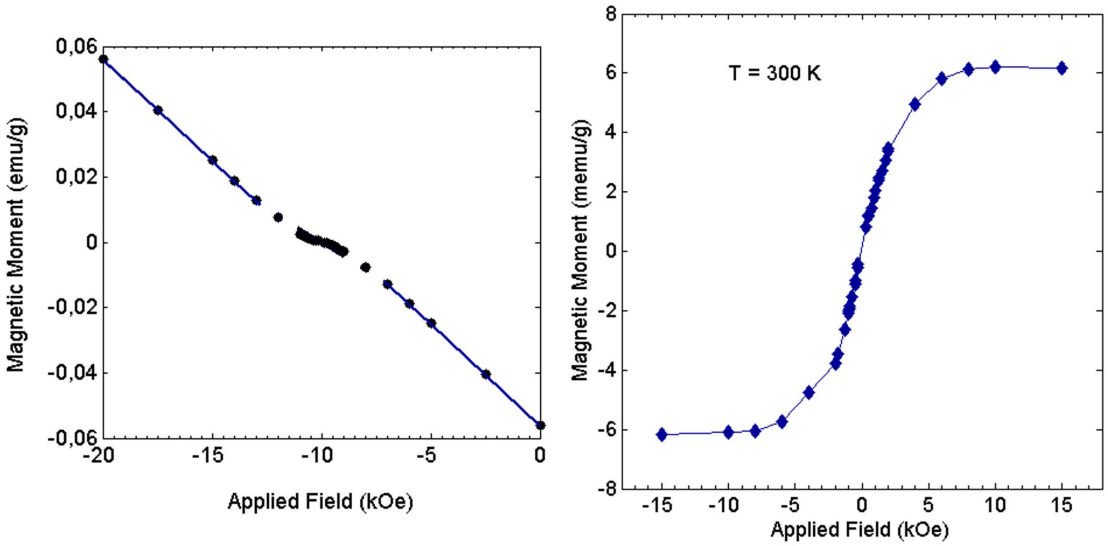

Figure 43. Left panel. M(H) data at 300 K from a graphene sample. The diamagnetism is superimposed to the ferromagnetic impurities contribution, which is reported alone in the **Right panel**.

A magnetic impurities contribute to the SQUID signal with an hysteresis curve, like the one depicted in the right panel of figure 43. This can be easily observed once the diamagnetism (or paramagnetism) of the bulk sample have been subtracted from the data, by means of a linear fit of the high filed region, where the FM contribution is

constant (left panel). The key parameters to be evaluated are the *saturation magnetization* M_{SAT} and *saturation field* H_{SAT}, also evidenced in the figure. The latter is important as an experimental parameter, in the sense that any measurement as a function of temperature has to be performed at a higher field, in order to get rid of the spurious contribution of FM impurities: indeed if a field $H < H_{SAT}$ is applied the magnetization $M(T)$ would be strongly affected from the FM component; if, on the contrary a higher field is used, the impurities contribution will be limited to a constant baseline. The saturation magnetization, instead, provide the estimation of the magnetic impurities content. Indeed its value, tipically of the order of several memu/g, is commonly expressed in equivalent content of iron (in ppm): within the simplifying hypothesis that all the impurities are iron (218 emu/g), one memu/g approximately corresponds to 4.5 ppm of iron.

Defects concentration: paramagnetism

In graphene magnetometry can be exploited as a tool for characterizing the defects concentration in the sample. Many of the defects discussed in section 1.7, indeed, are populated by a paramagnetic electron, including in-plane vacancies and edges [10]. Since graphene has a diamagnetic response, the paramagnetic contribution observed in the temperature dependence of magnetization can be attributed to these paramagnetic defect sites[20].

The magnetic susceptibility χ of a paramagnetic system obeys Curie-Weiss law

$$\chi(T) = \frac{C}{T-\Theta} \qquad \text{with} \quad C = \frac{N\, p_{eff}^2}{3\, k_B} = \frac{N\, \mu_B^2\, g^2\, J(J+1)}{3\, k_B} \tag{2.36}$$

where Θ is the Curie-Weiss asymptotic temperature, which accounts for residual FM ($\Theta > 0$) or AFM ($\Theta < 0$) correlations in the paramagnetic state, and C is the Curie constant, from which the number N of defects can be estimated.
Notice that to evaluate the defects concentration from C, p_{eff} (or equivalently g and J) must be known. They can be measured from the field dependence of the magnetization at low temperature and in the case of graphene, as expected for a pure carbon material (only s and p orbitals), one yields within experimental errors $g = 2$, $J = 1/2$, $p_{eff} = \sqrt{3}$.

[20] However, as not all the defects give a magnetic contribution, in the experimental section we will see that another technique, Raman scattering, have been used for a parallel characterization of defects concentration.

2.4 Inelastic Neutron Scattering

Neutrons are ideal probes for the investigation of many structural and dynamical aspects of matter. They are massive, neutral particles which deeply penetrate into the sample, allowing its bulk study. In contrast with X-Rays, to which they are commonly compared, neutrons are sensible also to the light elements, but less intense beams are available and thus large samples are usually measured. Inelastic Neutron Scattering (INS) techniques, in particular, offer the possibility to study the vibrational, rotational and diffusive motions that takes place in the investigated material, depending on the energy transfer between neutrons and the sample. The analysis of the neutron scattering data recorded in graphene is still in progress and thus, within the present study, only a few qualitative results will be discussed. For this reason the following description of the technique is limited to those fundamental aspects that are relevant for the considerations advanced in next chapter and many other important characteristics are left out. For a proper introduction to Neutron Scattering the reader may refer either to standard textbooks ([140, 141]) or to the proceedings of a recent school [142].

Due to its neutral electric charge, neutron in matter essentially interact with the atomic nuclei. Since the range of the nuclear forces is much shorter than the typical neutron wavelength, the interaction can be described by a Fermi contact potential [141]

$$V(\vec{r}) \;=\; \frac{2\,\pi\,\hbar^2}{m}\,\sum_j b_j\,\delta\left(\vec{r}-\vec{R}_j\right) \tag{2.37}$$

where the summation is extended over all involved nuclei and the scattering lengths b_j account for the strength of the interaction. The values of these coefficients are characteristics of each nucleus and also depend on the nuclear spin state. We will soon come back to their significance.
By evaluating the matrix elements of the assumed potential from the incident to the final neutron states, it is possible to calculate the fundamental quantity measured in a neutron scattering experiment, the *double differential cross-section*

$$\frac{d^2\sigma}{d\Omega\,d\omega} \;=\; N\frac{k_f}{k_i}\,\left[\left(\bar{b^2}-\bar{b}^2\right)\,S_{inc}(\vec{Q},\omega)+\bar{b}^2 S_{coh}(\vec{Q},\omega)\right] \tag{2.38}$$

The multiplication of this quantity by the flux of incoming neutrons gives the number of neutrons scattered into a solid angle element $d\Omega$ with an energy transfer $\hbar\omega$. In equation (2.38), N is the number of scattering elements in the sample, k_f and k_i are the final and incident wave vectors respectively, and the coherent and incoherent scattering functions

$$S(\vec{Q},\omega) \;=\; \frac{1}{2\pi}\,\int d^3\vec{r}\,dt\,e^{i(\vec{Q}\cdot\vec{r}-\omega t)}G(\vec{r},t) \tag{2.39}$$

provide a direct link to the microscopic motions of the atoms. In particular $S_{coh}(\vec{Q},\omega)$ is the double Fourier transform in space and time of the density-density correlation function

$$G(\vec{r},t) = \frac{1}{\rho_0}\langle\rho(\vec{0},0)\,\rho(\vec{r},t)\rangle = \\ = \frac{1}{N}\langle\int d^3\vec{r'}\sum_{i,j}\delta(\vec{r}-\vec{r'}+\vec{r}_j(t))\,\delta(\vec{r'}-\vec{r}_i(0))\rangle$$

that can be interpreted as the probability density of finding at time t an atom at a distance $\vec{r}$ from the position of another atom at time 0.
Similarly the incoherent scattering function $S_{inc}(\vec{Q},\omega)$ is the double Fourier transform of the self correlation function

$$G_{self}(\vec{r},t) = \frac{1}{N}\langle\int d^3\vec{r'}\sum_{i}\delta(\vec{r}-\vec{r'}+\vec{r}_i(t))\,\delta(\vec{r'}-\vec{r}_i(0))\rangle$$

which expresses the probability density of finding an atom at time t at a distance $\vec{r}$ from its position at time 0.
These scattering functions are weighted over the scattering lengths average $b_{coh} = \bar{b}$ and variance $b_{inc} = \sqrt{\bar{b^2}-\bar{b}^2}$. When performing experiments on graphitic materials or carbon nanostructures the inelastic neutron scattering signal is dominated by the high incoherent contribution of hydrogen: its incoherent scattering length and hence its total incoherent cross section $\sigma_{inc} = 4\pi b_{inc}^2$ is an order of magnitude higher than that of carbon and other atoms (mainly oxygen) possibly present in the material (see Table 4). This consideration is the basis of the *incoherent approximation*, which assumes that $S(\vec{Q},\omega)$ can be calculated neglecting the coherent part (mainly from carbon).

Table 4. Neutron scattering cross sections of common elements in carbon-based materials. The values are in barn (1 barn = 100 fm^2).

Element	$\sigma_{coh} = 4\pi\bar{b}^2$	$\sigma_{inc} = 4\pi(\bar{b^2}-\bar{b}^2)$
C	5.551	0.001
H	1.7568	**80.26**
D	5.592	2.05
O	4.232	0.0008

2.4.1 The Phonon Density of States

The derivation of the scattering functions for the case of crystal or molecular *dynamics*, within the incoherent approximation leads to the result [140, 143]

$$S(\vec{Q},\omega) \;=\; \exp\left(-2W(\vec{Q})\right) \frac{\frac{\hbar^2 Q^2}{2mk_BT}\,\exp\left(\frac{\hbar\omega}{2k_BT}\right)}{2\frac{\hbar\omega}{k_BT}\,\sinh\left(\frac{\hbar\omega}{2k_BT}\right)}\, g(\omega)\,. \tag{2.40}$$

Equation (2.40), where W is the Debye-Waller factor, states that $S(\vec{Q},\omega)$ is proportional to the generalized phonon *density of states* $g(\omega)$ [21] and thus directly links the neutron scattering spectrum to the dynamics within the sample. Notice, however, that to get the phonon density of states a significant data treatment is necessary: the typical INS spectrum, indeed, displays the raw scattered intensity against the neutron energy loss in the sample.

2.4.2 Instrumental Setup on IN1bef

All the neutron data displayed in next chapters have been recorded on the IN1 spectrometer at Institut Laue Langevin, in Grenoble. In the configuration used, IN1BEF, this is a two-axis spectrometer with a beryllium filter added just before the detectors (fig.44). Hot neutrons are sent through a single crystal copper monochromator to select the incident energy and the beam is then focused on the sample; finally the filter stops any neutrons with an energy higher than 2.5 meV, so that only the particles that have exchanged all their energy with the sample can reach the detectors. Therefore, in this configuration, the incident energy always matches the exchanged energy $E_{in} = \Delta E$ within the filter resolution.

[21] It is equivalent to say that the scattering functions are inversely proportional the derivative of the energy dispersion curves. Indeed, in points of the reciprocal space where the dispersion curve $\omega(\vec{k})$ gets flatter (the derivative drop to lower values), more phonons are found in an energy interval $d\omega$, that is a peak in the density of states is observed; correspondingly, according to eq.(2.40), a peak is observed in the neutron spectrum.

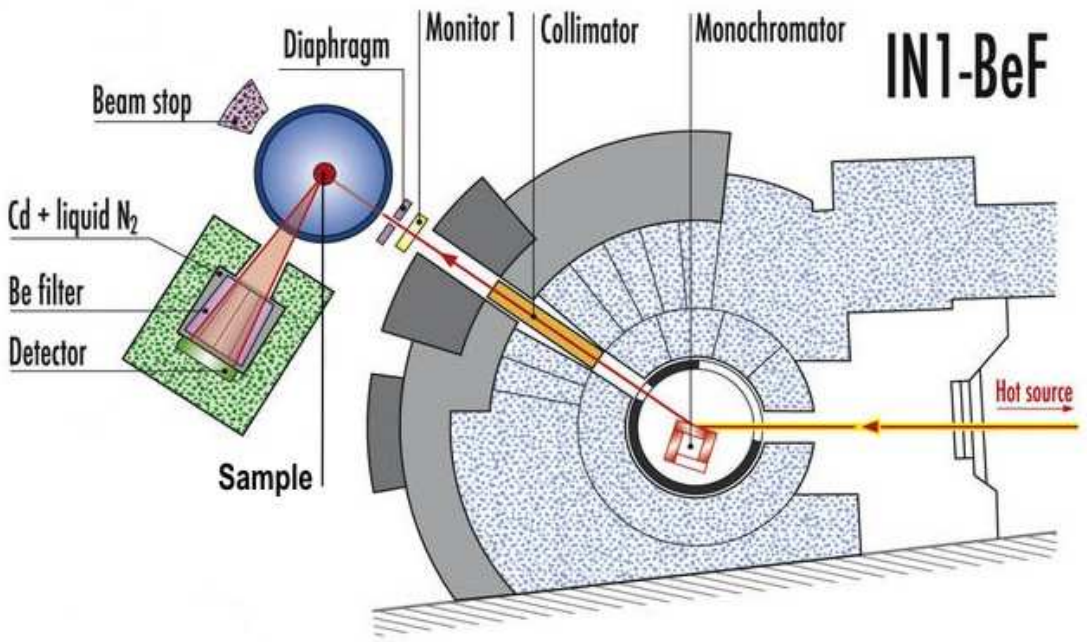

Figure 44. Instrumental setup of the IN1BEF at ILL. Adapted from the instrument official website (*http://www.ill.eu/instruments-support/instruments-groups/instruments/in1*).

Chapter 3

Chemical synthesis and Processing of Graphene

This chapter discusses the production of bulk graphene samples. This task and the more general issue of obtaining macroscopic quantities of a nanoscopic material, are of scientific interest both in the short and long term: their solution, indeed, on the one hand allows us to characterize these materials also by solid-state spectroscopies, and on the other could favour the development of future applications.

Since the discovery of graphene, during the last six years, the scientific community has developed a number of strategies either for the production of good-quality single monolayers and for the chemical synthesis of gram-scale samples. In the following we will give an overview of these methods and explain in detail the procedures used to synthesize the samples under study. A particular focus is kept on the presence of defects, as this will be relevant in the discussion of experimental results.
Besides and tightly connected to the production of graphene, some fundamental characterization techniques will be discussed. Microscopies are the natural candidates for the observation of a 2DIM nanostructured material and have been extensively applied to "see graphene-based sheets" [20]. Microscopy imaging allow to determine whether single layers are present and it is often considered an "indispensable quality control tool since it can provide immediate feedback to improve synthetic and processing strategies" [20]. Nevertheless we will show that also a bulk technique can answer these issues: in particular Neutron Scattering data has proven extremely valuable to identify the effects of the different chemical and thermal treatments performed on the samples.

3.1 Graphene Synthesis

Most of the initial investigations of graphene properties relied on **single graphene sheets** obtained by the *micromechanical cleaveage* technique, that was used to first isolate graphene in 2004 [14]. This is essentially a refined development of the idea of deriving single layers from scotch-tape peeling of graphite (a short description has already been introduced in section 1.1). Graphene soon started to be studied in view of microelectronics application and the request for a more clean and reproducible material led to the development of *epitaxial growth on silicon carbide* [144, 145]: in this method the thermal treatment of SiC at 1650°C in Argon atmosphere [146] results in the sublimation of silicon in the proximity of the surface and in a subsequent graphitization. However only recently [147] this method has yielded good quality samples.

Single sheet	Gram-scale
1. Micromechanical cleavage (scotch peeling)	1. Wet chemical methods and thermal exfoliation
2. Epitaxial growth on SiC	2. Solvothermal method
3. CVD on metal substrates	3. Arc-discharge in presence of H_2

Table 5. Main methods for the production of single graphene sheets and Gram-scale graphene samples.

Meanwhile similar efforts have allowed to optimize the growth of graphene by *chemical vapor deposition on metal surfaces*: At the beginning of 2009 three different research groups [31, 148, 149] independently demonstrated the ability to produce single layer graphene by CVD and transfer it to an arbitrary substrate. Their approach is the development of a method already used from the 70s [22] for producing multilayer graphene [150] or vertically-aligned carbon nanowalls [151, 152]: in proper conditions of high temperature (1000°C) and low pressure, the flux of a carbonaceous gas (ethylene, benzene) over a very clean metal substrate (usually Nickel[31] or Copper[153]) results in the deposition of the carbon atoms, which start to diffuse in the metal. The subsequent cooling leads the carbons to emerge at the surface and form single-layer graphene [154]. The sample quality depends on the cooling rate, on the type and concentration of the carbon gas and on the substrate thickness. The optimization of these parameters has already led to the production of very large graphenes, up to the dimensions of a flat TV panel [1]. Therefore the bottom-up approach of CVD is proving to be by far the best method for the production of single graphene sheets.

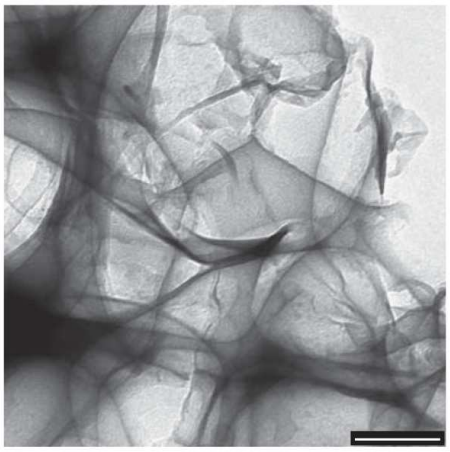

Figure 45. TEM image of a graphene sample obtained by the solvothermal method. The majority of the sample is made up of curved and fused graphene sheets. Scale bar is 200 nm. Adapted from [155].

On the other hand there is a large interest in the synthesis of **gram-scale samples of graphene**, as it is the case in the present study, in order to have enough sample for the characterization with solid-state spectroscopies like μSR and neutron scattering. There are three main methods to obtain "massive" powder samples:
the first is a bottom-up approach based on a *solvothermal reaction* [155] of sodium and ethanol (3 days in a sealed vessel at 220°C, 1:1 molar ratio). This yields a solid precursor whose subsequent flash pyrolysis generates graphene flakes, displayed in a TEM image in fig.45. These samples were the first to become available, at the end of 2008, and thus we chose them as the first set of sample for μSR investigations, starting a fruitful collaboration with the group of professor John Stride at the University of New South Wales, who developed the method.
The second, less used, approach is the extension to graphene of the *arc-discharge* method exploited for the routine production of fullerenes, where an hydrogen rather than helium atmosphere is used [94, 95]. Finally the most successful top-down approach is based on *wet chemical synthesis routes* [156]: in the most common procedure, outlined in the table opposite, pure graphite powder is oxidized by the reaction with strong acids, to yield graphite oxide (GO) [157, 158]; this material eventually undergo a partial reduction with $NaBH_4$ [159] or hydrazine [160, 161], which help to obtain a less defective graphene, and then a flash thermal treatment at 1050°C completes graphite exfoliation to a material largely composed of single-layer graphene [90]. This method has been used to produce most of the sample studied in this

Pure Graphite powder

OXIDATION

Graphite Oxide

PARTIAL REDUCTION WITH $NaBH_4$

Reduced Graphite Oxide

THERMAL EXFOLIATION AT 1050°C

Graphene

Figure 46. Pathway to the chemical synthesis of graphene. The various steps are thoroughly discussed in the following sections.

work and it is then worth describing here the different steps in detail, according to the exact preparation procedures followed.
As a closing remark, please notice that this family of wet chemical methods is often intended to include also minor different techniques [22], that are not discussed here: in particular the emerging techniques to obtain dispersion of graphene in solutions [162, 163] and the production of graphene Langmuir-Blodgett films [164].

3.1.1 Graphite Oxidation

Three methods for graphite oxidation are known since long time and, thanks to the recent interest, have been carefully optimized: the Brodie [165, 166, 157], Staudenmaier[167, 168, 161] and Hummers methods [169, 170][1]. The latter proved less efficient and have not been used for the production of graphene samples. Thus it will not be described.

Brodie oxidation

Pure graphite powder from SGL Carbon, RW-A grade, is used as a starting material (5 grams) and the oxidation process go through the following steps:

- Graphite and $KClO_3$ (49 g) are mixed and put inside a flask kept in ice bath;
- 100% nitric acid HNO_3 (30 ml) is slowly added by a dropping funnel over 2 hour; the solution is let to reach room temperature and it is stirred for several hours. (These reactions are highly exothermal and the slow addition of the acid is required to avoid explosion).
- The reaction is completed by a thermal treatment at 60°C for 8h. During this treatment ClO_2 is released in gas form.
- The solution is then diluted into water, filtered, washed in HCl (3 M).
- It is finally rinsed with water until a pH value of $\simeq 6$ is reached. The obtained *green* graphite powder is then dried at 60°C.

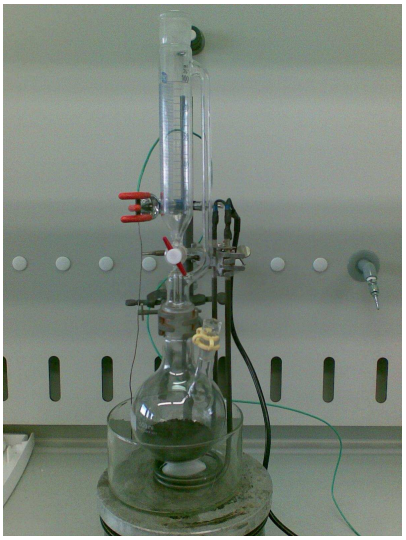

Figure 47. A picture taken during the preparation of Graphite Oxide.

[1]For each oxidation method a few references are given in chronological order: the first is to the original article, the following ones to more recent modifications of the method

Staudenmaier oxidation

This method, which uses also sulfuric acid in addition to nitric acid, can be seen as a variation of Brodie method, except that the order of the main operations is shuffled, as graphite is first mixed to the acids and the salt is then slowly added during the reaction. In particular:

- Concentrated H_2SO_4 and HNO_3 (2:1 in volume) are mixed inside a flask kept in ice bath;
- Graphite powder is added (3.5 g for 100 ml of H_2SO_4);
- $KClO_3$ (50 g) is gradually added over 2 days and the reaction continues under stirring at room temperature up to a total of 4 days.
- The solution is diluted into water, filtered, washed in HCl (5%) and filtered again.
- The obtained *brown* powder of graphite oxide is washed with water several times until $pH \simeq 7$ and then dried at 60°C.
- The sample is finally annealed above 100°C to get rid of intercalated water.

Graphite Oxide

The product of these oxidation procedures, known as graphite oxide, is an expanded, functionalized graphite, which structure is represented in fig.48. Graphite oxidation, indeed, leads to the bonding of many functional groups (hydroxide, peroxide, epoxy and carboxyl moieties) to the graphite planes [156]. As a consequence GO is hydrophilic, unlike the hydrophobic parent graphite, and the stacking distance among its planes is noticeably increased.

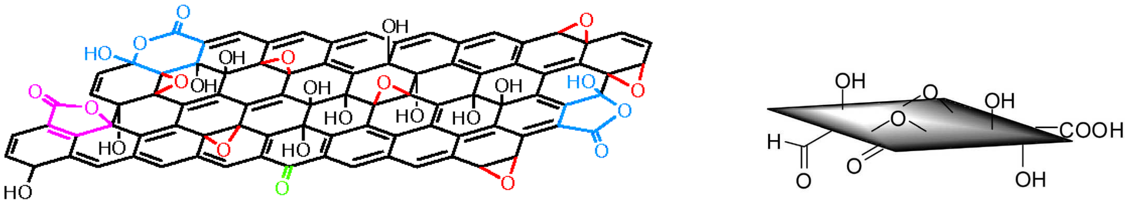

(a). Adapted from [159]. **(b).** Adapted from [161].

Figure 48. Schematic representations of Graphite Oxide.

Laboratory XRays diffraction spectra, displayed in fig.49, show the (002) reflection is rather left-shifted down to a lower angle, corresponding to an interplane distance which is almost doubled. These result confirm previous XRD studies present in the literature [158]. In addition GO has been structurally characterized by a number of

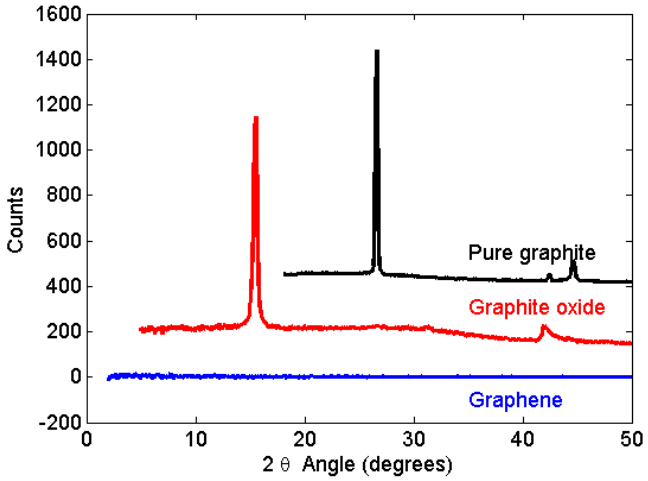

Figure 49. Laboratory X-Ray diffraction spectra for the starting graphite, graphite oxide and exfoliated graphite oxide. The spectra are vertically sifted for clarity.

techniques, including XPS [171, 172], NMR [173], Raman Spectroscopy [174], Electron microscopy and diffraction [158]. These studies all contributed to get a clear picture of the types and arrangement of the functional groups.

3.1.2 Thermal Exfoliation

Sudden heating of GO to 1050°C forces these groups to detach from the plane, generating an overpressure, mainly of CO_2 and CO, that separates the graphene layers. This exfoliation *increase the sample volume by more than 1000 times*, as it is apparent in the pictures below. It yields a dark grey material made of soft, expanded, "floating" graphene flakes, with a very low density. Its characterization, introduced below, proved that a consistent part of the sample is made out of single layer graphene.
Notice that the formation of CO_2 and CO have been mentioned, implying that when the functional groups are disrupted from the plane, most of the times they bring away the carbon atom they were attached to. Thus *samples obtained from thermal exfoliation are rich in defects* and especially in carbon vacancies. These may either remain paramagnetic or be saturated by the hydrogen freed during the exfoliation process.
For the implementation of this thermal treatment, the sample is placed in a large quartz vial, which is evacuated below $10^{-4}\,mbar$. The vial, in static vacuum conditions, is rapidly inserted into a tube furnace, preheated at 1050°C, to obtain a heating rate of almost 2000°C/min [22]. The system is kept 1 minute at high temperature and is then taken out from the oven and left to thermalize at room temperature.

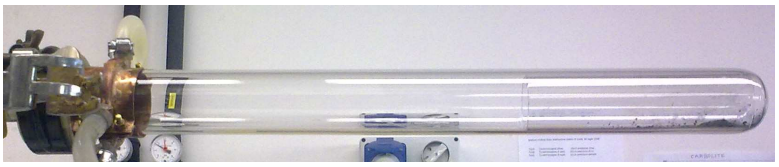

(a). The GO powder is loaded inside a vial for the thermal exfoliation treatment.

(b). The expansion of graphite to graphene leads to a huge increase in volume.

Figure 50. Pictures taken (a) before and (b) after thermal exfoliation.

Three additional remarks:

- The main exfoliation reaction and expansion happen within the first few seconds. One minute is the time expected to be long enough to warranty that all regions of the sample reach the maximum temperature and are then properly exfoliated (even the part of sample that is moved far away from the oven center by the initial reaction), but short enough to avoid annealing effects. However the time parameter may be further optimized.

- At the end of the thermal treatments the vial is evacuated from the excess gas formed (approximately 200 mbar) and then opened inside a Argon glove box. From this moment on, graphene samples are never exposed to air, neither for storing and handling, nor for further treatments or for μSR experiments. In this way unsaturated defects and dangling bonds are retained and can be characterized.

- The experimental feasibility of this treatment required special care towards security and the construction of several specifically-designed items, including: a proper water cooling system and a trolley, constrained to railings, which hold the sample vial to be sure it can enter/exit smoothly in the furnace (to have the maximum sample chamber volume the vial is chosen with a diameter which just fits the furnace).

3.1.3 Partial Reduction of Graphite Oxide

We have evidenced that the thermal exfoliation of GO generate highly defective graphene planes. If interested in a more clean material, a step of partial reduction can be introduced before the exfoliation: this process "repairs" the planes, by decreasing the number of adsorbed functional groups and thus the vacancies concentration in the final graphene sample. On the other hand, the strongest the reduction the less effective will result the exfoliation process, because if only a few adsorbed molecules are present, a lower pressure is generated among the planes.

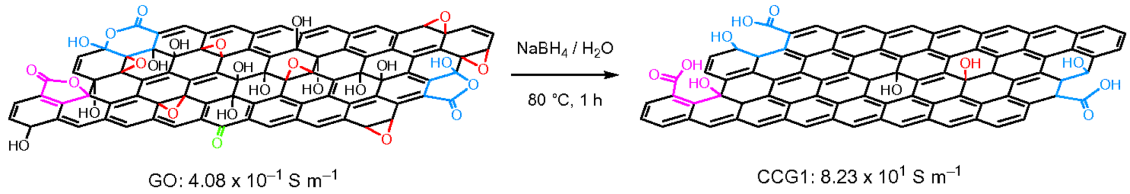

Figure 51. Schematic representation of the structure of GO and reduced GO. A lower concentration of adsorbed molecules and a larger stacking distance characterize the reduced GO. Adapted from [159].

An effective partial reduction can be obtained by reaction either with hydrazine [160, 161] (but this compound is seldom used because it is toxic and explosive) or with sodium borohydride $NaBH_4$, which has been used within this study.
For this reaction GO powder (1 g) is dispersed into water by sonication and a solution of $NaBH_4$ (6 g over 100 ml of water) is slowly added by a dropping funnel, under ultrasound sonication. Then to optimize the reaction conditions the pH value is corrected to 10 by adding a water solution of $NaCO_3$ (5% in weight). The sample then undergo a thermal treatment at 80°C for a few hours and is cooled down under stirring and sonication. Finally the resulting suspension is filtered, rinsed with water and dried at 60°C.

Recently also other compounds have been used as reducing agents for GO, including $NaHSO_3$ [175] and hydriodic and acetic acid [176] and, noticeably, it has been proposed to move the reduction step after the thermal exfoliation [176, 22].

Further treatment in H_2SO_4

In order to gain a control of the defects concentration in the samples, a further cleanup of the material in sulfuric acid have been considered. As shown in figure 52 this treatment has proven effective in removing residual functional groups from the GO planes [159]. Reduced GO is suspended in H_2SO_4 and undergo a thermal treatment at 120°C for 6 h, under stirring. Then the suspension is left to cool down and settle, and it is finally rinsed and filtered with water.

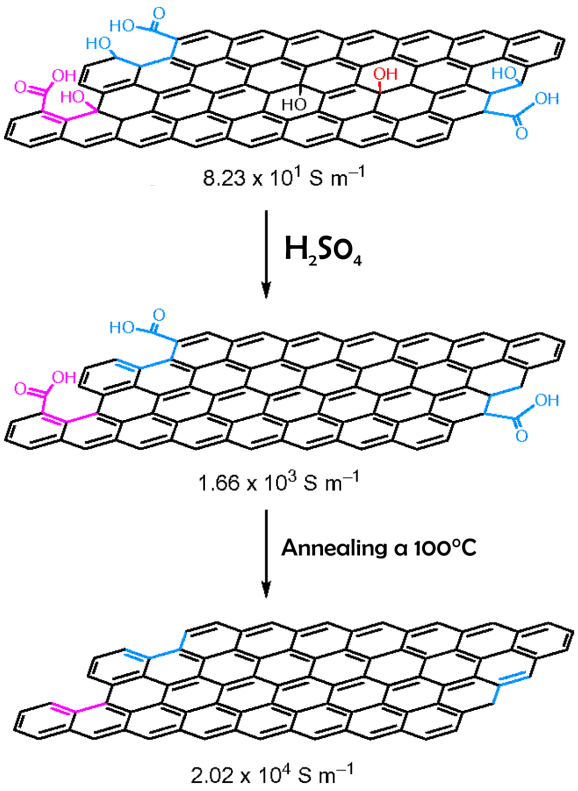

Figure 52. Schematic representation of the structural evolution of reduced GO under the treatment in sulfuric acid.

In summary three types of differently-prepared samples have been considered for characterization: graphene obtained from the solvothermal method, prepared by the group of prof.Stride (method **1**), and two chemically synthesized graphenes, derived by thermal exfoliation of GO with (method **2**) or without (method **3**) the reduction step. For the reduced samples a mild exfoliation at lower temperature has been used and hence these systems are more compact than the properly exfoliated ones. The preparation procedures are summarized in table 6.

<table>
<tr><th>Method 1</th><th>Method 2</th><th>Method 3</th></tr>
<tr><td colspan="3">Pure Graphite Powder (RW-A grade)</td></tr>
<tr><td rowspan="3">Pyrolisis of Na and Ethanol (Solvothermal Method)</td><td>Graphite Oxidation (Staudenmaier met.)</td><td>Graphite Oxidation (Brodie method)</td></tr>
<tr><td>Partial reduction with $NaBH_4$</td><td rowspan="2">Exfoliation at 1050°C</td></tr>
<tr><td>Exfoliation at 400°C</td></tr>
<tr><td>Highly defective graphene</td><td>Moderately defective graphene</td><td>Highly defective graphene</td></tr>
</table>

Table 6. Summary of the preparation procedures followed for the production of gram-scale graphene.

3.2 Morphological Characterization

The samples have been characterized first with respect to their morphology, by Transmission and Scanning Electron Microscopy and Electron Diffraction[2]. These are among the most common techniques used for graphene structural analysis. In addition we have already shown x-ray diffraction data and we will discuss in next chapter the investigation by another technique often applied to graphenes, Raman spectroscopy, which helped to identify the defects concentration in the samples. The techniques commonly used for graphene structural studies are gathered in fig.53 and were already mentioned in section 1.1.

Figure 45 above (page 71) shows a TEM image of samples obtained from method **1**, which entirely consist of fused graphene sheets forming a weak porous network. Their full characterization as already been published in [155], where evidence for the presence of single layers are given. The samples produced by exfoliation of GO have a quite different morphology. Their SEM and TEM images are shown in figure 54, for a sample of type **2** on the left and of type **3** on the right, respectively. The former appears as the aggregation of thick plates, each consisting of overlapping thin sheets, stacked in random orientations. The free sheet at the center of fig.54a is approximately $1\,\mu m \times 1\,\mu m$ in size and, though its thickness cannot be measured by SEM, it is thin

[2]These morphological characterization were performed at the University of New South Wales by our collaborators Mohammad Choucair and John Stride.

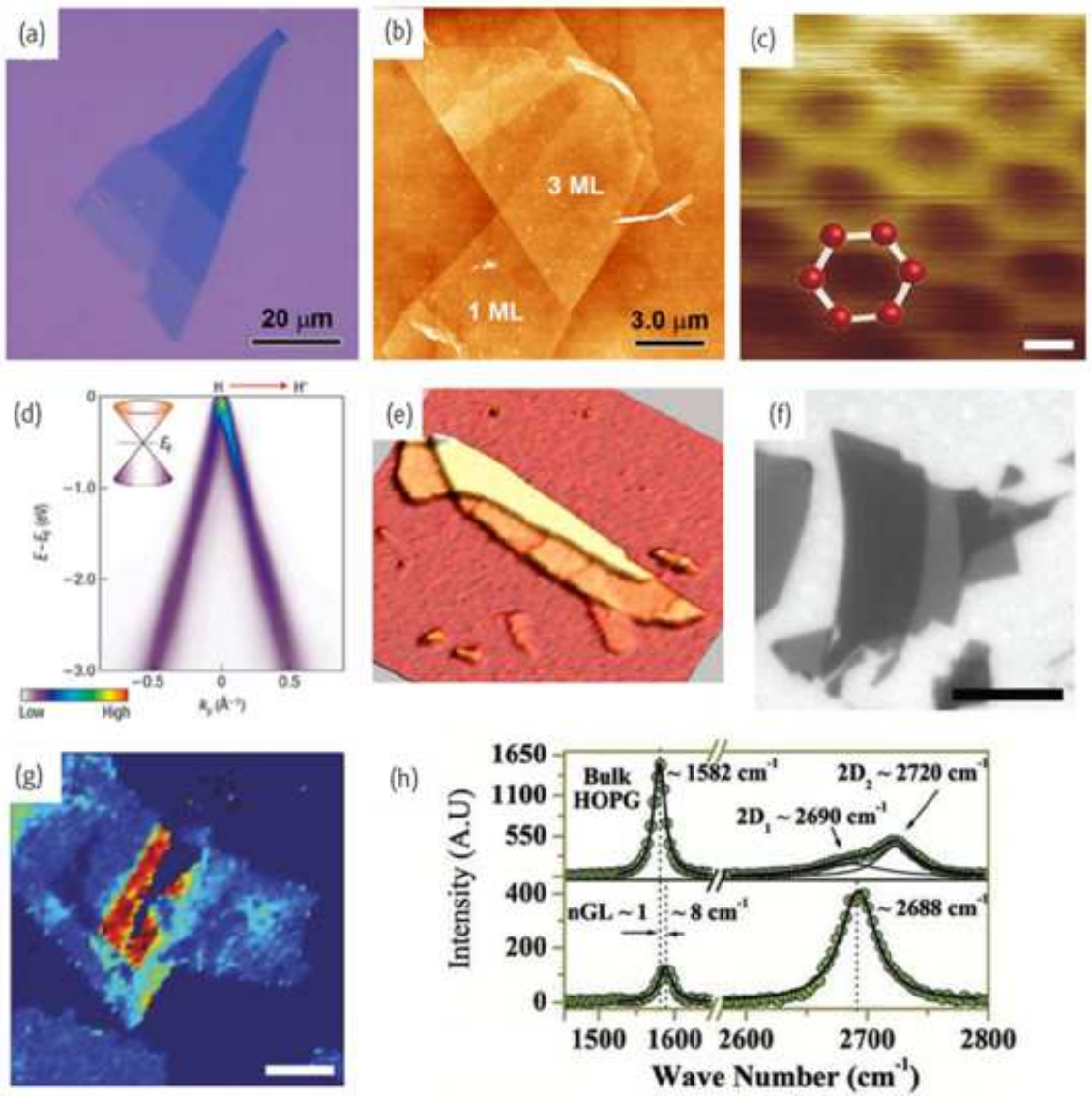

Figure 53. Major techniques for graphene characterization. **a.** Optical Microscopy, **b.** Atomic Force Microscopy, **c.** Scanning Tunneling Microscopy (scale bar 0.1 nm), **d.** Angle-resolved photoemission spectroscopy (ARPES), **e.** Rayleigh scattering, **f.** Fluorescence Quenching Microscopy (scale bar 10 μm). **g.** Raman Imaging (scale bar 3 μm), **h.** Raman Spectroscopy. Adapted from [22, 20, 177].

enough to be almost fully transparent under the beam. High-temperature exfoliated samples, instead, consist of flakes with a porous, layered structure where many single graphene sheets overlap and fuse together, as is apparent in figure 54b. The TEM images in both cases highlight the presence of an high concentration of single layer graphene sheets, with evident folding and crumpling in fig.54c.

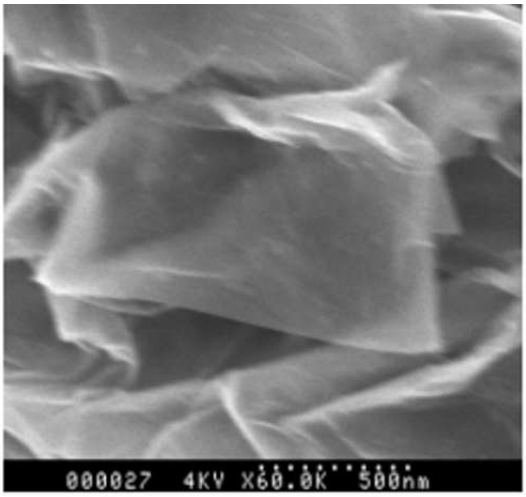

(a). SEM image of a sample of type (2).

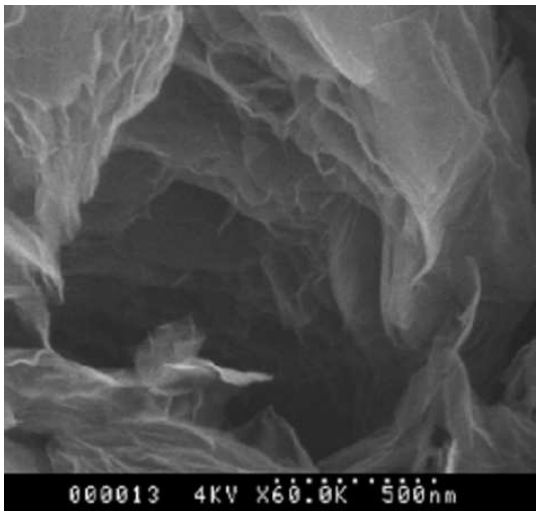

(b). SEM image of a sample of type (3).

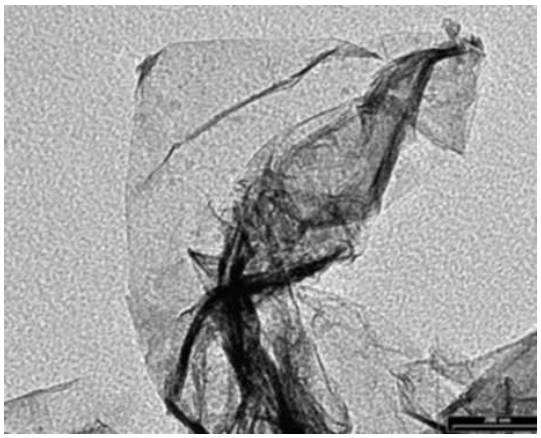

(c). TEM image from a region in a sample of type (2). The graphene sheet shows an evident folding and a crumpled-like appearance. Scale bar indicates 200 nm.

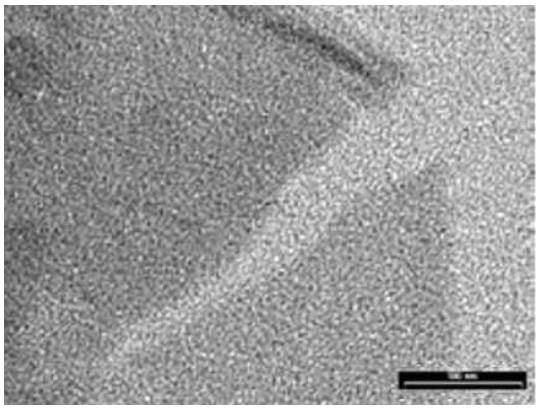

(d). TEM image from a region in a sample of type (2). A single layer sheet is shown with a prominent tear and crumpling at the edge. Scale bar indicates 100 nm.

Figure 54. Scanning and Transmission Electron Microscopy images from regions in samples prepared according to method (2) on the left and to method (3) on the right.

3.3 Reduction treatments "seen" by Inelastic Neutron Scattering

To conclude our discussion about the synthesis of graphene it is useful to look at the inelastic neutron scattering data we have recently recorded with the IN1BEF spectrometer at Institut Laue Langevin, in collaboration with Dr.Stéphane Rols (ILL). This experiment proposed to identify the dynamical features of graphene observable by INS, in comparison to that of graphite, in order to evidence the possible contributions of ripples (in the quasi-elastic region) and of in-plane and edge defects. In principle neutron scattering should be able even to sort out the contributions from different types of defects, on the basis of the different nature of their vibrational dynamics (localized for vacancies, collective for edges). The data analysis is still in progress and here we will limit to discuss some qualitative results which provided useful feedbacks on the preparation procedures.

Figure 55 displays the normalized neutron spectra for graphene samples prepared from direct exfoliation of GO (method **3**, black data points), with the inclusion of the reduction step (method **2**, red) and with the further treatment in sulfuric acid (yellow). In addition data taken on a graphene sample treated at high temperature in hydrogen are shown (we will come back to this blue curve soon).

Please now recall a consideration made in the introduction to neutron scattering: when performing experiments on graphitic materials or carbon nanostructures, the inelastic neutron scattering signal is dominated by the high incoherent contribution of hydrogen. With this statement in mind, it can be easily observed that neutron scattered intensities reflects the expected composition of the different samples, prospected in the structural models above, and hence *confirm the effectiveness of the reduction treatments*. In particular the background intensity of the highly defective as-prepared graphene is large, due to the residual groups attached to the plane and to the hydrogen impurities which may have saturated the paramagnetic electrons located at carbon vacancies; the reduction step, by lowering the concentrations of the adsorbed species, also strongly reduce the final hydrogen content in the sample, yielding a weaker signal; the intensity is further reduced in case the treatment in H_2SO_4 is applied, as it is consistent with the clean carbon planes expected in this system(fig.52).

In the two latter samples, the spectra are comparable to the ones of graphite and carbon nanotubes: this observation evidence that, in these cases, the coherent *carbon* signal is the main contribution and thus the samples have a rather low hydrogen content.

On the contrary, the signal is strongly enhanced for the sample exposed to hydrogen. For μSR investigations a whole set of "hydrogenated" graphene samples were prepared

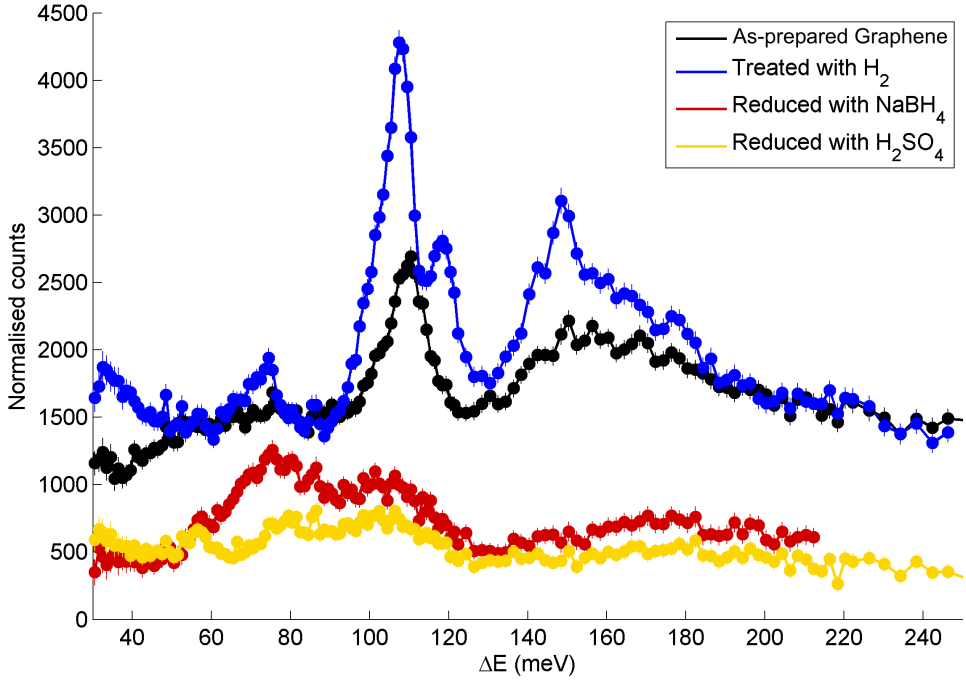

Figure 55. Inelastic neutron scattering spectra for different graphene samples. An higher intensity corresponds to a higher concentration of hydrogen in the sample.

and characterized: they were obtained by thermal treatment of different as-prepared graphenes in an hydrogen flux of 100 ml/min for 1h30'. The treatment temperature was varied from 600 to 1000°C and the optimal value turned out to be 800°C (see section 5.1). The increased intensity of the neutron scattering signal confirms that the considered thermal treatments are effective in hydrogenating the samples. The full characterization of hydrogenated species is the main topic of chapter 5, where a discussion of neutron data can also be found.

Chapter 4

The role of Defects in Graphene: a μSR investigation

In many areas of materials science, from crystal growth to mechanical applications, from transport properties to semiconductor devices, defects often play a significant role. Graphene makes no exception, as we have seen discussing the possible magnetic phases triggered by defects (section 1.8). Stimulated by these theoretical previsions [10, 89], in the following we study how the different types of defects influence graphene properties. In particular we show and discuss the major results of the first μSR investigation ever performed in graphene. It will become apparent that the observed interactions are strongly linked to the presence of *defects*, even beyond their relation to magnetism.

4.1 Edges States and Ball-Milled Graphite

At the beginning of this project, while developing the methods for the synthesis of graphene, the study of defects already started from the investigation of *edge states* in mechanically ball-milled graphite (BMG). This material is mainly made of nanometre-sized crystallites and it is then particularly suitable for edge studies.
After a preliminary vacuum annealing at high temperatures ($\geqslant$ 800°C), known to remove oxygen and moisture contamination [45][1], graphite powder is processed by mechanical ball-milling in strictly oxygen and moisture free Ar atmosphere ($\leqslant$ 1 ppm O_2, $\leqslant$ 1 ppm H_2O). This mechanical treatment induces several structural deformations, well described in the literature [178, 179]: with increasing milling time turbostratic disorder, planes cleavage, planes breaking and reduction of crystal grain size are observed, until sp^3 hybridization develop in small group of atoms and the material gradually get

[1] These treatments, however, keep the hydrogen saturation of dangling bonds at the edges.

amorphous. Xray diffraction (fig.56a) helped to optimize milling time[2] in order to avoid the latter transformation and obtain small graphite grains (known in the literature as *nanographites*), with a strongly increased volume fraction of graphene edges and in plane defects (mainly vacancies). Raman [180] and TEM investigations (fig.56) confirmed the produced ball-milled graphite is composed by exfoliated graphene sheets and elongated nanographites with an average thickness of 6 nm.

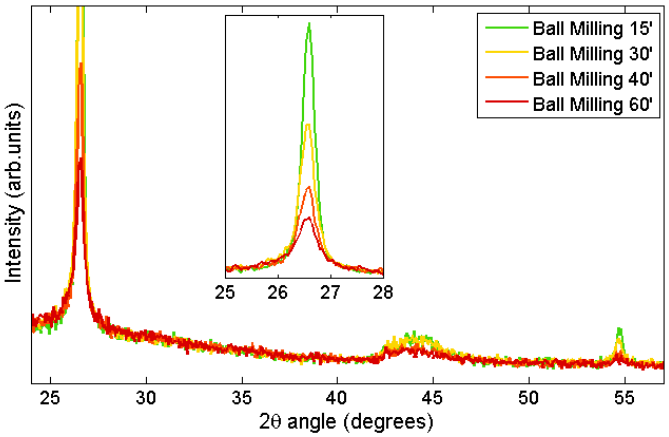

(a). Laboratory X-Ray diffraction spectra of BMG for increasing milling time. On the left the peak related to the (002) reflection is zoomed.

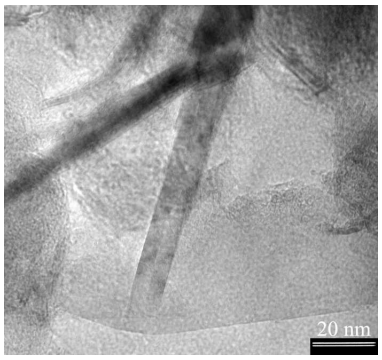

(b). TEM images of Ball-Milled Graphite. Nanographites and exfoliated graphene sheets are observed in the samples.

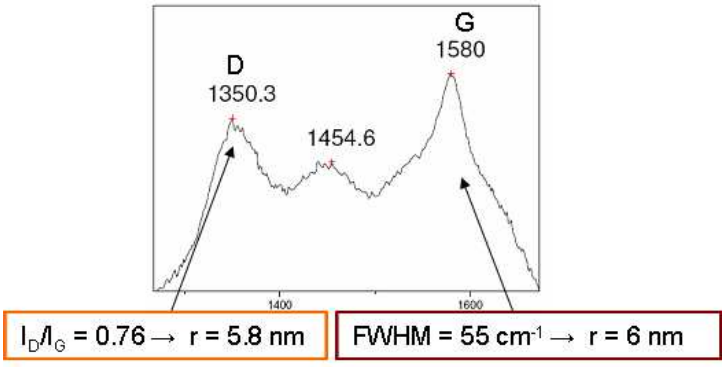

(c). Central region of the Raman spectra of BMG. The I_D/I_G ratio and the width of the G band give two independent measures of crystallites size.

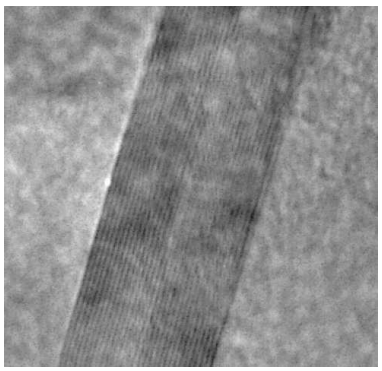

(d). Explosion of the side view of a nanographite, which evidences its structure composed of approx. 30 graphene planes.

Figure 56. Structural characterization of BMG.

[2]We employed a Fritsch ball-milling system, equipped with an agate jar (3 cm in diam.) and 3 agate balls: the optimal time in this configuration is 1 h at 50 Hz (separated in session of 10 minutes to avoid overheating).

The zero field μSR characterization of BMG (fig.57) has shown three different contributions:

1. the majority of the muons retains almost the full polarization, following their well-known behaviour in standard graphite, described in detail by Cox [181];

2. a second fraction (20%) displays a slow **lorentzian depolarization**, with a relaxation rate which vary slightly from sample to sample around an average value $\lambda = 0.25 \pm 0.06\,\mu s^{-1}$ at 5 K and decreases with increasing temperature down to $\lambda = 0.15 \pm 0.04\,\mu s^{-1}$ at 300 K;

3. a small missing fraction (10%).

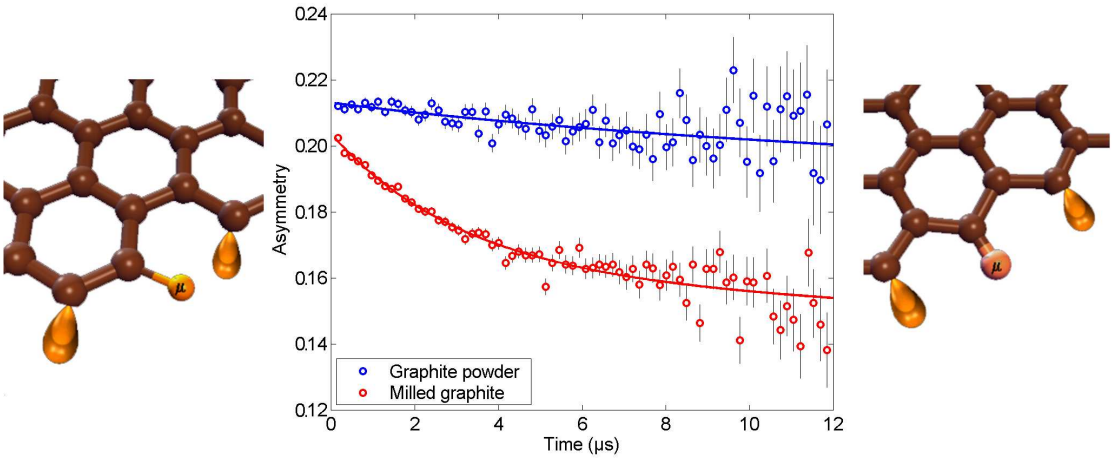

Figure 57. ZF μSR measurements in BMG at 5 K. Contrary to the case of graphite, a slow lorentzian depolarization and a small missing fraction are observed. The latter is supposed to arise from the muon interactions at *armchair* edges (left), while the relaxing contribution is attributed to *zigzag* edges (right).

Although no definitive conclusions have been reached, contributions (2) and (3) are found to be consistent with the following hypotheses: the lorentzian depolarization may derive from muonium binding at the *zigzag* edges, where it is affected by the paramagnetic electrons of nearby dangling bonds. A simple model, where each zigzag site near the muon host a paramagnetic electron randomly fluctuating on a sphere and thus generating an average dipolar field $\bar{H}_{dip}$, has been numerically implemented and the resulting relaxation rate is found to be[3] $\lambda = \sum \omega_\mu^2(i)\,\tau = \sum \left(\gamma_\mu \bar{H}_{dip}(i)\right)^2 \tau = 0.32\,\mu s^{-1}$,

[3]Here the characteristic time of electron fluctuations τ is an experimental parameter, derived form the observation that these fluctuations frezees at $1.6\,K$, where the relaxation start to follow a Gaussian rather than Lorentzian form.

in good agreement with experimental data. The analog influence of paramagnetic electrons along the armchair edges can be excluded, because the different geometry would induce a quite higher relaxation rate.
The missing fraction contribution, instead, can be tentatively attributed to the formation of a muonated *radical species at armchair edges*. Preliminary repolarization experiments in LF, indeed, seems to indicate an hyperfine interaction of $\simeq 350$ MHz[4]: this is compatible with the σ electrons at armchair edges, since their electronic configuration is similar to several organic compounds where typical frequencies of some hundreds MHz are measured [114].

4.2 μSR investigation of Graphene

We now turn to the "heart" of the present research, the μSR studies of chemically synthesized graphene. The investigated samples can be divided into 3 groups, corresponding to the 3 synthesis methods adopted (table 6). For convenience they are listed again in the following table:

	Group of Samples studied
1	Solvothermal Graphene
2	Exfoliation of Reduced GO
3	Exfoliation of GO

Table 7. The three different groups of samples characterized by μSR.

In addition a few single samples with slightly different preparation have been considered, including a sample which underwent a treatment in H_2SO_4 (see paragraph 3.1.3).

Apart from a constant background from muons stopped in the sample holder, two main contributions are observed in ZF μSR data, *independently of sample preparation* (20 different samples were investigated):

- A *Lorentzian relaxation* of polarization, experienced by a large fraction of the muons, most probably due to the isolated paramagnetic electrons located at unsaturated defects sites. This signal is analogue to the one already observed in BMG, but the relaxation rate is almost one order of magnitude lower.

[4]The considered missing fraction is really small and more accurate experiments are needed. Therefore this result should be taken with extreme care.

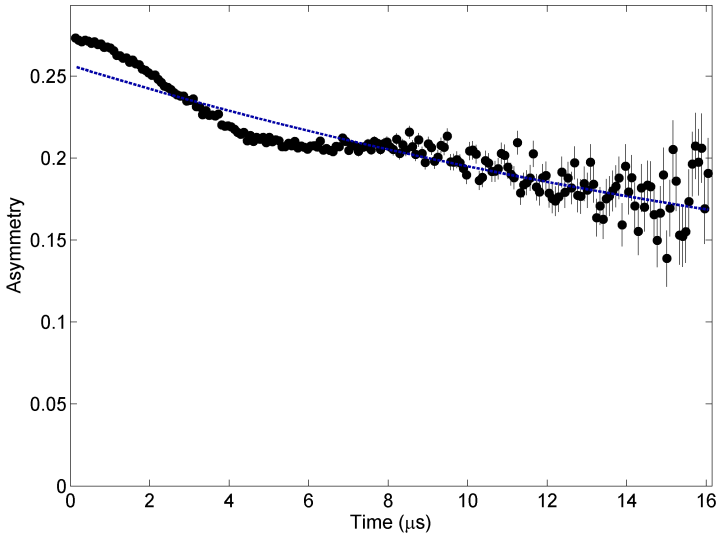

Figure 58. ZF μSR data for a sample of group **1**. The dashed line display the relaxation contribution (from the fit in next figure), in order to evidence the oscillating component.

- A *damped oscillation*, fingerprint of the muon spin precession around a local magnetic field (of the order of a few Gauss);

The striking observation of muon spin precession in graphene is of great interest, especially as it occurs in a 2DIM material and because it opens relevant discussions on the possibly related physical properties.
The model function that describes the muon polarization will be in the form

$$P(t) = A_{bg} + A_1 e^{-\lambda t} + A_2 P_{osc}(t) \tag{4.1}$$

where the first two terms account for the contributions of the silver sample holder [5] and of the lorentzian relaxation respectively. To explain the origin of the observed precession, two different physical interpretations, which demonstrated to fit the experimental data, can be considered:

Long range magnetic order

The rise of an ordered magnetic phase in the sample, either of ferro- or antiferromagnetic type.

μ-H dipolar interaction

The dipolar interaction between the muon and an hydrogen nucleus, similarly to what is observed in the F-μ-F configuration [127] (section 2.2.3).

[5] Muon polarization in silver is essentially constant. It shows only a tiny lorentzian relaxation rate, which was actually included in the fit.

In the following we thoroughly analyze these two hypotheses and show that both are fully consistent with the data. The discussion will allow important insights into the physics of graphene. First the "magnetic interpretation" is developed and the role of defects is discussed; then the "μ-H hypothesis" is introduced and, with the analysis of hydrogenated samples at the beginning of next chapter, the main focus shift to the interaction among graphene and the hydrogen atom. Finally the results of a specifically designed experiment will solve the ambiguity and some more advanced considerations will be possible.

An important notice: since the mathematical equations that describes the muon polarization are quite different in the two models, any value obtained (even for the lorentzian part) and any subsequent consideration hold valid only within the corresponding hypothesis.

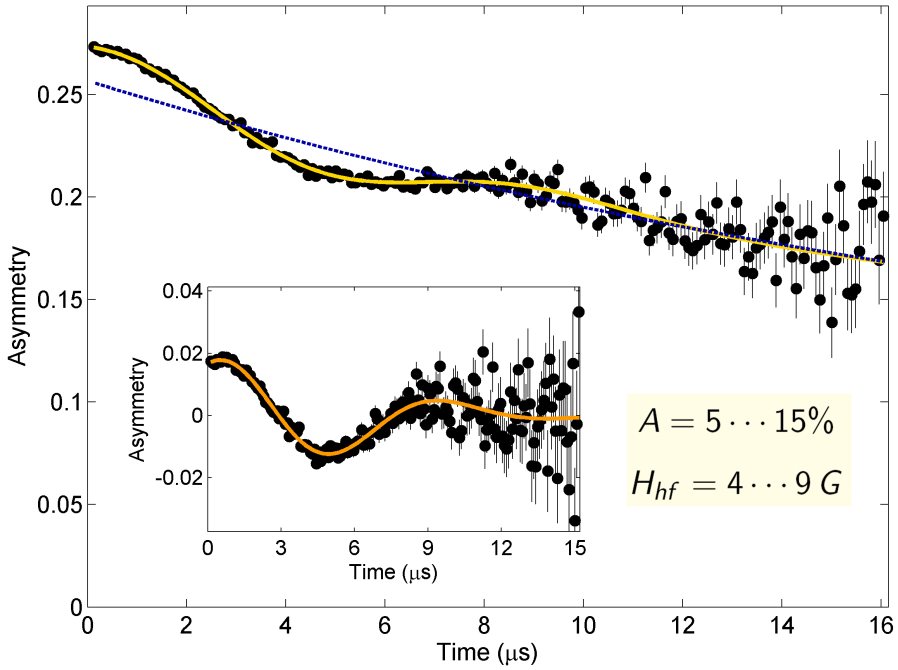

Figure 59. Best fit (yellow solid line) of ZF μSR data for a sample of group **1**, in the hypothesis of magnetic order (eq.4.2). The inset display the only oscillating contribution. The involved volume fraction A and precession field H_{hf} vary slightly form sample to sample in the specified ranges (see text).

4.3 The hypothesis of long range magnetic order

In the first model it is assumed that an ordered magnetic phase is present in (some regions of) the sample. The oscillating signal observed is then attributed to the Larmor precession of the muon spin around the internal field of the magnet H_{hf} and is described by a single gaussian-damped harmonic wave

$$P_{osc}(t) = \frac{1}{3} + \frac{2}{3}\cos(\gamma H_{hf} t)\exp\left(-\sigma^2 t^2\right) \tag{4.2}$$

A representative fit of eq.(4.2) to experimental data is shown in figure 59. In this model all the samples from groups **1-3** follow the same behaviour, with frequencies and amplitudes varying slightly from sample to sample, respectively in the ranges $H_{hf} = 4 \cdots 9\,G$ and $A = 5 \cdots 15\%$ (in volume fraction). The limited volume fraction is probably due to the fact that the magnetic phase can form only where the defects concentration is high enough and, most importantly, where the material is exfoliated to single layers.

4.3.1 At the origin of Magnetism: defects

Based on the theoretical predictions of defect-induced magnetism (see section 1.8), we performed Raman spectroscopy and SQUID susceptibility measurements on our samples. Both techniques are indeed indicative of the defects concentration in the samples: in magnetometry, since graphene has a diamagnetic response, the paramagnetic contribution observed in the temperature dependence of magnetization provide a quantitative estimation of defects concentration. Both unsaturated and saturated vacancies, as well as chemisorbed hydrogen, are known to bring a magnetic moment (see section 2.3.1). Regarding Raman spectroscopy, instead, this display a G band ($1580 - 1590\ cm^{-1}$), corresponding to the hexagonal order and a D band ($1450 - 1500\ cm^{-1}$), with contributions from defects and edges [18]. Hence the I_D/I_G ratio of the integrated intensities of the two peaks is relative indication of the total amount of defects.

Despite SQUID measures only the paramagnetic fraction of the defects, the estimations made by the two techniques agree well (fig.61a). The high correlation observed between the defects concentration and the μSR precession signal amplitude (panel b) and frequency (panel c) is a strong suggestion that the observed magnetism should be traced back to the presence of defects in graphene.

Some considerations about the type of defects involved can also be advanced. Within each group of samples (except the first), different graphite powders were taken into consideration as a starting material: most of the samples are made from graphite

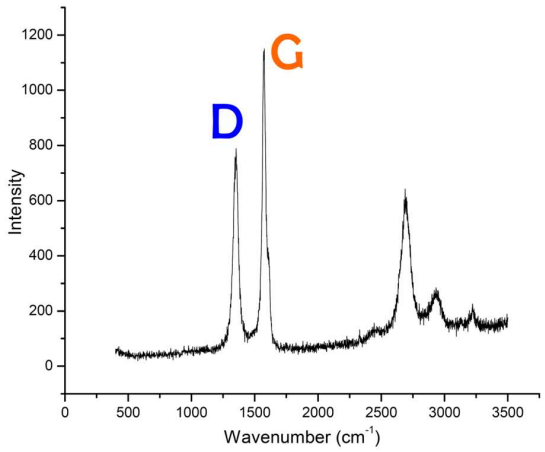

(a). Typical Raman spectrum from a graphene sample.

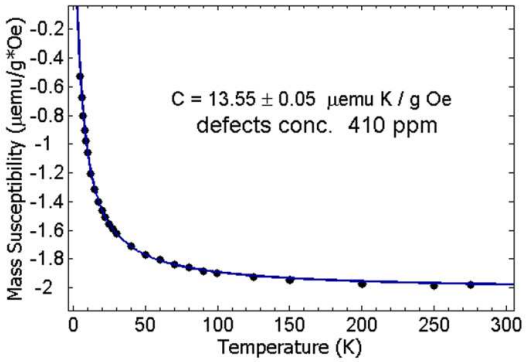

(b). Temperature dependence of magnetic susceptibility for a graphene sample in a field of 5kOe. The solid line is the Curie-Weiss best fit to experimental data (black points).

Figure 60. Techniques for the characterization of Defects concentration.

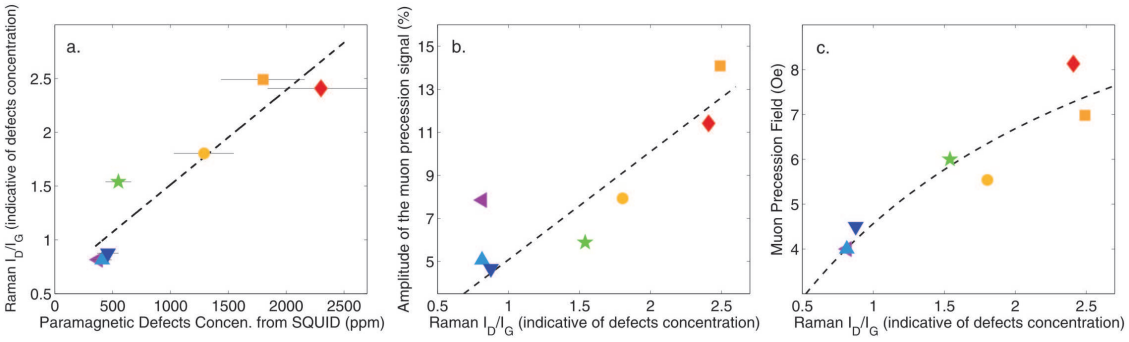

Figure 61. **a.**Correlation between the amplitude of SQUID paramagnetic susceptibility and Raman I_D/I_G ratio. Both quantities are indicative of defects concentration in graphene. **b-c.** The dependence of the muon precession amplitude and frequency from the Raman I_D/I_G suggests that defects could be the origin of the observed magnetism. While the dashed lines are intended just to evidence the presence of correlation in **a** and **b**, in panel **c** a logarithmic correlation is displayed, in agreement with the theoretical predictions (see next section).

powder with an average grain size of 66 μm, but a part of the samples were made from a graphite with smaller mesh (1.5 μm) and from ball-milled graphite. However, within experimental errors, no differences have been found among these samples. This result suggest that mainly carbon vacancies and chemisorbed species (H,OH) contribute to the formation of the magnetic phase, since edges seem not to play a major role.

4.3.2 Comparison to theoretical results

As discussed in section 1.8, theoretical studies have shown both single atom vacancies and chemisorbed hydrogens induce a net spin polarization on the neighbouring atoms. When the density of this defects is large enough, magnetism appears [10]. On this basis, our collaborator prof. Oleg Yazyev has implemented first-principles calculations on a defective honeycomb lattice, using the spin-polarized Density Functional Theory (GGA) scheme implemented in the SIESTA code [182, 183]. The calculated *hyperfine interaction* between the defect states and the muon spin follow a logarithmic behaviour as a function of the defects concentration x

$$\begin{aligned} A_{loc} &= \left[\ln\left(a + \frac{b}{x}\right)\right]^{-1} \\ a &= 1.0078G^{-1} \quad b = 4.75 \cdot 10^{-5} \end{aligned} \tag{4.3}$$

For the defects concentration estimated in our samples (a few hundred ppm) the theoretical expectations match the measured values of the local field ($4 \cdots 8$ Oe).

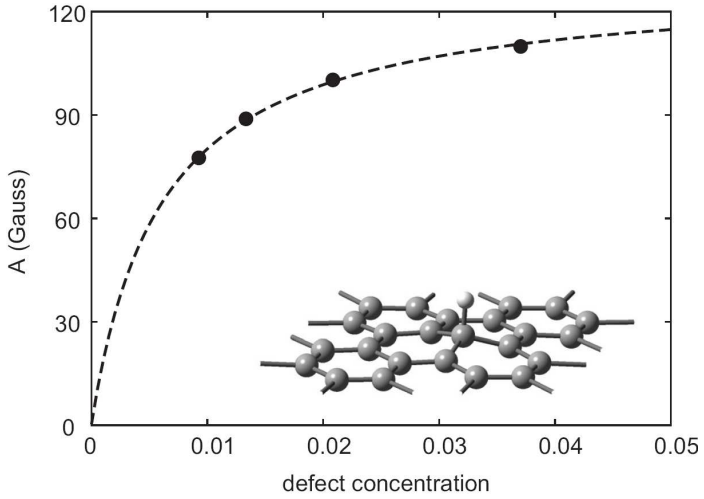

Figure 62. Theoretically expected dependence of the Hyperfine interaction H_{hf} (local field on the muon, in G) on defects concentration.

4.3.3 Nature of the magnetic interactions

Once it is clear if the observed precession is a signature of the presence of long range magnetic order, the question of whether it is of ferromagnetic (FM) or antiferromagnetic (AFM) character emerges. ZF μSR is unable to distinguish between the two cases as it probes the magnetization locally. However, the application of a longitudinal external field can help to clarify this issue.

Figure 63 shows the field dependence of the observed precession field at room temperature (in the same sample of the data shown above). The dashed line represents the expected dependence if the local field H_{hf} is considered insensitive to the external field, behaviour which is generally expected in the case of AFM order. The total field is then evaluated as the simple vector sum $\vec{H}_{tot} = \vec{H}_{ext} + \vec{H}_{hf}(0)$, averaged over all the possible powder orientations. On the contrary, in the case of FM ordering below saturation, the internal magnetization is expected to partially screen the external field, even in the 2DIM case [184].

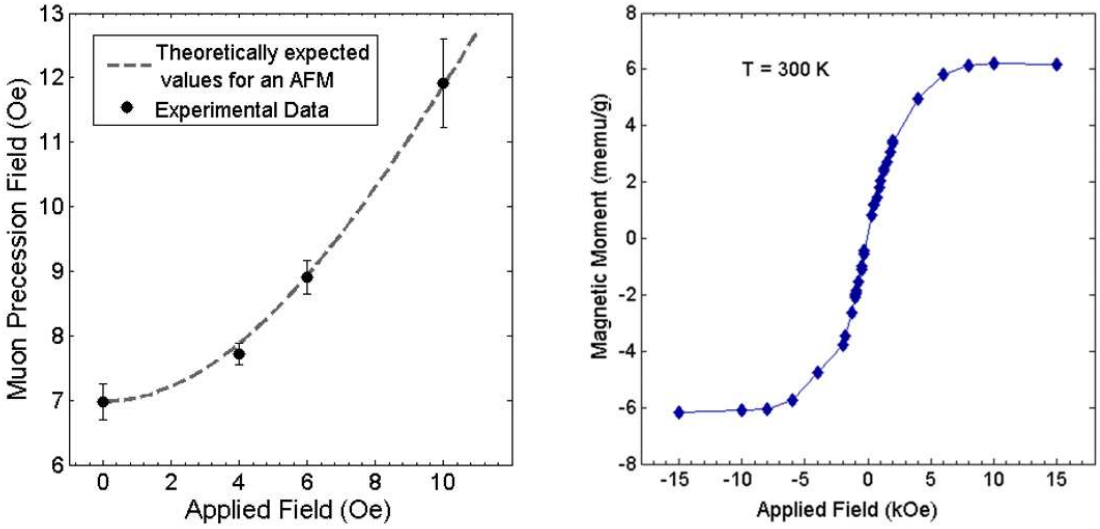

Figure 63. Left. Dependence of the muon precession frequency on small LF. The observed behaviour follows the expectation for the AFM case. **Right.** Ferromagnetic contribution of the SQUID magnetization curve of graphene at 300 K. The dominant diamagnetism has been subtracted (see fig.43, p.63.

A further insight into this issue is obtained by SQUID magnetometry. The field dependence of magnetization in a graphene sample from group **2** (all the samples show the same qualitative behaviour) is shown in the right panel of fig.63. A small ferromagnetic contribution is actually observed and looks contradictory with the evidence of AFM mentioned previously. However, this can be attributed to a small quantity of magnetic impurities ($\simeq$ 25 ppm in this case), observed by elemental analysis.
This result completes the SQUID characterization of graphene, which do not evidence the presence of any magnetic phase in graphene, as confirmed by a recent study [93].

4.4 The hypothesis of nuclear dipolar interactions

The observed precession of the muon spin is also consistent with the formation of a μ-H state, where the local field is the dipolar field of the hydrogen nucleus (see sec.2.2.3).

To yield a similar state the implanted muon have to form Muonium and ends up close to a single hydrogen nucleus.

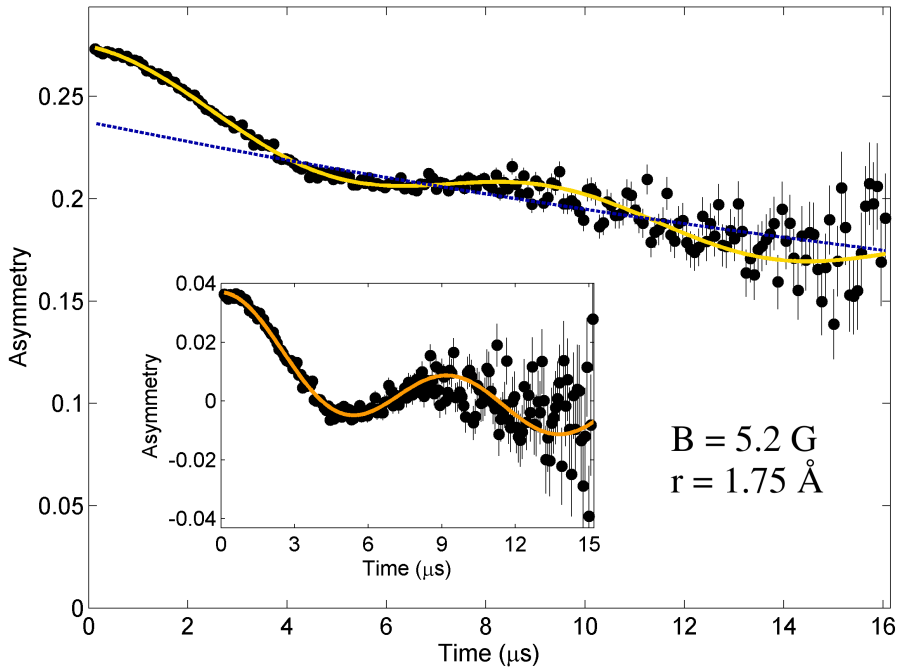

Figure 64. Best fit (yellow solid line) of ZF μSR data for a sample of group **1**, in the hypothesis of μ-H interaction (eq.4.4). The inset display only the oscillating contribution.

In this model the muon polarization is no more described by a simple harmonic oscillation, but takes the form given in eq.(2.21) (with an additional phenomenological damping)

$$P_{osc}(t) = \frac{1}{6}\left[1 + \cos\left(\gamma_\mu B_{dip} t\right) + 2\cos\left(\frac{1}{2}\gamma_\mu B_{dip} t\right) + 2\cos\left(\frac{3}{2}\gamma_\mu B_{dip} t\right)\right] e^{\lambda_{osc} t}. \tag{4.4}$$

The best fit of this expression to the ZF data of a sample from group **1** (same data analyzed for the magnetic hypothesis) yields a dipolar field $B_{dip} = 5.20 \pm 0.05\, G$ and hence a μ-H distance

$$r_{\mu-H} = \sqrt[3]{\frac{\mu_0 \hbar \gamma_H}{4\pi B_d}} = 1.76 \pm 0.006\,\text{Å}. \tag{4.5}$$

On the graphene plane, this distance is consistent with a $Mu - C - H$ (CH_2) configuration, where the muon and the hydrogen are bound to the same carbon atom (fig.65). A similar species can only form either next to a in-plane vacancy or at graphene edges:

the carbon atom, indeed, should be bond only to two other carbons and to an hydrogen, in order to have the last orbital free to host muonium. These "hydrogenated vacancies", as we can shortly call the configuration in the above figure, should be admitted to have an exceptionally high cross section for hydrogen capture, due to the high fraction of precessing muons with respect to the rather low density of defects measured by Raman and SQUID. This suggests that muons (and hence also hydrogen atoms) can easily diffuse onto the graphene plane before being trapped by the defects.

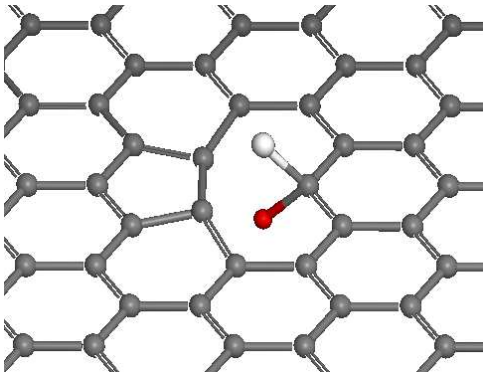

Figure 65. A $Mu-C-H$ (CH_2) configuration, in proximity of an in-plane vacancies.

The whole analysis of experimental data, performed with the *MuLab* suite [185], led to the following results:

- the amplitudes vary irregularly from sample to sample and the interaction interest up to 18% of the total incoming muons;
- All the samples from group **2** revealed, within experimental error, the same dipolar field (and μ-H distance)

  $$B_2 = 5.20 \pm 0.2\,G \qquad r_2 = 1.76 \pm 0.025\,\text{Å}$$

  and similarly the samples from group **3**, but with slightly different values

  $$B_3 = 4.45 \pm 0.1\,G \qquad r_3 = 1.85 \pm 0.02\,\text{Å}.$$

- The behaviour of samples of type **1** is more complex, since they contain an higher concentration of adsorbed chemical species (H,O,OH) and moisture. If they are annealed in vacuum above 600°C, in order to remove these impurities, they display a muon precession frequency consistent to the values of group *2*. In their as-prepared form, instead, they display an higher frequency:

  $$B_1^{as-prep.} = 5.75 \pm 0.05\,G \qquad r_1^{as-prep.} = 1.70 \pm 0.02\,\text{Å}.$$

A first idea to shed new light on these μSR results and try to distinguish the correct hypothesis has been to characterize a group of hydrogenated samples. Their investigation is proposed in the next chapter.

Chapter 5

Hydrogen dipolar interactions in Graphene

5.1 Hydrogenated samples

Stimulated by the interesting results obtained in as-prepared graphenes, the μSR investigations have been extended to hydrogenated samples or, more precisely, to samples treated in hydrogen atmosphere at high temperatures (between 600°C and 1000°C), treatment that proved effective in increasing the hydrogen content in the material (as described in section 3.3). Figure 66 displays the fit of ZF μSR experimental data with

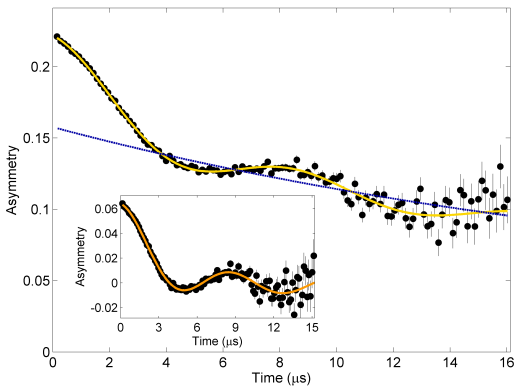

(a). The solid line is the best fit according to the μ-H model (eq. 4.4).

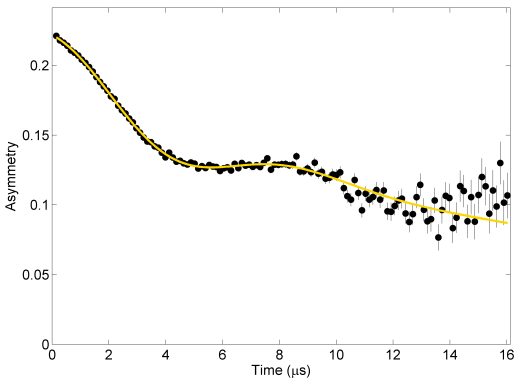

(b). The solid line is the best fit in the hypothesis of magnetic order (eq. 4.2). The inaccuracy of the fit at long times indicate that this model cannot properly account for the muon behaviour in hydrogenated samples.

Figure 66. ZF μSR data in a graphene sample prepared according to method 3 and hydrogenated at 1000°C.

both the considered models. It is apparent that the amplitude of the observed precession is much larger in these new samples: according to the μ-H model, the involved volume fraction ranges from 25 up to 40%, taking the maximum value in the sample hydrogenated at 800°C, and the dipolar field probed by the muon results to be the same in all hydrogenated samples, independently from the preparation of the original graphene

$$B_4 = 5.75 \pm 0.08\, G \qquad r_4 = 1.70 \pm 0.02\, \text{Å}.$$

We may then add a fourth group to the samples table and summarize the μSR results in the $\mu - H$ model as follow:

	Group of Samples studied	
1	Solvothermal Graphene	as-prepared $r_1 = r_4$ annealed $r_1 = r_2$
2	Exfoliation of Reduced GO	$r_2 = 1.76 \pm 0.025$ Å
3	Exfoliation of GO	$r_3 = 1.85 \pm 0.02$ Å
4	Hydrogenated Graphene	$r_4 = 1.70 \pm 0.02$ Å

Table 8. The four different groups of samples characterized by μSR and the observed μ - H distance.

Therefore three different values of the muon-hydrogen distance are measured, with as-prepared samples of type 1 that are found to be equivalent to hydrogenated samples, probably as they actually contain many hydrogen impurities, as anticipated. Since all these dipole-dipole distances are quite closer one to each other, it is difficult to say whether they are geometrical distortions of the same configuration or if the muon-hydrogen interaction occurs at distinct sites. We will address this issue later, with the help of complementary experimental techniques.

Figure 66b also offer an evidence that the magnetic hypothesis does not properly account for the data in hydrogenated samples, as a simple harmonic oscillation does not fit properly in the long times range. On the other hand, the increase of the μSR signal upon hydrogenation is consistent with both the considered models and does not allow to discriminate between the two: indeed it is apparent that the amplitude should increase in the case of a muon-hydrogen dipolar interaction and, when discussing the magnetic properties of graphene, we introduced that a chemisorbed hydrogen could contribute to the formation of a magnetic phase. Further investigations on the origin of the precession are thus needed.

5.2 A specifically designed experiment

A simple experiment has been designed to definitely clarify the origin of the precessing μSR signal. In particular it is proposed to study graphene samples where hydrogen is isotopically substituted by deuterium: in this system, in case of long-range magnetic order the signal should not change with respect to as-prepared or hydrogenated graphene; on the contrary, if the magnetism is of nuclear origin, a lower precession field is expected, due to the lower gyromagnetic ratio of deuterium. The isotope substitution is performed by a thermal treatment in D_2 flow at 800°C: the deuterium-hydrogen exchange during this process resulted efficient, as tested by deuterium NMR experiments (see section 5.4) and inelastic neutron scattering (where the signal of the deuterated sample drop to low intensities and is essentially given by the contribution of carbon, see fig. 67).

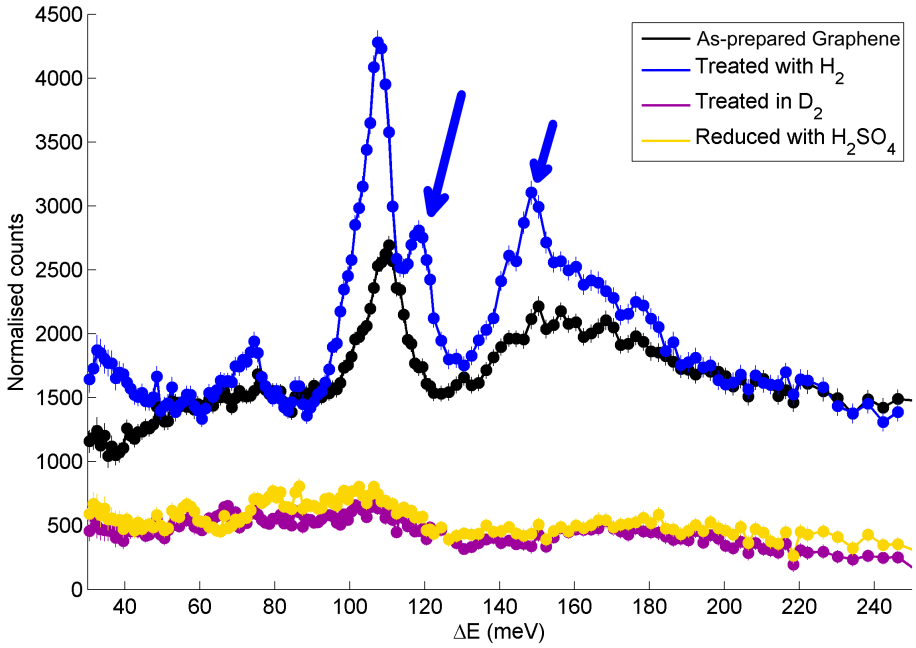

Figure 67. Inelastic neutron scattering spectra for as-prepared, hydrogenated and deuterated graphene and for graphene treated in H_2SO_4 before the exfoliation. The hydrogen contribution is almost negligible in the deuterated sample. The blue arrows stress the features present only in the hydrogenated samples (see the text in section 5.4).

Preliminary μSR data in a deuterated sample shows a relaxation of polarization (that on the typical timescale of the μSR experiment could be also a slow precession, approx. $1\,G$). Although more systematic measurements on deuterated species are needed[1], this result already allows to conclude that THE ONSET OF μ-H DIPOLAR INTERACTIONS IS THE CORRECT INTERPRETATION of the μSR experiments.

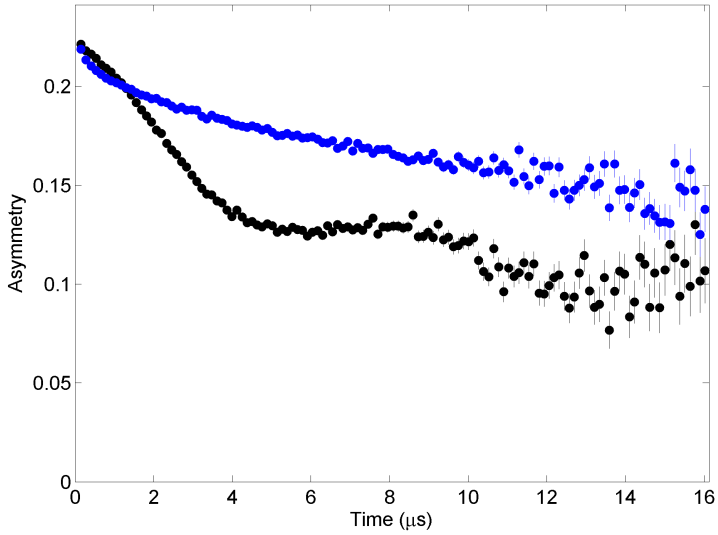

Figure 68. Preliminary μSR ZF measurements in deuterated and hydrogenated graphene. The precession signal is not observed any more in the deuterated sample.

Once again this technique proves to be an efficient experimental tool for the investigation of the hydrogen behaviour in materials. In particular we have seen that muons in graphene probe the dipolar interaction among hydrogen nuclei. The dipole-dipole distance measured is compatible with the formation of CH_2 fragments and suggests that vacancies saturated by hydrogen are effective in binding a second hydrogen atom. Consequently hydrogen shall be supposed to diffuse on the graphene plane before being captured by these sites.
With respect to the magnetic hypothesis, these μSR results, together with our SQUID investigations, pose important limits on magnetism in graphene: μSR, indeed, is very sensitive to the local internal field and does not show the presence of any magnetization.

[1]The fast-relaxing component observed here does not allow to fit this preliminary data to the model developed in chapter 2. A specific μSR experiment on deuterated samples, including measurements at low temperature where the relaxation may slow down, has already been accepted at ISIS and is scheduled shortly.

5.3 More μSR results

In this section some more results of the μSR investigations are described, in order to highlight other relevant features of the muon-hydrogen dipolar interaction. The work on these topics is still in progress and any observation made here (and in the following section) should not be taken as a definitive conclusion, but rather as a suggestion of possible interpretation.

5.3.1 Thermal stability

An important feature of the μSR signal in graphene, which we have left out so far, is its exceptional thermal stability. ZF measurements on hydrogenated graphene have shown that the muon can probe the hydrogen dipolar interaction up to 1220 K, the maximum investigated temperature. This experimental evidence is rather surprising since the thermal detachment of hydrogen (and muonium) from the graphene plane is expected at far lower temperatures: in particular graphane is known to convert to graphene already at 720 K [186].

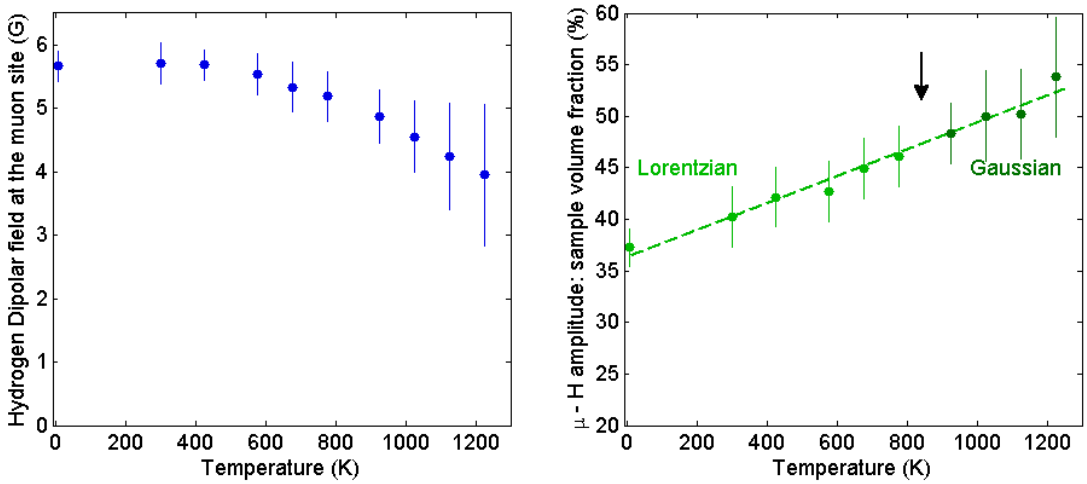

Figure 69. Temperature dependence of **(Left)** the dipolar frequency and of **(Right)** the precessing signal amplitude.

As displayed in figure 69 the nuclear dipolar field is constant from low temperature up to 400 K and then gradually lower with increasing temperature, reaching 4 G at 1220 K. A more complete study is in progress, however the thermal activation of molecular dynamics may be suggested to explain this behaviour, especially if we take into account the isotope effects related to muonium: this hydrogen isotope has a substantially smaller mass and thus its bending and vibrational motions are much

wider and could account for the longer distance (lower precession field) observed at high temperature. On the other hand, the amplitude of the precessing signal is found to increase linearly with temperature. A preliminary explanation can be advanced as follow: we evidenced in section 4.4 that muons could diffuse onto the graphene plane before being trapped by the defects; with high temperature the increase in kinetic energy can bring to a longer average diffusion length and hence the muons would have more probability to reach the defects sites. Furthermore please notice that the damping of the precession component (eq.4.4) changes from Lorentzian to Gaussian above 800 K, as pointed out in the figure. This relaxation is introduced as a phenomenological parameter, related to the dephasing of the muon spins during the precession, similarly to what is usually done with the Bloch equations in NMR (sec. 2.1.2): in general many factors influence this quantity and thus further analyses are needed to explain its complex behaviour. An additional insight on the damping rate, however, is given by its temperature dependence, shown in fig.70b: here it can be seen that it decreases linearly with increasing temperature until it keeps a Lorentzian form and then increases when changing to a Gaussian form.

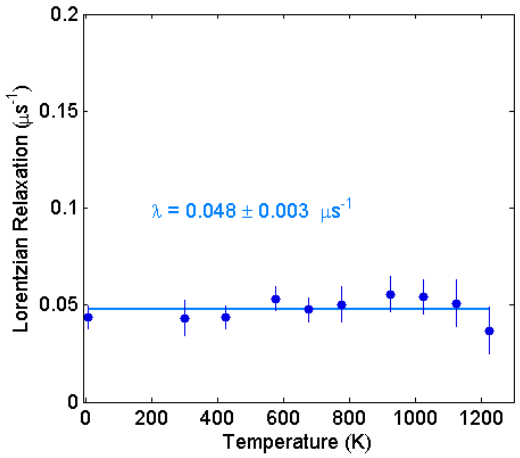

(a). The Lorentzian relaxation rate is constant over the whole temperature range.

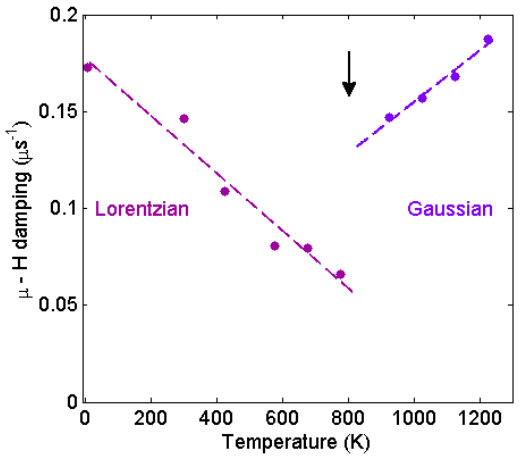

(b). The damping rate for the precessing contribution.

Figure 70. Temperature dependence of μSR relaxation parameters in graphene. Lines are guide for the eye.

Finally, to complete the overview of the temperature dependence of μSR signal, it is worth looking at the behaviour of the non-oscillating component (see eq.4.1): the lorentzian relaxation of polarization, caused by paramagnetic impurities, does not display any dependance on temperature over the whole investigated range, as can be expected due to the high energy of electrons fluctuations, and varies slightly from sample to sample around the average value $\lambda = 0.048 \pm 0.01\,\mu s^{-1}$.

5.3.2 Behaviour in Longitudinal Fields

The dependence of the μ-H interaction on an externally applied field can also be of interest. Preliminary Longitudinal field (LF) measurements in an hydrogenated sample have shown that, for increasing external field, the muon precession frequencies gradually raise, while the involved volume fraction slowly decreases, as can be expected since more and more muons starts to align their polarization to the external field.
Unfortunately it is not possible to offer here a quantitative analysis of the signal, since the mathematical description of the μ-H interaction in presence of an external field is rather complicated and it is still under development.

5.3.3 High statistic measurements

Apart from the groups of samples **1-4** a few additional samples were measured: these include a sample which underwent the reduction step with $NaBH_4$ (typical of group **2**) and a further chemical treatment in H_2SO_4, described in section 3.1.3, which is known to remove the defects from the graphene plane. The ZF μSR signal of this "repaired graphene" is different from anyone else: it displays beats corresponding to a lower hydrogen dipolar field of only $2.1 \pm 0.3\,G$ and hence to a muon-hydrogen distance $r_{\mu-H} = 2.4 \pm 0.1\,\text{Å}$.

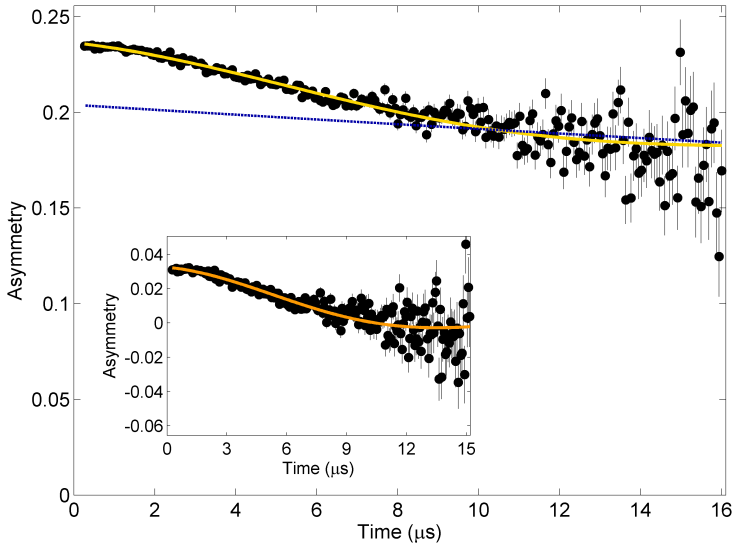

Figure 71. ZF μSR data in the sample treated with sulphuric acid. A slow precession is observed.

This result can be compared to a very high statistics measurement[2] performed on a sample from group **1**[3] . The accuracy reached allows to recognize that a single oscillating component is not enough to properly account for the observed signal and an additional contribution has to be considered. Therefore two different muon-hydrogen interactions sites are involved: one is characterized by the dipole-dipole distance observed from the beginning

$$B_{dip} = 5.22 \pm 0.05\, G \qquad r = 1.76 \pm 0.02\, \text{Å}$$

while the dipolar field at the second site is found to be consistent to the one measured in the "repaired graphene"

$$B_{dip} = 1.70 \pm 0.15\, G \qquad r = 2.55 \pm 0.06\, \text{Å}\,.$$

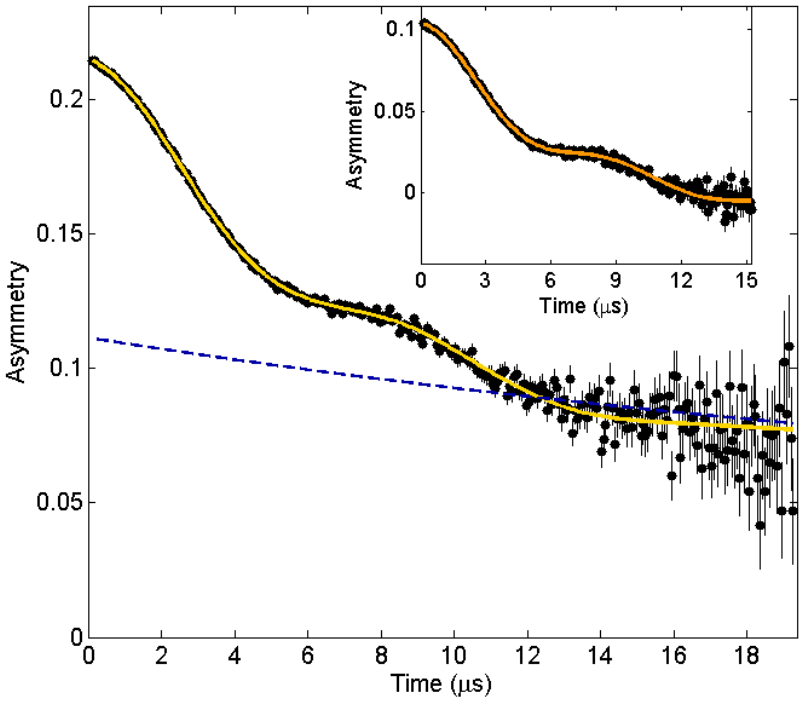

Figure 72. ZF μSR data (black points) in a sample from group **1**, recorded with a very high statistic. An accurate fit (yellow solid line)is obtained by considering two precessing components. The sum of their contributions is shown in the inset, where the relaxing part is subtracted.

[2]We have not considered up to now this high statistics measurements for clarity.

[3]This sample has been annealed in vacuum at 800°C and then, as discussed, display the same dipolar frequency of samples from group **2**.

This may lead us to consider that in-plane defects, similar to the hydrogenated vacancies of fig.65, are the sites with a typical μ-H distance of approximately 1.75 Å; after the chemical treatment in H_2SO_4, that is effective in removing these vacancies, only the other component is left: its characteristic μ-H length, $2.4 - 2.5$ Å, may be identified in the graphene lattice as the distance between the aromatic meta-carbons (second nearest-neighbours) or as the C-C distance along zigzag edges.

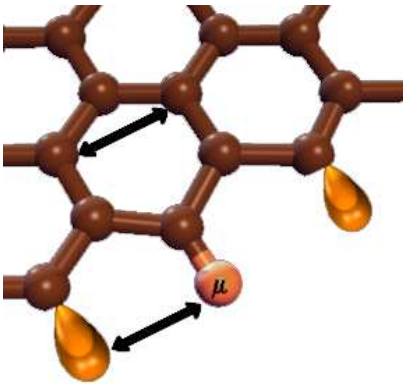

Figure 73. Distances of 2.4Å in the graphene structure.

5.4 Sites of interaction

In the following we address the emerging question about which types of defects host the muon-hydrogen dipolar interactions and are therefore privileged sites for hydrogen in graphene. To this aim, besides μSR results, we consider the perspective offered by a complementary technique, solid state NMR; thanks to the availability of deuterated graphene samples, we have performed NMR measurements on the deuterium nuclei: the quadrupolar interaction, indeed, strongly depend on structural details and may help to distinguish the sites of interaction.

^2H NMR in graphene

Deuterium NMR measurements in graphene has been performed with a commercial Tecmag Apollo spectrometer and a Bruker standard probe for solid state NMR, in an external field of approximately 8 T (^2H resonance frequency 52.3178 MHz). Both deuterated water and plexiglass were used as reference compounds[4].
Figure 74 displays the NMR powder spectrum recorded over a long acquisition (3 week, approximately 200 000 repetitions), after proper data analysis. Here the red solid line is the best fit to the spectrum[5] , including two quadrupolar components with vanishing asymmetry parameters and quadrupolar frequencies $\omega_{Q1} = 136\,kHz$ and $\omega_{Q2} = 36.6\,kHz$ for the most and least intense respectively.

[4]In water motional narrowing effects occur and a single line is observed. This may help to tune the resonance frequency and set the pulse length. In plexiglass the full quadrupolar spectrum of alkyl deuterons is visible and the sequence and parameters for the experiments can be tested.

[5]For the interpolation of NMR spectra we used specific libraries for the simulation of quadrupolar powder pattern, courtesy of Prof. G.Allodi (Parma University).

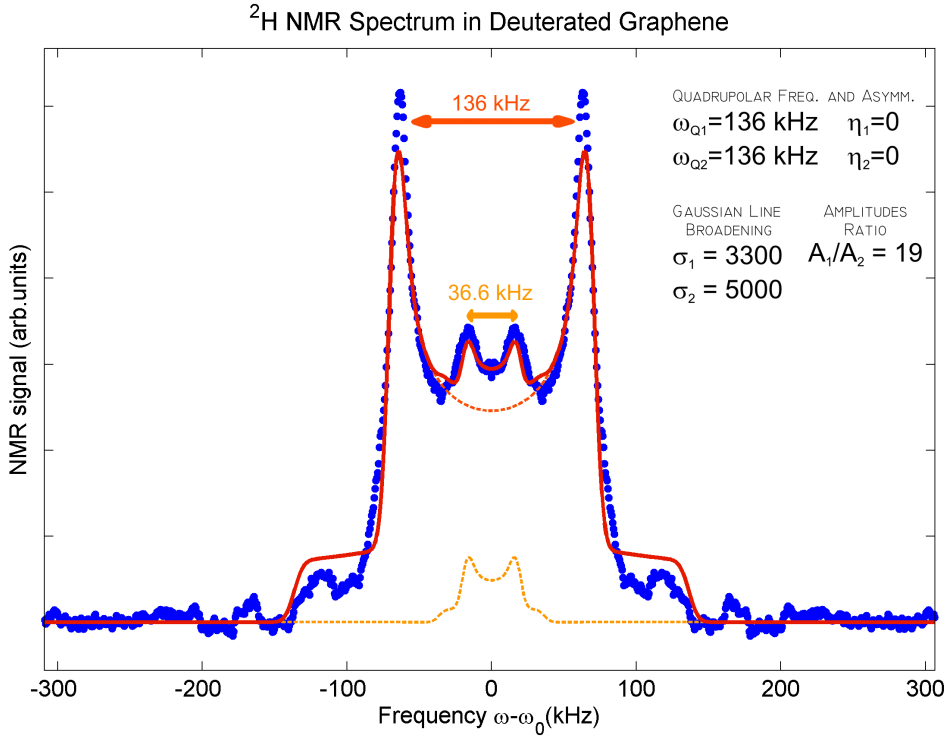

Figure 74. ^2H NMR spectrum of deuterated graphene at 300 K . The best fit (red solid line) to experimental data (blue points) include two well evident quadrupolar contributions (dashed lines).

The evidence for two different quadrupolar frequencies suggest deuterium (hydrogen) populates two distinct sites on graphene. However, to obtain more information from NMR, calculations of the electric field gradient need to be developed.

Comparison with other techniques

The observation of two different sites for hydrogen in graphene seems to be related to other experimental observations. In *Inelastic Neutron Scattering* the major peaks in the spectrum of as-prepared graphene seem to be related to a single molecular dynamics, already observed in other carbon-based systems [187] , while additional features are visible only in hydrogenated samples: in particular, as evidenced by the blue arrows in fig.67, the contribution around $150\,meV$ becomes more pronounced and a new peak appears at $120\,meV$. At first sight, from these results it seems that upon hydrogenation a new site starts to be populated by the hydrogen atoms and a total of two sites are thus seen by neutrons. To confirm these suggestions, first principle simulations on hydrogen dynamics in graphene have to be performed. Together with the planned investigation of the Quasi Elastic region of the spectrum, these calculations will help to get a more complete picture.

The existence of two possible sites of interaction is also strongly related to μSR results: at the current development of the analyses, however, it is not possible to confirm whether the two quadrupolar frequencies seen by NMR correspond to the two dipolar lengths discussed in the last section (1.75 and 2.50 Å) or rather to two of the slightly different distances reported in table 8. Moreover we cannot exclude the possibility that the two sites evidences may have the same muon-hydrogen dipolar frequency.

The experimental results outlined above about the possible sites of interaction lead to a few open questions: the 2 possible hydrogen sites observed can be attributed to specific defects (maybe in-plane vacancies and edges)? Is there any possibility to distinguish the μSR contributions of different type of defects? Which sites are more effective in attracting hydrogen? The development of the researches started in this chapter, mainly arisen from the μSR characterization, can answer these questions and be of help for the general understanding of the hydrogen interactions in graphene.

Conclusions

In the present thesis large scale samples of graphene have been prepared by different chemical methods and characterized by Muon Spin Rotation/Relaxation and other complementary techniques.
With respect to synthesis, the graphite oxidation and thermal exfoliation processes have been optimized and are found to be effective for the production of single-layer gram-scale graphene samples. Besides the traditional electron microscopies, also a bulk solid-state technique, Inelastic Neutron Scattering, has demonstrated to provide valuable structural information and feedbacks on the preparation procedure.
The main results has come from μSR spectroscopy, which proved a useful tool to study the interactions of the hydrogen atom with the defective graphene plane. A clear muon spin precession is observed in all the samples, contrary to the standard behaviour of graphite and to what observed in nanographites, which displayed only a slow relaxation. Its origin lies in the magnetic dipolar interactions of hydrogen nuclei present at defects, which reveal the structural conformation of hydrogen impurities sites. In particular it was found that the observed precession could be attributed to the formation of a $CHMu$ (CH_2) state and the signal amplitude suggests that vacancies saturated by hydrogen have an extraordinary hydrogen capture cross-section.
With respect to the magnetic hypothesis, the μSR results, together with our SQUID investigations, pose important limits on magnetism in graphene: μSR, indeed, is very sensitive to the local internal field and does not show the presence of any magnetization. From the μSR investigation several open questions have emerged, in particular regarding which type of the defects that host the CH_2 species. The Neutron Scattering and NMR investigations discussed at the end of chapter 5 are intended to address these issues and the analyses are in progress. In particular to extract structural information from the NMR data, it will be necessary to evaluate the electric filed gradient at deuterium sites. The study of graphene dynamics by Inelastic neutron scattering will be extended to the Quasi-Elastic region and first-principle simulations will allow the interpretation of the spectra.

Other short-term developments of the μSR studies include:

- further investigations on the thermal stability of the interactions even above the maximum investigated temperature (1220 K);
- the extension of μSR measurements of deuterated samples at low temperature, where the possibly slower relaxation may help to fit the data;
- the mathematical description of the μ-H interaction in presence of an external field and the analysis the corresponding LF μSR data.

More long-term perspectives are related to the integration of the present research into the international *HyCarbo*[6] project, addressed to the development of carbon-based materials for hydrogen storage applications.
Within this framework, useful studies can be directed on the one hand to a comprehensive understanding of the interactions of hydrogen atoms and molecules with the graphene layer and, on the other hand,to the improvement of synthesis procedures, to possibly control and even engineering the defects concentration and the hydrogen interaction sites.

[6]This project is funded by the Swiss National Science Foundation and sees the collaboration among Parma University, the EMPA Swiss federal institute, section *Hydrogen and energy*, and other Swiss academic institutions.

Appendix A

Muon-Hydrogen dipolar interaction

The dipolar interaction between the muon spin $\vec{I}$ and the hydrogen nuclear spin $\vec{S}$ can be expressed by the Hamiltonian

$$\begin{aligned} \mathcal{H} &= -\frac{\mu_0}{4\pi r^3}\hbar^2\,\gamma_\mu\,\gamma_H\left[3\left(\vec{I}\cdot\hat{r}\right)\left(\vec{S}\cdot\hat{r}\right)-\vec{I}\cdot\vec{S}\right] \\ &= -\hbar\omega_D\left[3\left(\vec{I}\cdot\hat{r}\right)\left(\vec{S}\cdot\hat{r}\right)-\vec{I}\cdot\vec{S}\right] \end{aligned} \tag{A.1}$$

where, for convenience, the front coefficients and the dipole-dipole distance r are included in the definition of the dipolar frequency $\omega_D = -\hbar\,\gamma_\mu\,\gamma_H\,\frac{\mu_0}{4\pi r^3}$.
Chosen a reference frame with the z axis oriented along the dipole axis this become

$$\mathcal{H} = -\hbar\omega_D\left(2I_zS_z - I_xS_x - I_yS_y\right).$$

In the following the time evolution of the muon spin polarization is evaluated starting from the above Hamiltonian.

1. First consider the ordinary Pauli spin matrices ($I = S = \frac{1}{2}$)

$$I_x = S_x = \frac{1}{2}\begin{pmatrix} 0 & 1 \\ 1 & 0 \end{pmatrix} \qquad I_y = S_y = \frac{1}{2}\begin{pmatrix} 0 & -i \\ i & 0 \end{pmatrix} \qquad I_z = S_z = \frac{1}{2}\begin{pmatrix} 1 & 0 \\ 0 & -1 \end{pmatrix}$$

2. The different terms of the Hamiltonian can be evaluated as direct products of these spins in a (4×4) tensor space (in the products the proton is chosen as the outer components, while the muon is associated to the inner component):

$$S_z\otimes I_z = \frac{1}{4}\begin{pmatrix} 1 & 0 & 0 & 0 \\ 0 & -1 & 0 & 0 \\ 0 & 0 & -1 & 0 \\ 0 & 0 & 0 & 1 \end{pmatrix} \quad S_x\otimes I_x = \frac{1}{4}\begin{pmatrix} 0 & 0 & 0 & 1 \\ 0 & 0 & 1 & 0 \\ 0 & 1 & 0 & 0 \\ 1 & 0 & 0 & 0 \end{pmatrix} \quad S_y\otimes I_y = \frac{1}{4}\begin{pmatrix} 0 & 0 & 0 & -1 \\ 0 & 0 & 1 & 0 \\ 0 & 1 & 0 & 0 \\ -1 & 0 & 0 & 0 \end{pmatrix}$$

The total Hamiltonian results

$$\mathcal{H} \;=\; -\hbar\omega_D\,(2I_zS_z - I_xS_x - I_yS_y) \;=\; \frac{\hbar\omega_D}{2}\begin{pmatrix} -1 & 0 & 0 & 0 \\ 0 & 1 & 1 & 0 \\ 0 & 1 & 1 & 0 \\ 0 & 0 & 0 & -1 \end{pmatrix}$$

3. The computation of the energy eigenvalues can be obtained from the characteristic equation

$$\begin{aligned} det(A-\lambda I) \;&=\; 0 \\ (-1-\lambda)^2\left[(1-\lambda)^2-1\right] \;&=\; 0 \\ (\lambda+1)^2\left(\lambda^2-2\lambda\right) \;&=\; (\lambda+1)^2\,\lambda\,(\lambda-1) \;=\; 0 \end{aligned}$$

and results

$$\lambda_{1/4}, \;=\; -\frac{1}{2}\hbar\omega_D \quad \lambda_2 \;=\; 0 \quad \lambda_3 \;=\; \hbar\omega_D$$

The transformation from the basis set of I_z, D_z to the basis set of the energy eigenstates results turns out to be expressed by the unitary matrix [1]

$$U \;=\; \hbar\begin{pmatrix} 1 & 0 & 0 & 0 \\ 0 & -\frac{\sqrt{2}}{2} & \frac{\sqrt{2}}{2} & 0 \\ 0 & \frac{\sqrt{2}}{2} & \frac{\sqrt{2}}{2} & 0 \\ 0 & 0 & 0 & 1 \end{pmatrix}$$

4. The diagonal form of the Hamiltonian allows to easily evaluate the time evolution operator

$$E_{diag}(t) \;=\; e^{-i\frac{\mathcal{H}}{\hbar}t} \;=\; \begin{pmatrix} e^{\frac{1}{2}i\omega_D t} & 0 & 0 & 0 \\ 0 & 1 & 0 & 0 \\ 0 & 0 & e^{-i\omega_D t} & 0 \\ 0 & 0 & 0 & e^{\frac{1}{2}i\omega_D t} \end{pmatrix} \;=\; \begin{pmatrix} \alpha^{-1} & 0 & 0 & 0 \\ 0 & 1 & 0 & 0 \\ 0 & 0 & \alpha^2 & 0 \\ 0 & 0 & 0 & \alpha^{-1} \end{pmatrix}$$

[1] As indicated by the dotted lines, the eigenvectors in these matrix are ordered by columns. Notice that this convention, although very common, is opposite to the one used in the *Mathematica* software, generally used to handle similar symbolic matrices. According to this convention the diagonal form of the Hamiltonian is given by $\mathcal{H}_D = U^{-1}\mathcal{H}U$.

where, for convenience, α has been defined as $\alpha = e^{-\frac{1}{2}i\omega_D t}$. Back in the basis set of angular momenta (I_z and D_z) the time evolution operator is given by

$$E(t) \,=\, U\, E_{diag}(t)\, U^{-1} \,=\, \left(\begin{array}{c|cc|c} \alpha^{-1} & 0 & 0 & 0 \\ \hline 0 & \frac{1}{2}+\frac{1}{2}\alpha^2 & -\frac{1}{2}+\frac{1}{2}\alpha^2 & 0 \\ 0 & -\frac{1}{2}+\frac{1}{2}\alpha^2 & \frac{1}{2}+\frac{1}{2}\alpha^2 & 0 \\ \hline 0 & 0 & 0 & e^{\frac{1}{2}i\omega_D t} \end{array}\right)$$

For later use, it is worth evaluating this matrix also at time $-t$

$$E(-t) \,=\, U\, E_{diag}(-t)\, U^{-1} \,=\, \left(\begin{array}{c|cc|c} \alpha^{-1} & 0 & 0 & 0 \\ \hline 0 & \frac{1}{2}+\frac{1}{2}\alpha^{-2} & -\frac{1}{2}+\frac{1}{2}\alpha^{-2} & 0 \\ 0 & -\frac{1}{2}+\frac{1}{2}\alpha^{-2} & \frac{1}{2}+\frac{1}{2}\alpha^{-2} & 0 \\ \hline 0 & 0 & 0 & e^{\frac{1}{2}i\omega_D t} \end{array}\right)$$

5. As we deal with LF μSR experiment, we now need to change the reference frame from the principal axes of the dipolar interaction to a new coordinate system (x', y', z') whose z' axis is oriented along the initial muon spin polarization. The muon spin projection along the dipole axis (which we call I_ζ and not I_z anymore, in order to stress we are writing it in a different reference frame) is now given by

$$I_\zeta \,=\, I_{z'}\,\cos\theta + I_{x'}\,\sin\theta \,=\, \frac{1}{2}\cos\theta \left(\begin{array}{cc} 1 & 0 \\ 0 & -1 \end{array}\right) + \frac{1}{2}\sin\theta \left(\begin{array}{cc} 0 & 1 \\ 1 & 0 \end{array}\right) \,=\, \frac{1}{2}\left(\begin{array}{cc} \cos\theta & \sin\theta \\ \sin\theta & -\cos\theta \end{array}\right)$$

and in the tensor space it is written as

$$I_\zeta \,=\, \mathbb{I}_2 \otimes I_\zeta \,=\, \frac{1}{2}\left(\begin{array}{cc|cc} \cos\theta & \sin\theta & 0 & 0 \\ \sin\theta & -\cos\theta & 0 & 0 \\ \hline 0 & 0 & \cos\theta & \sin\theta \\ 0 & 0 & \sin\theta & -\cos\theta \end{array}\right)$$

6. The muon spin polarization observed in μSR is the expectation value of this operator and can be obtained as

$$P(t) \,=\, Tr\,\left[E(t)\, I_\zeta\, E(-t)\, I_\zeta\right]\,.$$

Exploding the complex exponentials in their real and imaginary parts one gets

$$\begin{aligned} P(t) \,=\, & \frac{1}{4}\cos^2\theta\,\left[2+\cos\left(\omega_D t\right) - i\sin\left(\omega_D t\right) + \cos\left(\omega_D t\right) + i\sin\left(\omega_D t\right)\right] + \\ & + \,\frac{1}{4}\sin^2\theta\,\left[\cos\left(\frac{\omega_D t}{2}\right) - i\sin\left(\frac{\omega_D t}{2}\right) + \cos\left(\frac{\omega_D t}{2}\right) + i\sin\left(\frac{\omega_D t}{2}\right) + 2\cos\left(\frac{3}{2}\omega_D t\right)\right] \end{aligned}$$

$$P(t) \;=\; \frac{1}{2}\cos^2\theta\;[1+\cos(\omega_D t)] \;+\; \frac{1}{2}\sin^2\theta\;\left[\cos\left(\frac{\omega_D t}{2}\right)+\cos\left(\frac{3}{2}\omega_D t\right)\right]$$

This expression describe the muon spin polarization for the case of a single crystal with the dipole axis which form an angle θ with respect to $P(0)$.

7. For polycrystalline samples the "powder average" over all possible orientations have to be performed [132]

$$\begin{aligned}\langle P(t)\rangle \;&=\; \frac{1}{8\pi^2}\int_0^{2\pi} d\alpha \int_0^{2\pi} d\gamma \int_0^{\pi} d\theta\;\sin\theta\,P(t)\\ &=\; \frac{1}{8\pi^2}\,2\pi\,2\pi\int_0^{\pi} P(t)\;\sin\theta\,d\theta\\ &=\frac{1}{4}\left[1+\cos(\omega_D t)\right]\int_0^{\pi}\cos^2\theta\;\sin\theta\,d\theta \;+\; \frac{1}{4}\left[\cos\left(\frac{\omega_D t}{2}\right)+\cos\left(\frac{3}{2}\omega_D t\right)\right]\int_0^{\pi}\sin^3\theta\,d\theta\end{aligned}$$

The simple integrals to be performed are:

$$\begin{aligned}\longrightarrow &\int_0^{\pi}\cos^2\theta\;\sin\theta d\theta \;=\; \int_0^{\pi} -\cos^2\theta\,d(\cos\theta) \;=\\ &=\;\frac{\cos^3\theta}{3}\Big|_0^{\pi} \;=\; \frac{2}{3}\end{aligned}$$

$$\begin{aligned}\longrightarrow &\int_0^{\pi}\sin^2\theta\sin\theta d\theta \;=\; \int_0^{\pi}(1-\cos^2\theta)\sin\theta d\theta \;=\\ &=\;\int_0^{\pi}\sin\theta d\theta \;-\; \int_0^{\pi}\cos^2\theta\;\sin\theta d\theta \;=\\ &=\;(-\cos\theta)\big|_0^{\pi} \;-\; \frac{2}{3} \;=\; 1+1-\frac{2}{3} \;=\; \frac{4}{3}\quad .\end{aligned}$$

And the powder average of polarization finally results

$$\langle P(t)\rangle \;=\; \frac{1}{6}\left[1 \;+\; \cos(\omega_D t) \;+\; 2\,\cos\left(\frac{1}{2}\omega_D t\right) \;+\; 2\,\cos\left(\frac{3}{2}\omega_D t\right)\right].$$

The latter equation is the model function to be used for the interpolation of ZF μSR data in powder samples where the muon experience the nuclear dipolar field of an hydrogen atom.

Appendix B

Muon-Deuterium dipolar interaction

In the following the full calculations of the muon spin polarization function in case of μ-D dipolar interaction are shown. The general procedure and the main steps followed are already described in section 2.2.3. Here more mathematical details can be found.

The μ-D Hamiltonian includes both a dipolar and a quadrupolar term (spin $D = 1$). ^2H NMR experiments (see section 5.4) have shown that graphene display a vanishing asymmetry of the quadrupolar interaction ($\eta = 0$), as expected for a 2DIM material. Within this approximation the full Hamiltonian is:

$$\begin{aligned}\mathcal{H} \;=\; & -\hbar\omega_D \left[3\left(\vec{I}\cdot\hat{r}\right)\left(\vec{D}\cdot\hat{r}\right) - \vec{I}\cdot\vec{D}\right] + \\ & + \frac{eQV_{ZZ}}{4D(D+1)\cdot 2}\left(3\cos^2\beta - 1\right)\left[3D_z^2 - D(D+1)\right]\end{aligned}$$

Here the dipolar frequency is defined like in the μ-H case and the quadrupolar parameters are the same introduced in the NMR section (2.1). β is the angle between the dipole axis and the direction of the electric field gradient at the deuterium site (Z principal axis of the quadrupolar interaction). It will remain up to the end and will be considered a parameter of the fit model function.
It is convenient to define also the quadrupolar frequency ω_Q and the quadrupolar constant k_Q as

$$\omega_Q \;=\; \frac{3eQV_Z Z}{4D(2D-1)\hbar} \qquad\qquad k_Q \;=\; \frac{\omega_Q}{2}\left(3\cos^2\beta - 1\right)$$

and, if a reference frame with the z axis oriented along the dipole axis is chosen, the

Hamiltonian reduces to

$$\mathcal{H} = - -\hbar\omega_D \left(2I_zS_z - I_xS_x - I_yS_y\right) + \\ + \frac{\hbar k_Q}{3}\left[3D_z^2 - D(D+1)\right]$$

The last term $D(D+1)$ is a constant and introduce only a rigid shift of the energy levels: as far as we are interested in the muon precessing frequencies (i.e. in energy differences) this part can be neglected and the latest expression further simplifies to

$$\mathcal{H} = -\hbar\omega_D \left(2I_zS_z - I_xS_x - I_yS_y\right) + \hbar\, k_Q\, D_z^2\,.$$

In the following the time evolution of the muon spin polarization is evaluated starting from the above Hamiltonian.

1. First consider the Pauli spin matrices for the muon spin ($I = 1/2$) and for the deuterium spin ($D = 1$):

$$I_x = \frac{1}{2}\begin{pmatrix} 0 & 1 \\ 1 & 0 \end{pmatrix} \qquad I_y = \frac{1}{2}\begin{pmatrix} 0 & -i \\ i & 0 \end{pmatrix} \qquad I_z = \frac{1}{2}\begin{pmatrix} 1 & 0 \\ 0 & -1 \end{pmatrix}$$

$$D_x = \frac{1}{\sqrt{2}}\begin{pmatrix} 0 & 1 & 0 \\ 1 & 0 & 1 \\ 0 & 1 & 0 \end{pmatrix} \qquad D_y = \frac{1}{\sqrt{2}}\begin{pmatrix} 0 & -i & 0 \\ i & 0 & -i \\ 0 & i & 0 \end{pmatrix} \qquad D_z = \frac{1}{\sqrt{2}}\begin{pmatrix} 1 & 0 & 0 \\ 0 & 0 & 0 \\ 0 & 0 & -1 \end{pmatrix}$$

2. The different terms of the Hamiltonian can be evaluated as direct products of these spins in a (6×6) tensor space (in the products deuterium is chosen as the outer components, while the muon is associated to the inner component):

$$D_z \otimes I_z = \frac{1}{2}\left(\begin{array}{cc:cc:cc} 1 & 0 & & & & \\ 0 & -1 & & 0 & & 0 \\ \hdashline & & & & & \\ & 0 & & 0 & & 0 \\ \hdashline & & & & -1 & 0 \\ & 0 & & 0 & 0 & 1 \end{array}\right)$$

$$D_x \otimes I_x = \frac{1}{2\sqrt{2}}\left(\begin{array}{cc:cc:cc} & & 0 & +1 & & \\ & 0 & +1 & 0 & & 0 \\ \hdashline 0 & +1 & & & 0 & +1 \\ +1 & 0 & & 0 & +1 & 0 \\ \hdashline & & 0 & +1 & & \\ & 0 & +1 & 0 & & 0 \end{array}\right)$$

$$D_y \otimes I_y \;=\; \frac{1}{2\sqrt{2}} \left(\begin{array}{c:cc:c} & 0 & -1 & \\ 0 & 1 & 0 & 0 \\ & & & \\ \hdashline 0 & 1 & & 0 & -1 \\ -1 & 0 & 0 & 1 & 0 \\ \hdashline & & & \\ 0 & 0 & 1 & 0 \\ & -1 & 0 & \end{array}\right)$$

The last term to be computed is

$$D_z^2 \;=\; \left(\begin{array}{ccc} 1 & 0 & 0 \\ 0 & 0 & 0 \\ 0 & 0 & 1 \end{array}\right) \quad \text{and in the tensor space} \quad \mathbb{I}_2 \otimes D_z^2 \;=\; \left(\begin{array}{cc:c:cc} 1 & 0 & & & \\ 0 & 1 & 0 & 0 & \\ \hdashline & & & & \\ 0 & & 0 & 0 & \\ \hdashline & & & 1 & 0 \\ 0 & & 0 & 0 & 1 \end{array}\right)$$

To evaluate the total hamiltonian

$$\mathcal{H} \;=\; -\hbar\omega_D \left(2I_zS_z - I_xS_x - I_yS_y\right) + \hbar\, k_Q\, D_z^2$$

one can first perform the sum in the parentheses

$$\left(\begin{array}{cccccc} 2 & 0 & 0 & 0 & 0 & 0 \\ 0 & -2 & -\frac{1}{\sqrt{2}} & 0 & 0 & 0 \\ 0 & -\frac{1}{\sqrt{2}} & 0 & 0 & 0 & 0 \\ 0 & 0 & 0 & 0 & -\frac{1}{\sqrt{2}} & 0 \\ 0 & 0 & 0 & -\frac{1}{\sqrt{2}} & -2 & 0 \\ 0 & 0 & 0 & 0 & 0 & 2 \end{array}\right).$$

and, in turn, $\mathcal{H}$ results

$$\mathcal{H} \;=\; \hbar \left(\begin{array}{ccc:ccc} -2\omega_D + k_Q & 0 & 0 & & & \\ 0 & +2\omega_D + k_Q & \frac{\sqrt{2}}{2}\omega_D & & 0 & \\ 0 & \frac{\sqrt{2}}{2}\omega_D & 0 & & & \\ \hdashline & & & 0 & \frac{\sqrt{2}}{2}\omega_D & 0 \\ & 0 & & \frac{\sqrt{2}}{2}\omega_D & +2\omega_D + k_Q & 0 \\ & & & 0 & 0 & -2\omega_D + k_Q \end{array}\right)$$

For clarity in the subsequent calculations the D and Q subscripts of the dipolar frequency ω and quadrupole constant k will be omitted and we define the additional parameter α as

$$\alpha \;=\; \sqrt{6\omega^2 + 4\omega k + k^2}$$

3. The computation of the energy eigenvalues λ_i yields

$$\lambda_{1,2} \;=\; \hbar(-2\omega + k) \qquad \lambda_{3,4} \;=\; \frac{\hbar}{2}(2\omega + k - \alpha) \qquad \lambda_{5,6} \;=\; \frac{\hbar}{2}(2\omega + k + \alpha)$$

and the eigenvectors matrix U that express the transformation from the basis set of I_z, D_z to the basis set of the energy eigenstates results [1]

$$U \;=\; \hbar \left(\begin{array}{cc:c:c:c:c} 1 & 0 & 0 & 0 & 0 & 0 \\ 0 & 0 & 0 & \dfrac{2\omega+k-\alpha}{\omega\sqrt{2}} & 0 & \dfrac{2\omega+k+\alpha}{\omega\sqrt{2}} \\ 0 & 0 & 0 & 1 & 0 & 1 \\ 0 & 0 & -\dfrac{2\omega+k+\alpha}{\omega\sqrt{2}} & 0 & -\dfrac{2\omega+k-\alpha}{\omega\sqrt{2}} & 0 \\ 0 & 0 & 1 & 0 & 1 & 0 \\ 0 & 1 & 0 & 0 & 0 & 0 \end{array}\right)$$

4. The diagonal form of the Hamiltonian allows to easily evaluate the time evolution operator

$$E_{diag}(t) \;=\; e^{-i\,\frac{\mathcal{H}}{\hbar}\,t} \;=\; \left(\begin{array}{ccc:ccc} e^{i(2\omega-k)t} & 0 & 0 & & & \\ 0 & e^{i(2\omega-k)t} & 0 & & 0 & \\ 0 & 0 & e^{-\frac{i}{2}(2\omega+k-\alpha)t} & & & \\ \hdashline & & & e^{-\frac{i}{2}(2\omega+k-\alpha)t} & 0 & 0 \\ & 0 & & 0 & e^{-\frac{i}{2}(2\omega+k+\alpha)t} & 0 \\ & & & 0 & 0 & e^{-\frac{i}{2}(2\omega+k+\alpha)t} \end{array}\right)$$

which back in the basis set of angular momenta (I_z and D_z) is given by

$$E(t) \;=\; U\, E_{diag}(t)\, U^{-1}$$

and for convenience we should also evaluate

$$E(-t) \;=\; U\, E_{diag}(-t)\, U^{-1}$$

[1] s indicated by the dotted lines, the eigenvectors in these matrix are ordered by columns. Notice that this convention, although very common, is opposite to the one used in the *Mathematica* software, generally used to handle similar symbolic matrices. According to this convention the diagonal form of the Hamiltonian is given by $\mathcal{H}_D = U^{-1}\mathcal{H}U$.

5. As we deal with LF μSR experiment, we now need to change the reference frame from the principal axes of the dipolar interaction to a new coordinate system (x', y', z') whose z' axis is oriented along the initial muon spin polarization. The muon spin projection along the dipole axis (which we call I_ζ and not I_z anymore, in order to stress we are writing it in a different reference frame) is now given by

$$I_\zeta \,=\, I_{z'}\,\cos\theta + I_{x'}\,\sin\theta \,=\, \frac{1}{2}\cos\theta \begin{pmatrix} 1 & 0 \\ 0 & -1 \end{pmatrix} + \frac{1}{2}\sin\theta \begin{pmatrix} 0 & 1 \\ 1 & 0 \end{pmatrix} \,=\, \frac{1}{2}\begin{pmatrix} \cos\theta & \sin\theta \\ \sin\theta & -\cos\theta \end{pmatrix}$$

and in the tensor space it is written as

$$I_\zeta \,=\, \mathbb{I}_3 \otimes I_\zeta \,=\, \frac{1}{2}\begin{pmatrix} \cos\theta & \sin\theta & 0 & 0 & 0 & 0 \\ \sin\theta & -\cos\theta & 0 & 0 & 0 & 0 \\ 0 & 0 & \cos\theta & \sin\theta & 0 & 0 \\ 0 & 0 & \sin\theta & -\cos\theta & 0 & 0 \\ 0 & 0 & 0 & 0 & \cos\theta & \sin\theta \\ 0 & 0 & 0 & 0 & \sin\theta & -\cos\theta \end{pmatrix}$$

6. The polarization observed in μSR is the expectation value of this operator and can be obtained as

$$\begin{aligned}
P(t) \,&=\, Tr\,\left[E(t)\,I_\zeta\,E(-t)\,I_\zeta\right] \\
P(t) \,&=\frac{1}{2\alpha^2}\cos^2\theta\,\left[3k^2 \,+\, 12k\omega \,+\, 14\omega^2 \,+\, 4\omega^2\cos\left(\alpha t\right)\right] + \\
&\quad +\, \frac{1}{4\alpha^2}\sin^2\theta\, e^{-2ikt}\,\cdot \\
&\quad \left\{\omega^2 e^{it(2k-\alpha)} \,+\, \omega^2 e^{it(2k+\alpha)} \,+\, 2e^{i\,2kt}\left(\alpha^2-\omega^2\right) \,+\right. \\
&\quad +\, e^{\frac{it}{2}(3k-6\omega-\alpha)}\,\left(\alpha^2-k\alpha-2\omega\alpha\right) \,+ \\
&\quad +\, e^{\frac{it}{2}(5k-6\omega+\alpha)}\,\left(\alpha^2-k\alpha-2\omega\alpha\right) \,+ \\
&\quad +\, e^{\frac{it}{2}(5k-6\omega-\alpha)}\,\left(\alpha^2+k\alpha+2\omega\alpha\right) \,+ \\
&\quad \left.+\, e^{\frac{it}{2}(3k+6\omega+\alpha)}\,\left(\alpha^2+k\alpha+2\omega\alpha\right)\right\} \\
P(t) \,&=\frac{1}{2\alpha^2}\cos^2\theta\,\left[3k^2 \,+\, 12k\omega \,+\, 14\omega^2 \,+\, 4\omega^2\cos\left(\alpha t\right)\right] + \\
&\quad +\, \frac{1}{4\alpha^2}\sin^2\theta \\
&\quad \left\{\omega^2 e^{-it\alpha} \,+\, \omega^2 e^{it\alpha} \,+\, 2\left(\alpha^2-\omega^2\right) \,+\right. \\
&\quad +\, e^{\frac{it}{2}(-k+6\omega-\alpha)}\,\left(\alpha^2-k\alpha-2\omega\alpha\right) \,+ \\
&\quad +\, e^{\frac{it}{2}(k-6\omega+\alpha)}\,\left(\alpha^2-k\alpha-2\omega\alpha\right) \,+ \\
&\quad +\, e^{\frac{it}{2}(k-6\omega-\alpha)}\,\left(\alpha^2+k\alpha+2\omega\alpha\right) \,+ \\
&\quad \left.+\, e^{\frac{it}{2}(-k+6\omega+\alpha)}\,\left(\alpha^2+k\alpha+2\omega\alpha\right)\right\}
\end{aligned}$$

$$
\begin{aligned}
P(t) =& \frac{1}{2\alpha^2}\cos^2\theta\,\left[3k^2 + 12k\omega + 14\omega^2 + 4\omega^2\cos(\alpha t)\right] + \\
&+ \frac{1}{4\alpha^2}\sin^2\theta \\
&\left\{2\,\omega^2\,\cos(\alpha t) + 2\left(\alpha^2-\omega^2\right) + \right. \\
&\left(\alpha^2 - k\alpha - 2\omega\alpha\right)\left[e^{-\frac{it}{2}(k-6\omega+\alpha)} + e^{\frac{it}{2}(k-6\omega+\alpha)}\right] + \\
&\left.\left(\alpha^2 + k\alpha + 2\omega\alpha\right)\left[e^{\frac{it}{2}(k-6\omega-\alpha)} + e^{-\frac{it}{2}(k-6\omega-\alpha)}\right]\right\}
\end{aligned}
$$

$$
\begin{aligned}
P(t) =& \frac{1}{2\alpha^2}\,\cos^2\theta\,\left[3k^2 + 12k\omega + 14\omega^2 + 4\omega^2\cos(\alpha t)\right] + \\
&+ \frac{1}{4\alpha^2}\,\sin^2\theta\,\left\{2\omega^2\cos(\alpha t) + 2\left(\alpha^2-\omega^2\right) + \right. \\
&\left(\alpha^2 - k\alpha - 2\omega\alpha\right)\,2\cos\left(\frac{k-6\omega+\alpha}{2}\,t\right) + \\
&\left.\left(\alpha^2 + k\alpha + 2\omega\alpha\right)\,2\cos\left(\frac{k-6\omega-\alpha}{2}\,t\right)\right\}
\end{aligned}
$$

This expression describe the muon spin polarization for the case of a single crystal with the dipole axis which form an angle θ with respect to $P(0)$.

7. For polycrystalline samples the "powder average" over all possible orientations [132] must be performed

$$
\langle P(t)\rangle = \frac{1}{8\pi^2}\int_0^{2\pi} d\alpha \int_0^{2\pi} d\gamma \int_0^{\pi} d\theta\,\sin\theta\,P(t)
$$

$$
\langle P(t)\rangle = \frac{1}{8\pi^2}\,4\pi^2\left[A\int_0^{\pi}\cos^2\theta\,\sin\theta d\theta + B\int_0^{\pi}\sin^2\theta\sin\theta d\theta\right]
$$

Where A and B are respectively the content of the square brackets and braces of the above expression of polarization. The integrals to be performed are:

$$
\begin{aligned}
\longrightarrow & \int_0^{\pi}\cos^2\theta\,\sin\theta d\theta = \int_0^{\pi} -\cos^2\theta\,d(\cos\theta) = \\
&= \frac{\cos^3\theta}{3}\Big|_0^{\pi} = \frac{2}{3}
\end{aligned}
$$

$$
\begin{aligned}
\longrightarrow & \int_0^{\pi}\sin^2\theta\sin\theta d\theta = \int_0^{\pi}(1-\cos^2\theta)\sin\theta d\theta = \\
&= \int_0^{\pi}\sin\theta d\theta - \int_0^{\pi}\cos^2\theta\,\sin\theta d\theta = \\
&= (-\cos\theta)\Big|_0^{\pi} - \frac{2}{3} = 1 + 1 - \frac{2}{3} = \frac{4}{3}
\end{aligned}
$$

The powder average of polarization then results

$$\begin{aligned}\langle P(t)\rangle \;=\; \frac{1}{3}A \;+\; \frac{2}{3}B \;=\; \frac{1}{6\alpha^2}\left[3k^2 \;+\; 12k\omega \;+\; 14\omega^2 \;+\; 4\omega^2\cos\left(\alpha t\right)\right] \;+\\ +\; \frac{1}{6\alpha^2}\left[2\omega^2\cos\left(\alpha t\right) \;+\; 2\left(\alpha^2-\omega^2\right) \;+\right.\\ 2\left(\alpha^2-k\alpha-2\omega\alpha\right)\cos\left(\frac{k-6\omega+\alpha}{2}\,t\right) \;+\\ \left.\left(\alpha^2+k\alpha+2\omega\alpha\right)\,2\cos\left(\frac{k-6\omega-\alpha}{2}\,t\right)\right]\,.\end{aligned}$$

Remembering that $\alpha^2 \;=\; 6\omega^2+4\omega k+k^2$ one finally obtain

$$\begin{aligned}\langle P(t)\rangle \;=\; \frac{1}{6\alpha^2}\left[\left(5k^2 \;+\; 20\omega k \;+\; 4\omega^2\right) \;+\; 6\omega^2\cos\left(\alpha t\right)+\right.\\ +2\left(\alpha^2-k\alpha-2\omega\alpha\right)\cos\left(\frac{k-6\omega+\alpha}{2}\,t\right) \;+\\ \left.+2\left(\alpha^2+k\alpha+2\omega\alpha\right)\cos\left(\frac{k-6\omega-\alpha}{2}\,t\right)\right]\end{aligned}$$

The latter equation describes beats depending on complex functions of both the dipolar and quadrupolar frequencies and is the model that can be employed to fit ZF μSR data for the case of the muon-deuterium interaction.

Acknowledgements

I wish to thank first my research colleagues: Mauro for his guidance and to continue fostering my research attitude everyday and Daniele, for his continuative company in the labs and friendship. Thanks to Alessandra. Together with them I also thank the Fullerene Research Group alumni, Matteo, Fabio G., Angelo and Massimo.
Thanks to Roberto, for his precious (not only scientific) support.

Official thanks to Institute Laue Langevin, for provision of neutron beamtime and to the Rutherford Appleton Laboratory for muon experiments. Thanks to Stéphane, for his long time collaboration and for being a very good friend. Thanks to Sean Giblin and Iain McKenzie for their assistance during experiments in England and to Alexandre Ivanov for the experiment at ILL.

I acknowledge the financial support of the EU/FP6 *Ferrocarbon* project and of the SNSF Sinergia project *HyCarbo*.

In addition many thanks to...
... the guys who spent with me all or most of our university years: Yuri, Fabio, Chiara, Nazza, Anteo, Ricky, but also Michele Bra., Elena, Giacomo, Ventu, Elisa, Luca, Daniela and Fabio P.;
... the three who are going to take their PhD with me: Laura, Francesca and Baldo;
... the most recently "added": Stefano, Aldo and Alessio.
And to many more spending their time in the universe of physics and chemistry.

Thanks to Anna, for his past and future, I hope long-life, assistance and affection.
Thanks to my all-time friends Filippo, Alexander and Giovanni, Michela, Pesca, Gaia.
And finally to my family Mara, Roberta and Bruno.

Bibliography

[1] S. Bae et al., **Roll-to-roll production of 30-inch graphene films for transparent electrodes**, *Nature Nanotechnology*, vol. 5, no. 8, 574 (Jun. 2010), doi: 10.1038/nnano.2010.132.

[2] M. A. Rafiee et al., **Fracture and fatigue in graphene nanocomposites**, *Small (Weinheim an der Bergstrasse, Germany)*, vol. 6, no. 2, 179 (Jan. 2010), doi:10.1002/smll.200901480.

[3] J. D. Fowler et al., **Practical chemical sensors from chemically derived graphene**, *ACS nano*, vol. 3, no. 2, 301 (Feb. 2009), doi:10.1021/nn800593m.

[4] Y. Ohno et al., **Label-free biosensors based on aptamer-modified graphene field-effect transistors**, *Journal of the American Chemical Society*, vol. 132, no. 51, 18012 (Dec. 2010), doi:10.1021/ja108127r.

[5] F. Schedin et al., **Detection of individual gas molecules adsorbed on graphene**, *Nature materials*, vol. 6, no. 9, 652 (Sep. 2007), doi:10.1038/nmat1967.

[6] H. Lee et al., **Calcium-decorated graphene-based nanostructures for hydrogen storage**, *Nano letters*, vol. 10, no. 3, 793 (Mar. 2010), doi:10.1021/nl902822s.

[7] Z. Jin et al., **Nano-Engineered Spacing in Graphene Sheets for Hydrogen Storage**, *Chemistry of Materials*, , no. 26, 110105122854042 (Jan. 2011), doi: 10.1021/cm1025188.

[8] T. Chakraborty, **Graphene, Nobel Prize and All that Jazz** (2010).

[9] L. Pisani et al., **A defective graphene phase predicted to be a room temperature ferromagnetic semiconductor**, *New Journal of Physics*, vol. 10, no. 3, 033002 (Mar. 2008), doi:10.1088/1367-2630/10/3/033002.

[10] O. Yazyev and L. Helm, **Defect-induced magnetism in graphene**, *Physical Review B*, vol. 75, no. 12, 1 (Mar. 2007), doi:10.1103/PhysRevB.75.125408.

[11] A. Ghosh et al., **Uptake of H_2 and CO_2 by Graphene**, *Journal of Physical Chemistry C*, vol. 112, no. 40, 15704 (Oct. 2008), doi:10.1021/jp805802w.

[12] A. K. Geim, **Graphene: status and prospects**, *Science (New York, N.Y.)*, vol. 324, no. 5934, 1530 (Jun. 2009), doi:10.1126/science.1158877.

[13] P. Wallace, **Band Theory of Graphite**, *Physical Review*, vol. 71, no. 9, 622 (1947).

[14] K. S. Novoselov et al., **Electric field effect in atomically thin carbon films**, *Science (New York, N.Y.)*, vol. 306, no. 5696, 666 (Oct. 2004), doi:10.1126/science.1102896.

[15] A. K. Geim and K. S. Novoselov, **The rise of graphene**, *Nature materials*, vol. 6, no. 3, 183 (Mar. 2007), doi:10.1038/nmat1849.

[16] Y. Niimi et al., **Scanning tunneling microscopy and spectroscopy studies of graphite edges**, *Applied Surface Science*, vol. 241, no. 1-2, 43 (Feb. 2005), doi:10.1016/j.apsusc.2004.09.091.

[17] P. Blake et al., **Making graphene visible**, *Applied Physics Letters*, vol. 91, no. 6, 063124 (2007), doi:10.1063/1.2768624.

[18] A. Ferrari et al., **Raman Spectrum of Graphene and Graphene Layers**, *Physical Review Letters*, vol. 97, no. 18, 1 (Oct. 2006), doi:10.1103/PhysRevLett.97.187401.

[19] S. Y. Zhou et al., **First direct observation of Dirac fermions in graphite**, *Nature Physics*, vol. 2, no. 9, 595 (Aug. 2006), doi:10.1038/nphys393.

[20] J. Kim et al., **Seeing graphene-based sheets**, *Materials Today*, vol. 13, no. 3, 28 (2010).

[21] J. C. Meyer et al., **The structure of suspended graphene sheets**, *Nature*, vol. 446, no. 7131, 60 (Mar. 2007), doi:10.1038/nature05545.

[22] C. Soldano et al., **Production, properties and potential of graphene**, *Carbon*, vol. 48, no. 8, 2127 (Jul. 2010), doi:10.1016/j.carbon.2010.01.058.

[23] L. Landau, **Zur Theorie der Phasenumwandlungen**, *Physikalische Zeitschrift der Sowjetunion*, vol. 11, 26 (1937).

[24] R. E. Peierls, **Quelques propriétés typiques des corps solides**, *Annales Institut Henri Poincare*, vol. 5, no. 3, 177 (1935).

[25] N. Mermin, **Crystalline Order in Two Dimensions**, *Physical Review*, vol. 176, no. 1, 250 (Dec. 1968), doi:10.1103/PhysRev.176.250.

[26] D. Garcia-Sanchez et al., **Imaging mechanical vibrations in suspended graphene sheets**, *Nano letters*, vol. 8, no. 5, 1399 (May 2008), doi:10.1021/nl080201h.

[27] **Graphene, Scientific background on the Nobel Prize in Physics 2010** (2010).

[28] C. Lee et al., **Measurement of the elastic properties and intrinsic strength of monolayer graphene**, *Science (New York, N.Y.)*, vol. 321, no. 5887, 385 (Jul. 2008), doi:10.1126/science.1157996.

[29] H. Chen et al., **Mechanically Strong, Electrically Conductive, and Biocompatible Graphene Paper**, *Advanced Materials*, vol. 20, no. 18, 3557 (Sep. 2008), doi:10.1002/adma.200800757.

[30] D. A. Dikin et al., **Preparation and characterization of graphene oxide paper**, *Nature*, vol. 448, no. 7152, 457 (Jul. 2007), doi:10.1038/nature06016.

[31] K. S. Kim et al., **Large-scale pattern growth of graphene films for stretchable transparent electrodes**, *Nature*, vol. 457, no. 7230, 706 (Feb. 2009), doi:10.1038/nature07719.

[32] S. J. Wang et al., **Fabrication of highly conducting and transparent graphene films**, *Carbon*, vol. 48, no. 6, 1815 (May 2010), doi:10.1016/j.carbon.2010.01.027.

[33] Y. Lee et al., **Wafer-scale synthesis and transfer of graphene films**, *Nano letters*, vol. 10, no. 2, 490 (Feb. 2010), doi:10.1021/nl903272n.

[34] M. Zhang et al., **Strong, transparent, multifunctional, carbon nanotube sheets**, *Science (New York, N.Y.)*, vol. 309, no. 5738, 1215 (Aug. 2005), doi:10.1126/science.1115311.

[35] Z. Wu et al., **Transparent, conductive carbon nanotube films**, *Science*, vol. 305, no. 5688, 1273 (Aug. 2004), doi:10.1126/science.1101243.

[36] A. B. Dalton et al., **Super-tough carbon-nanotube fibres**, *Nature*, vol. 423, no. 6941, 703 (Jun. 2003), doi:10.1038/423703a.

[37] N. Pugno, **Graded cross-links for stronger nanomaterials**, *Materials Today*, vol. 13, no. 3, 40 (2010).

[38] Y. Zhang et al., **Experimental observation of the quantum Hall effect and Berry's phase in graphene**, *Nature*, vol. 438, no. 7065, 201 (Nov. 2005), doi:10.1038/nature04235.

[39] S. Stankovich et al., **Graphene-based composite materials**, *Nature*, vol. 442, no. 7100, 282 (Jul. 2006), doi:10.1038/nature04969.

[40] M. Mullaney and N. Koratkar, **Graphene outperforms Carbon Nanotubes for stronger materials**, *Inside Renssealer*, vol. 4, no. 8 (2010).

[41] A. M. Van Der Zande et al., **Large-Scale Arrays of Single-Layer Graphene Resonators**, *Nano Letters*, p. 101116125413000 (Nov. 2010), doi:10.1021/nl102713c.

[42] J. S. Bunch et al., **Electromechanical resonators from graphene sheets**, *Science (New York, N.Y.)*, vol. 315, no. 5811, 490 (Jan. 2007), doi:10.1126/science.1136836.

[43] A. Sakhaeepour et al., **Potential application of single-layered graphene sheet as strain sensor**, *Solid State Communications*, vol. 147, no. 7-8, 336 (Aug. 2008), doi:10.1016/j.ssc.2008.04.016.

[44] A. Castro Neto et al., **The electronic properties of graphene**, *Reviews of Modern Physics*, vol. 81, no. 1, 109 (Jan. 2009), doi:10.1103/RevModPhys.81.109.

[45] W. A. Diño et al., **H_2 Dissociative Adsorption at the Zigzag Edges of Graphite**, *e-Journal of Surface Science and Nanotechnology*, vol. 2, no. February, 77 (2004), doi:10.1380/ejssnt.2004.77.

[46] N. B. Arboleda et al., **Scattering and dissociative adsorption of H_2 on the armchair and zigzag edges of graphite**, *Journal of Applied Physics*, vol. 96, no. 11, 6331 (2004), doi:10.1063/1.1806549.

[47] M. Fujita et al., **Peculiar localized state at zigzag graphite edge**, *Journal of the Physical Society of Japan*, vol. 65, no. 7, 1920 (1996).

[48] Y. Kobayashi et al., **Edge state on hydrogen-terminated graphite edges investigated by scanning tunneling microscopy**, *Physical Review B*, vol. 73, no. 12, 1 (Mar. 2006), doi:10.1103/PhysRevB.73.125415.

[49] Y. Kobayashi et al., **STM/STS observation of peculiar electronic states at graphite edges**, *Physica E: Low-dimensional Systems and Nanostructures*, vol. 34, no. 1-2, 678 (Aug. 2006), doi:10.1016/j.physe.2006.03.058.

[50] P. Koskinen et al., **Self-Passivating Edge Reconstructions of Graphene**, *Physical Review Letters*, vol. 101, no. 11, 1 (Sep. 2008), doi:10.1103/PhysRevLett.101.115502.

[51] V. Gusynin and S. Sharapov, **Magnetic oscillations in planar systems with the Dirac-like spectrum of quasiparticle excitations. II. Transport properties**, *Physical Review B*, vol. 71, no. 12, 1 (Mar. 2005), doi:10.1103/PhysRevB.71.125124.

[52] S. Adam et al., **A self-consistent theory for graphene transport**, *Proceedings of the National Academy of Sciences of the United States of America*, vol. 104, no. 47, 18392 (Nov. 2007), doi:10.1073/pnas.0704772104.

[53] K. S. Novoselov et al., **Two-dimensional gas of massless Dirac fermions in graphene**, *Nature*, vol. 438, no. 7065, 197 (Nov. 2005), doi:10.1038/nature04233.

[54] J. Chen et al., **Charged-impurity scattering in graphene**, *Nature Physics*, vol. 4, no. 5, 377 (2008).

[55] J. Chen et al., **Intrinsic and extrinsic performance limits of graphene devices on SiO2**, *Nature Nanotechnology*, vol. 3, no. 4, 206 (2008).

[56] K. Bolotin et al., **Temperature-Dependent Transport in Suspended Graphene**, *Physical Review Letters*, vol. 101, no. 9, 1 (Aug. 2008), doi:10.1103/PhysRevLett.101.096802.

[57] K. Bolotin et al., **Ultrahigh electron mobility in suspended graphene**, *Solid State Communications*, vol. 146, no. 9-10, 351 (Jun. 2008), doi:10.1016/j.ssc.2008.02.024.

[58] A. Rycerz et al., **Valley filter and valley valve in graphene**, *Nature Physics*, vol. 3, no. 3, 172 (Feb. 2007), doi:10.1038/nphys547.

[59] J. Cayssol, **Crossed Andreev Reflection in a Graphene Bipolar Transistor**, *Physical Review Letters*, vol. 100, no. 14, 1 (Apr. 2008), doi:10.1103/PhysRevLett.100.147001.

[60] E. Mariani and F. von Oppen, **Temperature-dependent resistivity of suspended graphene**, *Physical Review B*, vol. 82, no. 19, 1 (Nov. 2010), doi:10.1103/PhysRevB.82.195403.

[61] B. E. Feldman et al., **Broken-symmetry states and divergent resistance in suspended bilayer graphene**, *Nature Physics*, vol. 5, no. 12, 889 (Sep. 2009), doi:10.1038/nphys1406.

[62] K. Ziegler, **Delocalization of 2D Dirac Fermions: The Role of a Broken Supersymmetry**, *Physical Review Letters*, vol. 80, no. 14, 3113 (Apr. 1998), doi:10.1103/PhysRevLett.80.3113.

[63] K.-S. Park, **Topological effects, index theorem and supersymmetry in graphene** (Sep. 2010).

[64] A. A. Balandin et al., **Superior thermal conductivity of single-layer graphene**, *Nano letters*, vol. 8, no. 3, 902 (Mar. 2008), doi:10.1021/nl0731872.

[65] S. Berber et al., **Unusually high thermal conductivity of carbon nanotubes**, *Physical Review Letters*, vol. 84, no. 20, 4613 (2000).

[66] X. Wang et al., **Room-Temperature All-Semiconducting Sub-10-nm Graphene Nanoribbon Field-Effect Transistors**, *Physical Review Letters*, vol. 100, no. 20, 100 (May 2008), doi:10.1103/PhysRevLett.100.206803.

[67] M. C. Lemme et al., **A Graphene Field-Effect Device**, *IEEE Electron Device Letters*, vol. 28, no. 4, 282 (Apr. 2007), doi:10.1109/LED.2007.891668.

[68] Y.-M. Lin et al., **Operation of graphene transistors at gigahertz frequencies**, *Nano letters*, vol. 9, no. 1, 422 (Jan. 2009), doi:10.1021/nl803316h.

[69] J. T. Robinson et al., **Reduced graphene oxide molecular sensors**, *Nano letters*, vol. 8, no. 10, 3137 (Oct. 2008), doi:10.1021/nl8013007.

[70] P. K. Ang et al., **Solution-gated epitaxial graphene as pH sensor**, *Journal of the American Chemical Society*, vol. 130, no. 44, 14392 (Nov. 2008), doi:10.1021/ja805090z.

[71] M. D. Stoller et al., **Graphene-based ultracapacitors**, *Nano letters*, vol. 8, no. 10, 3498 (Oct. 2008), doi:10.1021/nl802558y.

[72] P. Blake et al., **Graphene-based liquid crystal device**, *Nano letters*, vol. 8, no. 6, 1704 (Jun. 2008), doi:10.1021/nl080649i.

[73] R. Sordan et al., **Logic gates with a single graphene transistor**, *Applied Physics Letters*, vol. 94, no. 7, 073305 (2009), doi:10.1063/1.3079663.

[74] T. J. Echtermeyer et al., **Nonvolatile Switching in Graphene Field-Effect Devices**, *IEEE Electron Device Letters*, vol. 29, no. 8, 952 (Aug. 2008), doi:10.1109/LED.2008.2001179.

[75] X. Liang et al., **Graphene Transistors Fabricated via Transfer-Printing In Device Active-Areas on Large Wafer**, *Nano Letters*, vol. 7, no. 12, 3840 (Dec. 2007), doi:10.1021/nl072566s.

[76] M. P. Levendorf et al., **Transfer-free batch fabrication of single layer graphene transistors**, *Nano letters*, vol. 9, no. 12, 4479 (Dec. 2009), doi:10.1021/nl902790r.

[77] Y.-M. Lin et al., **100-GHz transistors from wafer-scale epitaxial graphene**, *Science (New York, N.Y.)*, vol. 327, no. 5966, 662 (Feb. 2010), doi:10.1126/science.1184289.

[78] F. Xia et al., **Graphene field-effect transistors with high on/off current ratio and large transport band gap at room temperature**, *Nano letters*, vol. 10, no. 2, 715 (Feb. 2010), doi:10.1021/nl9039636.

[79] X. Li et al., **Graphene Films with Large Domain Size by a Two-Step Chemical Vapor Deposition Process**, *Nano Letters*, p. 101019121246086 (Oct. 2010), doi:10.1021/nl101629g.

[80] X. Wang et al., **Transparent, conductive graphene electrodes for dye-sensitized solar cells**, *Nano letters*, vol. 8, no. 1, 323 (Jan. 2008), doi:10.1021/nl072838r.

[81] J. Wu et al., **Organic solar cells with solution-processed graphene transparent electrodes**, *Applied Physics Letters*, vol. 92, no. 26, 263302 (2008), doi:10.1063/1.2924771.

[82] R. R. Nair et al., **Fine structure constant defines visual transparency of graphene**, *Science (New York, N.Y.)*, vol. 320, no. 5881, 1308 (Jun. 2008), doi:10.1126/science.1156965.

[83] K. Mak et al., **Measurement of the Optical Conductivity of Graphene**, *Physical Review Letters*, vol. 101, no. 19, 2 (Nov. 2008), doi:10.1103/PhysRevLett.101.196405.

[84] T. Stauber et al., **Optical conductivity of graphene in the visible region of the spectrum**, *Physical Review B*, vol. 78, no. 8, 1 (Aug. 2008), doi:10.1103/PhysRevB.78.085432.

[85] F. Bonaccorso et al., **Graphene photonics and optoelectronics**, *Nature Photonics*, vol. 4, no. 9, 611 (Aug. 2010), doi:10.1038/nphoton.2010.186.

[86] P. Avouris, **Graphene: Electronic and Photonic Properties and Devices**, *Nano Letters*, p. 100929092847080 (Sep. 2010), doi:10.1021/nl102824h.

[87] Z. Liu et al., **Open and Closed Edges of Graphene Layers**, *Physical Review Letters*, vol. 102, no. 1, 1 (Jan. 2009), doi:10.1103/PhysRevLett.102.015501.

[88] W.-M. Huang et al., **Power-law singularity in the local density of states due to the point defect in graphene**, *Physical Review B*, vol. 80, no. 12, 1 (Sep. 2009), doi:10.1103/PhysRevB.80.121404.

[89] O. Yazyev and M. Katsnelson, **Magnetic Correlations at Graphene Edges: Basis for Novel Spintronics Devices**, *Physical Review Letters*, vol. 100, no. 4, 1 (Jan. 2008), doi:10.1103/PhysRevLett.100.047209.

[90] M. Mazzani et al., **Muons probe hydrogen interactions with defective graphene**, *(in preparation)* (2011).

[91] B.-L. Huang et al., **Density of states of graphene in the presence of strong point defects**, *Physical Review B*, vol. 82, no. 15, 1 (Oct. 2010), doi:10.1103/PhysRevB.82.155462.

[92] C. B. Nielsen et al., **Organic light-emitting diodes from symmetrical and unsymmetrical π-extended tetraoxa[8]circulenes**, *Chemistry (Weinheim an der Bergstrasse, Germany)*, vol. 16, no. 44, 13030 (Nov. 2010), doi:10.1002/chem.201002261.

[93] M. Sepioni et al., **Limits on Intrinsic Magnetism in Graphene**, *Physical Review Letters*, vol. 105, no. 20, 1 (Nov. 2010), doi:10.1103/PhysRevLett.105.207205.

[94] H. S. S. R. Matte et al., **Novel Magnetic Properties of Graphene: Presence of Both Ferromagnetic and Antiferromagnetic Features and Other Aspects**, *The Journal of Physical Chemistry C*, vol. 113, no. 23, 9982 (Jun. 2009), doi:10.1021/jp903397u.

[95] C. N. R. Rao et al., **Some Novel Attributes of Graphene**, *The Journal of Physical Chemistry Letters*, vol. 1, no. 2, 572 (Jan. 2010), doi:10.1021/jz9004174.

[96] J. Červenka et al., **Room-temperature ferromagnetism in graphite driven by two-dimensional networks of pointÂ defects**, *Nature Physics*, vol. 5, no. 11, 840 (Oct. 2009), doi:10.1038/nphys1399.

[97] Y. Wang et al., **Room-temperature ferromagnetism of graphene**, *Nano letters*, vol. 9, no. 1, 220 (Jan. 2009), doi:10.1021/nl802810g.

[98] O. Yazyev, **Magnetism in Disordered Graphene and Irradiated Graphite**, *Physical Review Letters*, vol. 101, no. 3, 1 (Jul. 2008), doi:10.1103/PhysRevLett.101.037203.

[99] L. R. Radovic and B. Bockrath, **On the chemical nature of graphene edges: origin of stability and potential for magnetism in carbon materials**, *Journal of the American Chemical Society*, vol. 127, no. 16, 5917 (Apr. 2005), doi:10.1021/ja050124h.

[100] O. V. Yazyev and L. Helm, **Magnetism induced by single-atom defects in nanographites**, *Journal of Physics: Conference Series*, vol. 61, 1294 (Apr. 2007), doi:10.1088/1742-6596/61/1/255.

[101] O. V. Yazyev, **Hyperfine interactions in graphene and related carbon nanostructures**, *Nano letters*, vol. 8, no. 4, 1011 (Apr. 2008), doi:10.1021/nl072667q.

[102] P. Mohn, ***Magnetism in the solid state: an introduction*** (2003).

[103] C. P. Slichter, ***Principles of magnetic resonance***, Springer, Heidelberg (1990).

[104] M. H. Levitt, ***Spin dynamics: basics of nuclear magnetic resonance***, John Wiley & Sons, New York (2008).

[105] D. Freude and J. Haase, ***Quadrupole effects in solid state NMR***, pp. 1–90, Springer-Verlag, New York (1993).

[106] D. Freude, ***Quadrupolar Nuclei in Solid-State Nuclear Magnetic Resonance***, pp. 12 188–12 224, John Wiley & Sons, Chichester (2000).

[107] A. Jerschow, **From nuclear structure to the quadrupolar NMR interaction and high-resolution spectroscopy**, *Progress in Nuclear Magnetic Resonance Spectroscopy*, vol. 46, 63 (2005).

[108] S. J. Blundell, **Spin-polarized muons in condensed matter physics**, *Contemporary Physics*, vol. 40, no. 3, 175 (May 1999), doi:10.1080/001075199181521.

[109] P. Réotier and A. Yaouanc, **Muon spin rotation and relaxation in magnetic materials**, *Journal of Physics: Condensed Matter*, vol. 9, 9113 (Jan. 1997), doi:10.1007/BF02066147.

[110] A. Amato et al., **Weak-magnetism phenomena in heavy-fermion superconductors: selected SR studies**, *Journal of Physics: Condensed Matter*, vol. 16, no. 40, S4403 (Oct. 2004).

[111] E. Morenzoni et al., **Nano-scale thin film investigations with slow polarized muons**, *Journal of Physics: Condensed Matter*, vol. 16, no. 40, S4583 (Oct. 2004).

[112] S. F. J. Cox, **Muonium as a model for interstitial hydrogen in the semiconducting and semimetallic elements**, *Reports on Progress in Physics*, vol. 72, no. 11, 116501 (Nov. 2009), doi:10.1088/0034-4885/72/11/116501.

[113] S. F. J. Cox, **Implanted muon studies in condensed matter science** (1987), doi:10.1088/0022-3719/20/22/005.

[114] E. Roduner, ***The positive muon as a probe in free radical chemistry***, Springer-Verlag (1988).

[115] B. Webster and S. H. Kilcoyne, **Muonium radical formation in apoferritin and ferritin**, *Physical Chemistry Chemical Physics*, vol. 1, no. 20, 4805 (1999), doi:10.1039/a905030b.

[116] R. Kiefl et al., **Molecular dynamics of $\mu^+ - C_{60}$ radical in solid C_{60}**, *Physical Review Letters*, vol. 68, no. 9, 1347 (1992).

[117] P. Kunze, **Untersuchung der Ultrastrahlung in der Wilsonkammer**, *Zeitschrift fur Physik*, vol. 83, no. 1-2, 1 (Jan. 1933), doi:10.1007/BF01331088.

[118] S. Neddermeyer and C. Anderson, **Note on the Nature of Cosmic-Ray Particles**, *Physical Review*, vol. 51, no. 10, 884 (May 1937), doi:10.1103/PhysRev.51.884.

[119] J. Street and E. Stevenson, **New Evidence for the Existence of a Particle of Mass Intermediate Between the Proton and Electron**, *Physical Review*, vol. 52, no. 9, 1003 (Nov. 1937), doi:10.1103/PhysRev.52.1003.

[120] R. Garwin et al., **Observations of the Failure of Conservation of Parity and Charge Conjugation in Meson Decays: the Magnetic Moment of the Free Muon**, *Physical Review*, vol. 105, no. 4, 1415 (Feb. 1957), doi:10.1103/PhysRev.105.1415.

[121] J. H. Brewer, **A Brief History of μSR**, *Website of the International Society for Muon Spectroscopy* http://musr.org/intro/musr/history.htm.

[122] L. Le et al., **Muon-spin-rotation and relaxation studies in (TMTSF)$_2-X$ compounds**, *Physical Review B*, vol. 48, no. 10, 7284 (1993).

[123] T. Yamazaki, **Muon spin relaxation in magnetic materials**, *Hyperfine Interactions*, vol. 6, no. 1-4, 115 (1979), doi:10.1007/BF01028779.

[124] R. Walstedt and L. Walker, **Nuclear-resonance line shapes due to magnetic impurities in metals**, *Physical Review B*, vol. 9, no. 11, 4857 (Jun. 1974), doi:10.1103/PhysRevB.9.4857.

[125] A. G. Schenck, ***Muon Spin Rotation Spectroscopy: Principles and Applications in solid state physics***, Books on Demand (1985).

[126] R. Hayano et al., **Zero-and low-field spin relaxation studied by positive muons**, *Physical Review B*, vol. 20, no. 3, 850 (Aug. 1979), doi:10.1103/PhysRevB.20.850.

[127] J. Brewer et al., **Observation of muon-fluorine "hydrogen bonding" in ionic crystals**, *Physical Review B*, vol. 33, no. 11, 7813 (Jun. 1986), doi:10.1103/PhysRevB.33.7813.

[128] R. De Renzi, ***A special case: a muon with few nuclei***, *http://www.fis.unipr.it/ derenzi/dispense/pmwiki.php?n=MuSR.FMuF* (2008).

[129] M. Riccò et al., **Fullerenium salts: a new class of C_{60}-based compounds**, *Journal of the American Chemical Society*, vol. 132, no. 6, 2064 (Feb. 2010), doi:10.1021/ja909614x.

[130] M. Mazzani et al., **The F-μ-F centre in the Fullerenium salt** $(AsF_6)_2C_{60}$, *(in preparation)* (2011).

[131] R. De Renzi, ***A special case: a muon with few nuclei***, *http://www.fis.unipr.it/˜derenzi/dispense/pmwiki.php?n=MuSR.HMu* (2008).

[132] M. Edén, **Computer simulations in solid-state NMR. III. Powder averaging**, *Concepts in Magnetic Resonance*, vol. 18A, no. 1, 24 (Apr. 2003), doi:10.1002/cmr.a.10065.

[133] J. Clarke, **SQUIDs**, *Scientific American*, vol. 271, no. 2, 46 (1994).

[134] G. Jenks et al., **SQUIDS**, *Encyclopedia of Applied Physics*, vol. 19 (1997).

[135] B. Josephson, **Coupled superconductors**, *Reviews of Modern Physics* (1964).

[136] B. Josephson, **The discovery of tunnelling supercurrents**, *Reviews of Modern Physics*, vol. 46, no. 2, 251 (1974).

[137] R. Jaklevic et al., **Quantum Interference Effects in Josephson Tunneling**, *Physical Review Letters*, vol. 12, no. 7, 159 (Feb. 1964), doi:10.1103/PhysRevLett.12.159.

[138] M. McElfresh et al., **Effects of magnetic field uniformity on the measurement of superconducting samples**, *Quantum Design MPMS Application Notes*.

[139] P. Esquinazi et al., **Induced Magnetic Ordering by Proton Irradiation in Graphite**, *Physical Review Letters*, vol. 91, no. 22 (Nov. 2003), doi:10.1103/PhysRevLett.91.227201.

[140] M. Bée, ***Quasielastic neutron scattering: principles and applications in solid state chemistry, biology and materials science***, Adam Hilger, Bristol, UK (1988).

[141] G. L. Squires, ***Introduction to the theory of thermal neutron scattering***, Courier Dover Publications (1996).

[142] H. Schober and S. Rols, ***Les excitations dans la matière condensée : vibrations et phonons***, pp. 3–136, EDP Sciences, Les Ulis, France (Jun. 2010), doi:10.1051/sfn/2010001.

[143] P. Papanek et al., **Inelastic-neutron-scattering studies of poly (p-phenylene vinylene)**, *Physical Review B*, vol. 50, no. 21, 15668 (1994).

[144] C. Berger et al., **Electronic confinement and coherence in patterned epitaxial graphene**, *Science (New York, N.Y.)*, vol. 312, no. 5777, 1191 (May 2006), doi:10.1126/science.1125925.

[145] E. Rollings et al., **Synthesis and characterization of atomically thin graphite films on a silicon carbide substrate**, *Journal of Physics and Chemistry of Solids*, vol. 67, no. 9-10, 2172 (2006).

[146] K. V. Emtsev et al., **Towards wafer-size graphene layers by atmospheric pressure graphitization of silicon carbide**, *Nature materials*, vol. 8, no. 3, 203 (Mar. 2009), doi:10.1038/nmat2382.

[147] S. Unarunotai et al., **Layer-by-layer transfer of multiple, large area sheets of graphene grown in multilayer stacks on a single SiC wafer**, *ACS nano*, vol. 4, no. 10, 5591 (Oct. 2010), doi:10.1021/nn101896a.

[148] H. Cao et al., **Large-scale graphitic thin films synthesized on Ni and transferred to insulators: Structural and electronic properties**, *Journal of Applied Physics*, vol. 107, no. 4, 044310 (2010), doi:10.1063/1.3309018.

[149] A. Reina et al., **Large area, few-layer graphene films on arbitrary substrates by chemical vapor deposition**, *Nano letters*, vol. 9, no. 1, 30 (Jan. 2009), doi:10.1021/nl801827v.

[150] A. Obraztsov et al., **Chemical vapor deposition of thin graphite films of nanometer thickness**, *Carbon*, vol. 45, no. 10, 2017 (Sep. 2007), doi:10.1016/j.carbon.2007.05.028.

[151] Y. Wu et al., **Carbon Nanowalls Grown by Microwave Plasma Enhanced Chemical Vapor Deposition**, *Advanced Materials*, vol. 14, no. 1, 64 (Jan. 2002), doi:10.1002/1521-4095(20020104)14:1⟨64::AID-ADMA64⟩3.0.CO;2-G.

[152] M. Hiramatsu et al., **Fabrication of vertically aligned carbon nanowalls using capacitively coupled plasma-enhanced chemical vapor deposition**

assisted by hydrogen radical injection, *Applied Physics Letters*, vol. 84, no. 23, 4708 (2004), doi:10.1063/1.1762702.

[153] X. Li et al., **Large-area synthesis of high-quality and uniform graphene films on copper foils**, *Science (New York, N.Y.)*, vol. 324, no. 5932, 1312 (Jun. 2009), doi:10.1126/science.1171245.

[154] A. N. Obraztsov, **Chemical vapour deposition: Making graphene on a large scale**, *Nature nanotechnology*, vol. 4, no. 4, 212 (Apr. 2009), doi:10.1038/nnano.2009.67.

[155] M. Choucair et al., **Gram-scale production of graphene based on solvothermal synthesis and sonication**, *Nature Nanotechnology*, vol. 4, no. 1, 30 (2008), doi:10.1038/NNANO.2008.365.

[156] S. Park and R. S. Ruoff, **Chemical methods for the production of graphenes**, *Nature nanotechnology*, vol. 4, no. 4, 217 (Apr. 2009), doi:10.1038/nnano.2009.58.

[157] T. Szabó et al., **Evolution of Surface Functional Groups in a Series of Progressively Oxidized Graphite Oxides**, *Chemistry of Materials*, vol. 18, no. 11, 2740 (May 2006), doi:10.1021/cm060258+.

[158] H.-K. Jeong et al., **Evidence of graphitic AB stacking order of graphite oxides**, *Journal of the American Chemical Society*, vol. 130, no. 4, 1362 (Jan. 2008), doi:10.1021/ja076473o.

[159] W. Gao et al., **New insights into the structure and reduction of graphite oxide**, *Nature Chemistry*, vol. 1, no. 5, 403 (2009), doi:10.1038/NCHEM.281.

[160] V. C. Tung et al., **Low-temperature solution processing of graphene-carbon nanotube hybrid materials for high-performance transparent conductors**, *Nano letters*, vol. 9, no. 5, 1949 (May 2009), doi:10.1021/nl9001525.

[161] J. R. Lomeda et al., **Diazonium functionalization of surfactant-wrapped chemically converted graphene sheets**, *Journal of the American Chemical Society*, vol. 130, no. 48, 16201 (Dec. 2008), doi:10.1021/ja806499w.

[162] A. a. Green and M. C. Hersam, **Emerging Methods for Producing Monodisperse Graphene Dispersions**, *Journal of Physical Chemistry Letters*, vol. 1, no. 2, 544 (Jan. 2010), doi:10.1021/jz900235f.

[163] Y. Hernandez et al., **High-yield production of graphene by liquid-phase exfoliation of graphite**, *Nature nanotechnology*, vol. 3, no. 9, 563 (Sep. 2008), doi:10.1038/nnano.2008.215.

[164] G. Li et al., **Observation of Van Hove singularities in twisted graphene layers**, *Nature Physics*, vol. 6, no. 2, 109 (Nov. 2009), doi:10.1038/nphys1463.

[165] B. Brodie, **Sur le poids atomique du graphite**, *Ann Chim Phys*, vol. 59, 466 (1860).

[166] T. Nakajima, **Formation process and structure of graphite oxide**, *Carbon*, vol. 32, no. 3, 469 (1994), doi:10.1016/0008-6223(94)90168-6.

[167] L. Staudenmaier, **Verfahren zur Darstellung der Graphitsäure**, *Berichte der deutschen chemischen Gesellschaft*, vol. 31, no. 2, 1481 (May 1898), doi:10.1002/cber.18980310237.

[168] H. C. Schniepp et al., **Functionalized single graphene sheets derived from splitting graphite oxide**, *The journal of physical chemistry. B*, vol. 110, no. 17, 8535 (May 2006), doi:10.1021/jp060936f.

[169] W. Hummers Jr and R. Offeman, **Preparation of graphitic oxide**, *Journal of the American Chemical Society*, vol. 80, no. 6, 1339 (1958), doi:10.1021/ja01539a017.

[170] N. I. Kovtyukhova et al., **Layer-by-Layer Assembly of Ultrathin Composite Films from Micron-Sized Graphite Oxide Sheets and Polycations**, *Chemistry of Materials*, vol. 11, no. 3, 771 (Mar. 1999), doi:10.1021/cm981085u.

[171] H.-K. Jeong et al., **X-ray absorption spectroscopy of graphite oxide**, *EPL (Europhysics Letters)*, vol. 82, no. 6, 67004 (Jun. 2008), doi:10.1209/0295-5075/82/67004.

[172] S. Stankovich et al., **Stable aqueous dispersions of graphitic nanoplatelets via the reduction of exfoliated graphite oxide in the presence of poly(sodium 4-styrenesulfonate)**, *Journal of Materials Chemistry*, vol. 16, no. 2, 155 (2006), doi:10.1039/b512799h.

[173] A. Lerf et al., **Structure of Graphite Oxide Revisited**, *The Journal of Physical Chemistry B*, vol. 102, no. 23, 4477 (Jun. 1998), doi:10.1021/jp9731821.

[174] S. Stankovich et al., **Synthesis of graphene-based nanosheets via chemical reduction of exfoliated graphite oxide**, *Carbon*, vol. 45, no. 7, 1558 (Jun. 2007), doi:10.1016/j.carbon.2007.02.034.

[175] W. Chen et al., **Chemical Reduction of Graphene Oxide to Graphene by Sulfur-Containing Compounds**, *Journal of Physical Chemistry C*, vol. in press (2010), doi:10.1021/jp107131v.

[176] I. K. Moon et al., **Reduced graphene oxide by chemical graphitization**, *Nature Communications*, vol. 1, no. 6, 1 (Sep. 2010), doi:10.1038/ncomms1067.

[177] J. Kim et al., **Visualizing graphene based sheets by fluorescence quenching microscopy**, *Journal of the American Chemical Society*, vol. 132, no. 1, 260 (Jan. 2010), doi:10.1021/ja906730d.

[178] N. Welham, **Effect of extended ball milling on graphite**, *Journal of Alloys and Compounds*, vol. 349, no. 1-2, 255 (Feb. 2003), doi:10.1016/S0925-8388(02)00880-0.

[179] T. Shen, **Structural disorder and phase transformation in graphite produced by ball milling**, *Nanostructured Materials*, vol. 7, no. 4, 393 (Jun. 1996), doi:10.1016/0965-9773(96)00010-4.

[180] T. Makarova et al., **Ageing effects in nanographite monitored by Raman spectroscopy**, *Physica Status Solidi (B)*, vol. 245, no. 10, 2082 (Oct. 2008), doi:10.1002/pssb.200879594.

[181] S. Cox et al., **A molecular radical model for hydrogen and muonium in graphite**, *Journal of Physics: Condensed Matter*, vol. 13, 2169 (2001).

[182] P. Ordejón, **Self-consistent order-N density-functional calculations for very large systems**, *Physical Review B*, vol. 53, no. 16, R10441 (Apr. 1996), doi:10.1103/PhysRevB.53.R10441.

[183] José M Soler et al, **The SIESTA method for ab initio order- N materials simulation**, *Journal of Physics: Condensed Matter*, vol. 14, no. 11, 2745 (2002), doi:10.1088/0953-8984/14/11/302.

[184] R. Allenspach, **Ultrathin films: magnetism on the microscopic scale**, *Journal of Magnetism and Magnetic Materials*, vol. 129, no. 2-3, 160 (Jan. 1994), doi:10.1016/0304-8853(94)90108-2.

[185] R. De Renzi and G. Allodi, ***Mulab: a Matlab Toolbox***, *http://www.fis.unipr.it/˜derenzi/dispense/pmwiki.php?n=MuSR.Mulab* (2008).

[186] D. C. Elias et al., **Control of graphene's properties by reversible hydrogenation: evidence for graphane**, *Science (New York, N.Y.)*, vol. 323, no. 5914, 610 (Jan. 2009), doi:10.1126/science.1167130.

[187] P. Papanek et al., **Neutron scattering studies of disordered carbon anode materials**, *Journal of Physics Condensed Matter*, vol. 13, 8287 (Sep. 2001), doi: 10.1088/0953-8984/13/36/305.